



DELTA Annual Report 2024

**Dortmund
20. December 2024**

Edited by C. Sternemann, M. Paulus,
D. Lützenkirchen-Hecht (2024)

Preface

Dear readers, dear colleagues,

2024 was a special year for DELTA for various reasons. First of all, it was the 30th anniversary of DELTA, which was celebrated with an anniversary event on November 12th. Accordingly, Metin Tolan took us on a journey through the history and development of research at DELTA, sharing a few anecdotes, particularly from the early days. The keynote speech was given by Thomas Feurer, Chairman of the Board of Directors of the European XFEL, putting the spotlight on current aspects and possibilities of X-ray research. The well-attended ceremony ended with a tour of the machine, a diner and numerous conversations between guests, current and former employees, as also reflected in the short contribution from Wolfram Helml in this report.

The second important point in 2024 was that the TU Dortmund decided to discontinue the operation of DELTA at the end of 2026. Until then, the University will however fully support all DELTA services, so that ongoing projects can safely be finished within the next two years.

As in the year before, an impressive number of projects have been conducted at DELTA in the past 12 months – those are compiled in this report. In total, 7 reports are dedicated to instrumentation, 18 reports on X-ray scattering and 9 to X-ray spectroscopies, respectively, which reflects that all the different instruments and endstations were intensively used within the 10 weeks of user operation and 5 weeks dedicated to accelerator physics. Still, several users mailed in their samples for X-ray experiments, and the DELTA staff and the beamline scientists did their best to get the X-ray data recorded.

All contributions in this annual report from the different scientific disciplines (engineering, physics, chemistry, biology) have a high scientific quality, and reflect the broad spectrum of scientific activities at DELTA for both, fundamental and applied research.

We take the opportunity to thank the involved technicians, engineers and scientists of the machine group for running the DELTA machine, as well as we acknowledge the financial support by the funding agencies and the local government. Furthermore, the success of DELTA would not be possible without the manifold contributions from the universities and research institutions, in particular the TU Dortmund.

Christian Sternemann, Michael Paulus & Dirk Lützenkirchen-Hecht

Contents:

<u>DELTA anniversary</u>	1
30 years celebration of DELTA W. Helml	3
<u>Instrumentation</u>	7
DELTA Control System A. Althaus, A. Erpelding, D. Schirmer	9
New Steerer Power Supplies for DELTA G. Schmidt, A. Althaus, G. Dahlmann, C. Mai, H.-P. Ruhl, D. Schirmer	11
Space-Charge-Enhanced Energy Modulation at Free-Electron Lasers S. Khan	13
Worldwide first EEHG Signal at a Storage Ring S. Khan, B. Büsing, A. Held, C. Mai, A. Radha Krishnan, W. Salah, Z. Usfoor, V. Vijayan	15
Progress of the Superconducting Wiggler Operation G. Schmidt, A. Althaus, B. Beyer, B. Büsing, G. Dahlmann, T. Dybiona, A. Erpelding, P. Hartmann, S. Khan, V. Kniss, A. Leinweber, C. Mai, M. Paulus, H.-P. Ruhl, D. Schirmer, T. Schulte-Eickhoff, C. Sternemann	19
High energy EXAFS at DELTA beamline 8 D. Lützenkirchen-Hecht	23
Time-resolved X-ray absorption spectroscopy at DELTA beamline 10 D. Lützenkirchen-Hecht, S. Paripsa, L. Voss, F. Braun, F. Eckelt	25
<u>X-ray scattering</u>	27
An X-ray diffraction study on the structure of neat linear alkylamines L. Friedrich, M. Paulus, A. Perera, M. Požar, C. Sternemann	29
Structural changes of entangled and disentangled UHMWPE powders during melting U.A. Handge, C. Krüsener, L. Neumann, G.A. Luinstra, A. Vaghar, C. Sternemann, M. Paulus	31
Influence of perfluorodecalin on the structure of proteins and lipid vesicles J. Savelkouls, M. Paulus	33
Influence of ibuprofen on the pressure stability of human serum albumin J. Savelkouls, E. Schneider, C. H. Whoo, M. Paulus	35
The concentration-dependent structure factor of dextran and Ficoll® M. Paulus, M. Dargasz, J. Savelkouls, C. H. Woo, C. Gutt	37
Probing the structural evolution of starch solutions during gelation M. Agha Raza, M. Dargasz, J. Savelkouls, M. Paulus, C. Gutt	39
Protein adsorption on solid supported lipid membranes J. Savelkouls, M. Dargasz, E. Schneider, G. Scholz, C. Sternemann, M. Paulus	41

An X-ray diffraction study on the structure and phase behaviour of water-amine mixtures	43
L. Friedrich, M. Paulus, A. Perera, M. Požar, D. Lützenkirchen-Hecht, N.Thiering, J. Savelkouls, C. Sternemann	
Liquid-solid phase transformations in macromolecular liquids under cryogenic temperatures	45
M. Dargasz, J. Savelkouls, N. Das Anthuparambil, M. Paulus, C. Gutt	
Phase transition in $\text{Eu}_2\text{LiC}_3\text{H}$	47
T. Kleinöder, U. Ruschewitz	
X-ray diffraction analysis via synchrotron radiation of various natural rocks coated with TiN	49
W. Tillmann, D. Graf, N.F.L. Dias, B. Breidenstein, B. Denkena, B. Bergmann, H. Petersen	
Investigating the long-range structural evolution of multivariate ZIF-76 derivatives during exothermic melting and glass formation properties	53
G. Li, S. Henke	
Alloy Development of Austenitic Stainless Steels for Additive Manufacturing	57
M. Hussein, A. Röttger, C. Sternemann	
X-ray diffraction analysis of chemically complex TiSiBCN nanocomposites	59
W. Tillmann, J. Urbanczyk, A.Z. Ebady, N.F.L. Dias, A. Tewes, G. Bräuer	
Development and structure analysis of thermally sprayed Quasi-crystalline (QC) Al-Cu-Fe coatings	65
I. Baumann, M. A. Kada, J. Zajackowski, W. Tillmann, C. Sternemann, M. Paulus, M. Sipura, N. Piljic	
Microstructure evolution of boron-containing tool steel under rapid solidification conditions	73
H. Sohaib, A. Röttger, C. Sternemann	
Crystallographic analysis of arc-evaporated TiAlN thin films produced from differently manufactured cathode materials	75
F. Rümenapf, N.F.L. Dias, D. Stangier, N. Denkmann, A. Meijer, S. Jaquet, R.G. Carballo, J. Debus, D. Biermann, W. Tillmann	
An X-ray diffraction study of copper powder for laser-based powder bed fusion	79
E. Schneider, R. Ortman, J. Savelkouls, L. Friedrich, J. Frank, F. Hellwig, M. Blüm, M. Paulus, A. Röttger, J.T. Sehart, C. Sternemann	
<u>Hard X-ray spectroscopy</u>	81
An X-ray absorption near edge spectroscopy study on AlCrVY(O)N thin films	83
E. Schneider, F. Rümenapf, J. Savelkouls, C. Sternemann, M. Paulus, N.F.L. Dias, D. Lützenkirchen-Hecht, W. Tillmann	
Hydrogen Economy vs. Hydrogen Embrittlement: Indirect Electrochemical Determination of Hydrogen Diffusion in Steel	85
A. Drichel, M. Spiewak, A. Röttger, D. Lützenkirchen-Hecht, B.V. Manzolli Rodrigues, A. Slabon	

Revealing the metal coordination environment of solvent-free synthesised MOF glasses by X-ray absorption fine structure analysis W.-L. Xue, S. Henke	87
The structure of medium-entropy alloy nanoparticles as determined by EXAFS T. Trompeter, D. Lützenkirchen-Hecht	91
XAS Investigations of a Dual Atom Iron Catalyst on Coffee Waste Biochar for Electrochemical Kraft Lignin Depolymerization L. M. Lindenbeck, D. Lützenkirchen-Hecht, A. Drichel, B. B. Beele, B. V. M. Rodrigues, A. Slabon	93
Laser-polishing of niobium in N ₂ -atmospheres: An EXAFS study F. Brockner, D. Lützenkirchen-Hecht	95
XAS Investigations of Copper Nanoparticles on Biomass for Biomass Valorization F. Stallmann, L. M. Lindenbeck, D. Lützenkirchen-Hecht, A. Drichel, B. B. Beele, B. V. M. Rodrigues, A. Slabon	97
EXAFS investigations of Fe-Co single atoms catalysts on N-doped carbon supports K. Yuan, Y. Pei, Y. Wu, Y. Chen, B. Wu, D. Lützenkirchen-Hecht	99
Feasibility study for in-situ investigations of Vanadium in battery materials by XANES M. Spiewak, A. Drichel, V. Barra, N. Petersen, A. Slabon, D. Lützenkirchen-Hecht	101
<u>Notes</u>	103

DELTA – anniversary

30 years celebration of DELTA

W. Helml

Direktor am Zentrum für Synchrotronstrahlung (DELTA), Technische Universität Dortmund



Within the fall of 2024 the accelerator facility DELTA turned its 30th year of operation — a very good reason to celebrate the many achievements and exciting activities over the past three decades at the “*Dortmunder Elektronenspeicherringanlage*”.

To honor the fruitful history of this Westfalian Village in the harsh landscape of multinational accelerator facilities all over the world, two highly acclaimed speakers could be won to give celebratory talks: Professor Dr. Metin Tolan, at that time President of the Georg-August-Universität Göttingen, and Professor Dr. Thomas Feuerer, Managing Director and Chairman of the Management Board of the European X-ray XFEL at Schenefeld/Hamburg.

The colloquium took place in the traditional lecture hall II of the physics faculty at the TU Dortmund in front of a large and expectant audience. Many former scientists, X-ray users, fellow workers and students from DELTA had come to join the current DELTA team and academic staff from the university. In his humorous and personal presentation Prof. Tolan led the audience from the first ideas and concepts of building an accelerator in Dortmund to numerous developments and pioneering successes like the lasing of a ring-based FEL or the setup of experimental stations for X-ray diffraction under exotic high-pressure and high-temperature conditions. Even very recently new additions had been made to the ring, in form of the Superconducting Wiggler at 7 Tesla, and groundbreaking achievements had been delivered, like the first demonstration of deep UV radiation by echo-enabled harmonic generation at a storage ring.

Prof. Feurer continued the narrative with a vision about X-ray research at state-of-the-art free-electron lasers, exemplified by the Eu-XFEL, currently the world's most powerful free-electron laser source. The research outline spanned many different topics, from attosecond X-ray spectroscopy for the investigation of ultrafast processes at the core of electronic rearrangement dynamics to the impact of machine learning on understanding experimental results and dealing with huge amounts of data at measurement rates of more than 2 MHz.

The location was then transferred to the DELTA building, where guided tours of the inner workings of an accelerator facility were offered and embraced by interested laymen and experienced professionals alike. Finally, the celebrations culminated in a festive buffet in the DELTA hall, giving everybody the chance to exchange old stories and new scientific ideas in a relaxed atmosphere. Many celebrants deeply submersed in these comfortable if unusual dinner party surroundings and kept their discussions going until long into the evening — a fitting finale for the anniversary of an accelerator run devotedly over 30 years in many shifts during day and night!



PS: I want to express my specific thanks to all of the DELTA team who helped organize this event and to the Faculty of Physics for the support.

The pictures in the following give some more impressions of the anniversary celebrations:



High demand for the DELTA guided tours and much to explain for the tour guides.



Prof. Wille is opening the buffet with enjoyable insights about the founding phase of DELTA.



The buffet in the outskirts of the accelerator hall gave an inspiring background for many extensive conversations.



Prof. Feurer and the author enjoy a beer after the anniversary colloquium.

Instrumentation

DELTA Control System

A. Althaus, A. Erpelding, D. Schirmer

Zentrum für Synchrotronstrahlung (DELTA), Technische Universität Dortmund

Introduction:

Usual maintenance work was carried out on the DELTA EPICS-based control system. This includes hardware replacements, software updates, network infrastructure improvements and the EPICS integration of new device controls. One extensive renewal was the replacement of a large part of the outdated server infrastructure and the implementation of NixOS [1] environment, a Linux distribution based on the Nix package manager.

- The majority of deprecated servers (out of warranty and maintenance) have been replaced by two new 19-inch rack servers (based on: CPU EPYC 7443P 24C/48T). They were purchased in summer 2024 within the estimated investment funds and have been installed very soon after delivery in autumn 2024. The new hardware replaces also the outdated storage area network (SAN) system. For this purpose, the servers were configured as a redundant Proxmox cluster [2]. The Proxmox virtual environment operates as an open source server management platform for enterprise virtualization. It tightly integrates kernel-based virtual machine hypervisors (KVM) and Linux containers (LXC), software-defined storage and networking functionality, on a single platform. The integrated web-based user interface also simplifies the management of high availability within the server cluster and the integrated disaster recovery tool. At DELTA, the cluster operates as a KVM hypervisor for all implemented VMs. The VMs in turn provide general-purpose and a variety of DELTA-specific software services (see Fig. 1, right). These include, for example, the basic network services, machine services (e.g., EpicsLog, boot server, Epics-SoftIOCs, etc.), management services (e.g., database web services, monitoring, etc.) and general services (e.g., Git, DELTA-Wiki, elog shift book, etc.). An additional computer freed up by the server exchange also functions as a Proxmox backup server and acts at the same time as the third node in the Proxmox cluster to ensure high availability and reliability. This means that the failure of one of the above-mentioned services is automatically taken over by the other server within the cluster. The new installation partially replaces 13-year-old hardware and thus significantly increases computing performance (e.g., for database access and EpicsLog queries) and reliability. The new system has been running for several months with high stability, minimum maintenance effort and no downtime.

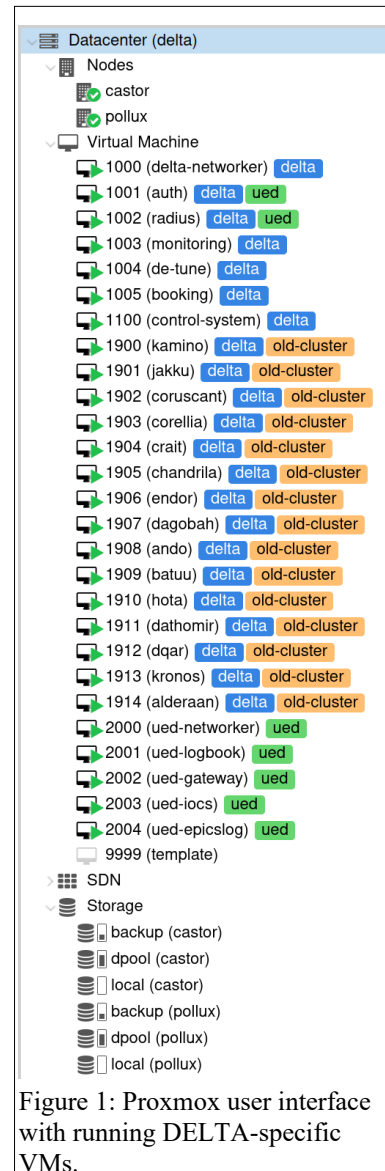


Figure 1: Proxmox user interface with running DELTA-specific VMs.

- To ease with maintenance and provide a more reliable software environment, a new operating system NixOS was evaluated. Our typical distribution is generally based on ad-hoc management of the operating system configuration. After installation of the software from the provided package manager, multiple files have to be edited to realize the needed features. Modern cloud computing provides tools like Ansible [3] to automate this process and allow version control of the configuration. But this can still lead to errors because of the order of operations or other side effects of changing the configuration. NixOS takes a different approach. The complete system configuration is defined in a domain-specific language called Nix (see Fig. 2, right).

```
{ config, lib, ... }:
{
  imports = [
    ../profiles/proxmox-vm.nix
    ../applications/room-booking
  ];

  nixpkgs.hostPlatform = lib.systems.examples.gnu64;

  delta = {
    vmid = 1005;
    project = "delta";
  };

  networking = {
    useDHCP = false;

    interfaces.main = {
      name = "enp6s18";

      ipv4.addresses = [ {
        address = "129.217.175.66";
        prefixLength = 27;
      } ];
    };

    defaultGateway = {
      address = "129.217.175.65";
      interface = config.networking.interfaces.main.name;
    };

    nameservers = [ "129.217.164.200" ];
  };

  # This value determines the NixOS release from which the default
  # settings for stateful data, like file locations and database versions
  # on your system were taken. It's perfectly fine and recommended to leave
  # this value at the release version of the first install of this system.
  # Before changing this value read the documentation for this option
  # (e.g. man configuration.nix or on https://nixos.org/nixos/options.html).
  system.stateVersion = "24.05";
}
```

Figure 2: Example of NixOS system configuration.

This provides build recipes for all software packages and all configuration files. The configuration can then be put under version control, providing a complete, reproducible system configuration. NixOS uses the Nix package repository [4] (nixpkgs) which provides more than 100,000 packages. The repository supplies pre-build binaries, so only the configuration files for the system need to be build. The Nix community provides many abstractions that make it easy to extend NixOS with own software and system configuration. At DELTA we developed a module for EPICS packages, which gives us an easy way to build EPICS base 3 and 7, asyn, streamdevice, gateway server and more packages [5]. We also developed modules for some of our own Python-based software (e.g., channel_access library, epicslog). A small number of virtual machines are already running NixOS, and the others will be ported from the Debian-based OS in the future. Because the Nix package manager can be used in addition to a distribution's package manager, it can also provide a consistent and tested repository of facility packages that can be used by users and researchers on other Linux-based distributions.

References

- [1] <https://nixos.org>
- [2] <https://www.proxmox.com/en>
- [3] <https://www.redhat.com/en/ansible-collaborative>
- [4] <https://github.com/NixOS/nixpkgs>
- [5] <https://epics-controls.org/>

New Steerer Power Supplies for DELTA

G. Schmidt, A. Althaus, G. Dahmann, C. Mai, H.-P. Ruhl, D. Schirmer

Zentrum für Synchrotronstrahlung (DELTA), Technische Universität Dortmund



Figure 1: A comparison of the DELTA (left) and DESY (right) power supply unit.

The DELTA steerer power supplies were an adaptation of a previous DESY power supply design (see figure 1) that allowed higher currents (10 A) with reduced voltage (20 V) instead of 3.5 A, 120 V of the original DESY device. The power supplies are current regulated, using 12-bit DACs. The backplane connections and software communications are completely identical between the two developments. With the higher output current thermal problems occurred on some components of the power supplies at DELTA, therefore additional cooling was installed years ago to reduce the failure rate of the power supplies, but the problem was not solved satisfactorily. The alignment initiative of the dipole and quadrupole magnets [1] significantly reduced the average and peak currents of the steerer power supplies, necessary to achieve the design orbit. Now nearly all steerer power supplies are at values which can be delivered with the original DESY power supply. 64 steerer power supplies have been obtained in

2023 from DESY out of the heritage of HERA. Tests have been made during this year and it has been shown that the DESY power supplies can be easily adapted to the DELTA control system. The regulation step width of the output current is smaller and the regulation accuracy of the DESY power supplies is better, because the same digital resolution is used for a smaller maximum current. In the near future we will exchange a significant number of steerer power supplies to the DESY type. After modifying the device current limits in the orbit correction program, it was shown that operation with mixed DELTA and DESY steerer power supplies is possible without any problems. In addition to the higher regulation accuracy we expect to profit from the many spare components we obtained with the delivery from DESY.

We want to thank particularly the DESY MKK group for their support and the transfer of the steerer power supplies.

References:

[1] Progress on survey and alignment of the DELTA magnets and vacuum chambers, G. Schmidt et al., DELTA annual report 2020

Space-Charge-Enhanced Energy Modulation at Free-Electron Lasers

S. Khan

Zentrum für Synchrotronstrahlung (DELTA), Technische Universität Dortmund

As an external activity, an experimental investigation [1-3] of the effect of longitudinal space charge (LSC) at FERMI, a free-electron laser (FEL) user facility at Elettra Sincrotrone Trieste in Italy [4], was conducted. In this context, a new method to enhance an initially small laser-induced energy modulation was proposed and investigated experimentally.

Seeding of FELs with laser pulses improves the longitudinal coherence of the FEL output and reduces pulse-to-pulse fluctuations of pulse energy, arrival time, and central wavelength compared to self-amplified spontaneous emission (SASE) [5]. In the high-gain harmonic generation (HG) scheme [6], the interaction with a laser pulse in a first undulator (“modulator”) creates a sinusoidal modulation of the electron energy, which is converted to periodic microbunches in a dispersive section (“chicane”) – see Fig. 1 (a). Lasing takes place in a second long undulator (“radiator”) tuned to a harmonic of the initial seed laser wavelength.

If the chicane is followed by a drift section, LSC causes a debunching effect, i.e., it broadens the microbunches, thus reducing their bunching factor. On the other hand, LSC also flattens the correlated energy spread of the electrons between the microbunches (Fig. 1 (b)), which may be advantageous for harmonic generation [7]. If the drift section is long enough, the correlated energy spread rises again with opposite sign (Fig. 1 (c)), which can be used to create new microbunches in a second chicane (Fig. 1 (d)). Simulation studies suggest that the bunching factor of the new microbunches may be larger than that of the original ones. After a drift length d , the amplitude of energy modulation $A(d)$ normalized to the energy spread is given in a simplified model by

$$A(d) = |s| \cdot d - A(0),$$

where s is the approximately constant LSC-induced normalized energy change per drift length. The counterintuitive result is that the final modulation amplitude after a given drift length is larger when the initial modulation amplitude $A(0)$ is smaller. This is because the zero-crossing of the correlated energy spread, as shown in Fig. 1 (b), happens at shorter distance, leaving more of the remaining drift length for the modulation with opposite sign to develop.

Thus, the scheme presented here is attractive when the initial energy modulation amplitude is small, e.g., in seeded FELs with high repetition rate, or to recover from the debunching effect in a drift section.

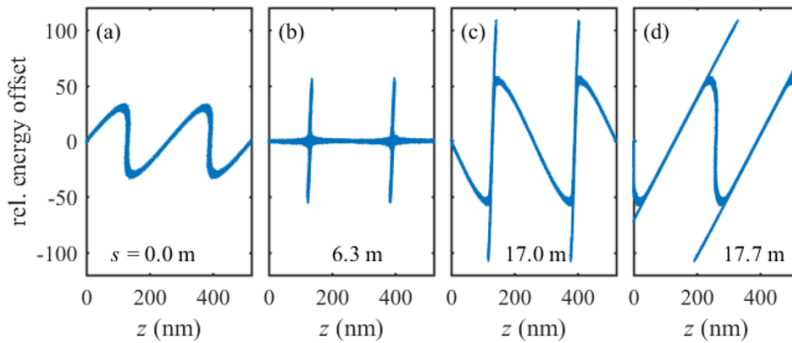


Figure 1: Phase-space distribution of electrons (energy offset versus longitudinal position) after laser-induced energy modulation and a dispersive section (a), after additional drift under the influence of longitudinal space charge (b,c), and after a second dispersive section (d).

An experimental investigation of this yet unexplored regime has been conducted at the FEL-1 beamline of FERMI, where the first chicane was tuned for optimum HGHG signal, and the longitudinal dispersion $R_{56}(2)$ of the second chicane after a drift section was scanned. The measurements were repeated under variation of the seed pulse energy, the peak current of the electron bunch, and the number of undulators acting as FEL radiator.

Figure 2 shows an example. As expected, the signal is strongly reduced with nonzero $R_{56}(2)$ and rises again with the condition shown in Fig. 1 (d), followed by a tail consisting of many merging secondary peaks. The pulse energy around $R_{56}(2) = 50 \mu\text{m}$ is significantly higher than the HGHG signal with zero $R_{56}(2)$. A dip near $R_{56}(2) = 30 \mu\text{m}$ hints that the underlying physics is more complex than described above, requiring a more detailed analysis of the data and maybe further measurements.

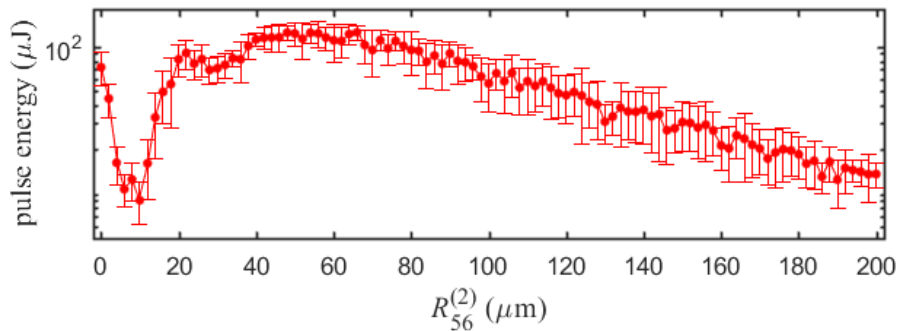


Figure 2: Example of scanning the longitudinal dispersion $R_{56}(2)$ of the second chicane while recording the FEL pulse energy after 6 undulators, i.e., the maximum available radiator length. Here, the seed pulse energy was $11.8 \mu\text{J}$ and the peak current was about 1700 A .

Acknowledgements

The kind hospitality of the FERMI team is gratefully acknowledged, particularly the guidance provided by P. R. Ribič during the measurements.

References

- [1] S. Khan et al., *Evolution of microbunching in drift sections*, Proc. of FEL'22, Trieste, Italy, p. 21 (2022).
- [2] S. Khan et al., *Space charge effects on density-modulated electron beams in drift spaces*, Proc. of IPAC'23, Venice, Italy, p. 1835 (2023).
- [3] S. Khan et al., *Evolution of density-modulated electron beams in drift sections*, Phys. Rev. Accel. Beams 27, 040702 (2024).
- [4] E. Allaria et al., *The FERMI free-electron lasers*, J. Synchrotron Radiation 22, p. 485 (2015).
- [5] A. M. Kondratenko, E. L. Saldin, *Generating coherent radiation by a relativistic electron beam in an undulator*, Particle Accelerators 10, p. 207 (1980).
- [6] L. H. Yu, *Generation of intense uv radiation by subharmonically seeded single-pass free-electron lasers*, Phys. Rev. A 44, p. 5178 (1991).
- [7] E. Hemsing et al., *Correlated Energy-Spread Removal with Space Charge for High-Harmonic Generation*, Phys. Rev. Lett. 113, 134802 (2014).

Worldwide first EEHG Signal at a Storage Ring

S. Khan, B. Büsing, A. Held, C. Mai, A. Radha Krishnan,
W. Salah*, Z. Usfoor, V. Vijayan

Zentrum für Synchrotronstrahlung (DELTA), Technische Universität Dortmund

* The Hashemite University, Zarqa, Jordan

Until recently, the short-pulse source operated at DELTA [1,2] was based on coherent harmonic generation (CHG) [3], where the interaction between ultrashort laser pulses and electrons in an undulator (“modulator”) results in a sinusoidal modulation of the electron energy. A dispersive section (“chicane”) leads to a density modulation (“microbunching”) and coherent emission of ultrashort radiation pulses in a second undulator (“radiator”) tuned to a harmonic of the laser wavelength.

Echo-enabled harmonic generation (EEHG) [4] was proposed in 2009 as a seeding scheme for free-electron lasers and was demonstrated at several linac-based facilities [5-8]. However, it can also be adopted for storage rings to generate ultrashort radiation pulses as proposed in [9-14]. The scheme is based on a twofold laser-electron interaction leading to a more complex density pattern and higher laser harmonics compared to CHG – see Fig. 1.

In summer 2022, the electromagnetic undulator U250 at DELTA was rewired for the SPEED project (Short-Pulse Emission via EEHG at DELTA) to undertake the worldwide first demonstration of EEHG at a storage ring. A single insertion device with a length of only 4.75 m and 38 periods now comprises two modulator sections, two chicanes and a radiator section. The calculated magnetic field, transverse beam excursion, and the integrated matrix element R_{56} measuring the strength of magnetic chicanes are shown in the left part of Fig. 2 [15].

As sketched in Fig. 2 (right), pulses from a Ti:sapphire laser system are frequency-doubled by SHG (second-harmonic generation) resulting in residual 800-nm pulses for the first energy modulation and 400-nm pulses for the second one. The interaction of both pulses with the electrons was demonstrated in September 2022 with coherent emission at a wavelength of 267 nm [16]. This was a first indication of the EEHG process, since the emission wavelength is not a harmonic of the 400-nm pulses and both pulses were required to produce the signal.

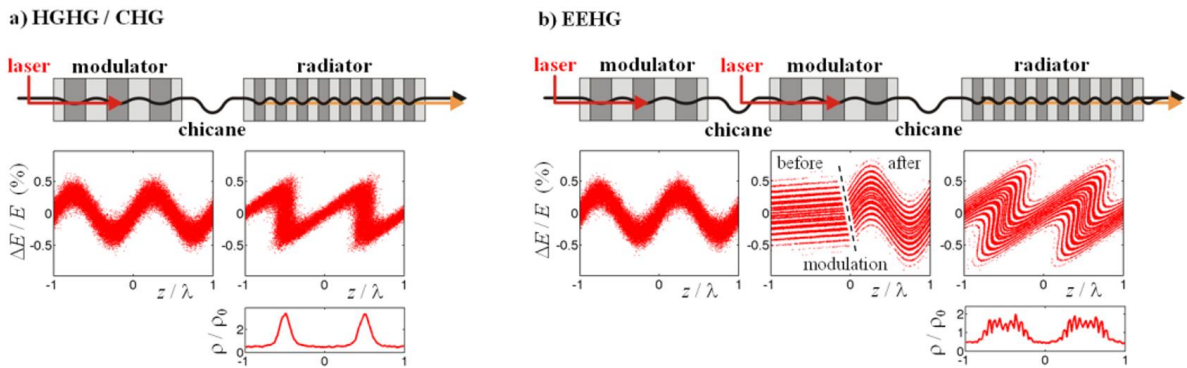


Figure 1: Magnetic configuration for CHG (left) and EEHG (right) with respective phase space distributions (i.e., relative energy offset $\Delta E/E$ versus longitudinal coordinate z in units of the laser wavelength λ) and longitudinal distribution of the final normalized electron density ρ/ρ_0 .

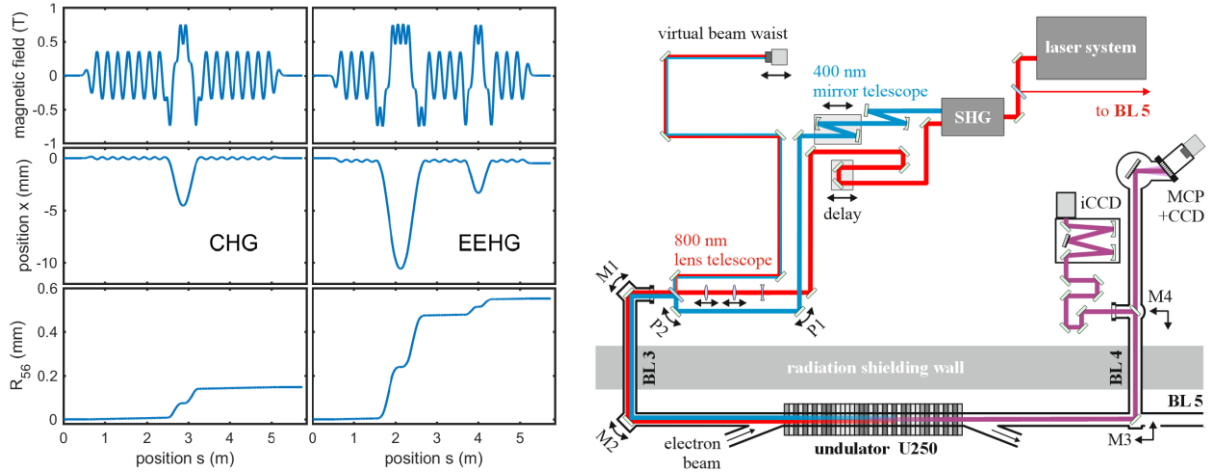


Figure 2: Left: Calculated magnetic field (top), horizontal electron path (center), and integrated R_{56} matrix element (bottom) as function of position along the undulator U250 for CHG and EEHG. Right: Paths of laser pulses (red and blue) and the resulting EEHG pulses (magenta), which are detected by an in-vacuum grating spectrometer equipped with a microchannel plate (MCP) and a CCD camera [17].

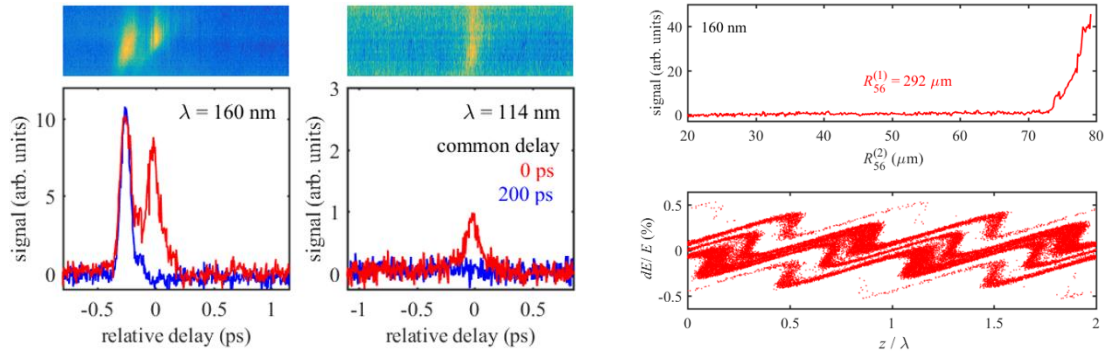


Figure 3: Left: Scans of the delay between 400- and 800-nm pulses with (red) and without (blue) interaction with the electrons while recording signals at 160 nm and 114 nm (above: raw data from the spectrometer). Right: Signal at 160 nm as function of the R_{56} value of the second chicane. For maximum R_{56} , the calculated phase space distribution is shown below.

After the first results in 2022, the project was plagued by technical issues involving significant investment and delay. It took until June 2024 to demonstrate first EEHG signals at shorter wavelengths, 160 nm and 114 nm [18]. In Fig. 3 (left), the respective signals are shown under variation of the delay between the two laser pulses. One of the two lines at 160 nm persists even after applying a common delay of 200 ps, i.e., without laser-electron interaction. This line is interpreted as harmonic generation in upstream dielectric mirrors [19]. The signal at 144 nm is only present when both laser pulses overlap with the same electrons. The right part of Fig. 3 shows an R_{56} scan of the second chicane, where the maximum of the 160-nm signal is barely reached, but increasing the chicane strength further tends to distort the electron orbit.

The present layout with only 4 periods per undulator, moderate R_{56} values, and limited laser power is not ideally suited for EEHG. An equally short setup with permanent magnets would enable more undulator periods improving the energy modulation and radiation output. Nevertheless, the setup at DELTA allows to study the consistency of measurements and theory in view of future EEHG applications at storage rings. The relative energy modulation and the R_{56} range can be improved by reducing the electron energy at the expense of beam lifetime [20].

References

- [1] S. Khan et al., *Coherent harmonic generation at DELTA: A new facility for ultrashort pulses in the VUV and THz regime*, Sync. Rad. News 24:5, p. 18 (2011).
- [2] S. Khan et al., *Generation of Ultrashort and Coherent Synchrotron Radiation Pulses at DELTA*, Sync. Rad. News 26:3, p. 25 (2013).
- [3] R. Coisson and F. De Martini, *Free-electron coherent relativistic scatterer for UV-generation*, Quantum Electronics 9, p. 939 (1982).
- [4] G. Stupakov, *Using the Beam-Echo Effect for Generation of Short-Wavelength Radiation*, Phys. Rev. Lett. 102, 074801 (2009).
- [5] D. Xiang et al., *Demonstration of Echo-Enabled Harmonic Generation Technique for Short-Wavelength Seeded Free-Electron Laser*, Phys. Rev. Lett. 105, 114801 (2010).
- [6] Z.T. Zhao et al., *First lasing of an echo-enabled harmonic generation free-electron laser*, Nat. Photonics 6, p. 360 (2012).
- [7] E. Hemsing et al., *Echo-enabled harmonics up to the 75th order from precisely tailored electron beams*, Nat. Photonics 10, p. 515 (2016).
- [8] P. Rebernik Ribič et al., *Coherent soft X-ray pulses from an echo-enabled harmonic generation free-electron laser*, Nat. Photonics 13, p. 555 (2019).
- [9] R. Molo et al., *Echo-enabled harmonic generation at DELTA*, Proc. of IPAC'11, San Sebastián, Spain, p. 3074 (2011).
- [10] C. Evain et al., *Soft x-ray femtosecond coherent undulator radiation in a storage ring*, New J. Phys. 14, 023003 (2012).
- [11] H. Li et al., *Echo-Enabled Harmonic Generation Based on Hefei Storage Ring*, Proc. of IPAC'13, Shanghai, China, p. 1208 (2013).
- [12] A. Streun et al., *SLS-2 – the upgrade of the Swiss Light Source*, J. Sync. Radiation 25, p. 631 (2018).
- [13] J.-G. Hwang et al., *Generation of intense and coherent subfemtosecond X-ray pulses in electron storage rings*, Sci. Reports 10, p. 10093 (2020).
- [14] X. Yang et al., *Optimization of echo-enabled harmonic generation toward coherent EUV and soft X-ray free-electron laser at NSLS-II*, Sci. Reports 12, p. 9437 (2022).
- [15] B. Büsing et al., *Preparatory experimental investigations in view of EEHG at the DELTA storage ring, Reconfiguration of the U250 for EEHG*, Proc. of FEL'22, Trieste, Italy, p. 313 (2022).
- [16] S. Khan et al., *SPEED: Worldwide first EEHG implementation at a storage ring*, Proc. of IPAC'23, Venice, Italy, p. 1057 (2023).
- [17] Z. Usfoor et al., *A New Spectrometer for the Characterization of VUV/XUV Radiation at DELTA*, DELTA Annual Report 2022.
- [18] S. Khan et al., *Commissioning of echo-enabled harmonic generation at the Delta storage ring*, Proc. of FEL'24, MOAI02/TUP250 (2024).
- [19] T. Tsang, *Reflected optical harmonic from dielectric mirrors*, App. Optics 33, p. 7720 (1994).
- [20] C. Mai et al., *Observation of coherent terahertz bursts during low-energy operation of DELTA*, Proc. of IPAC'23, Venice, Italy, p. 1061 (2023).

Progress of the Superconducting Wiggler Operation

G. Schmidt, A. Althaus, B. Beyer, B. Büsing, G. Dahlmann, T. Dybiona, A. Erpelding, P. Hartmann, S. Khan, V. Kniss, A. Leinweber, C. Mai, M. Paulus, H.-P. Ruhl, D. Schirmer, T. Schulte-Eickhoff, C. Sternemann
Zentrum für Synchrotronstrahlung (DELTA), Technische Universität Dortmund

In summer shutdown 2020, the old 5.5-T superconducting asymmetric wiggler (SAW) with 5 periods was replaced by a new superconducting wiggler (SCW) with ten full 7-T symmetric periods [1]. It was shown that the old wiggler outlet chamber was not able to withstand the high-power radiation fan of the new SCW which delivers four times the radiation power of the old SAW. In recent years, the maximum field of the new wiggler has therefore been limited to 5 T during beam time.



Figure 1: New wiggler outlet chamber and photon absorber area.



Figure 2: Water flow, pressure and temperature control of all absorber cooling circuits.

displayed in the control system (see Fig. 2). An interlock is triggered if the water temperature reaches a critical value or the water flow gets too low.

To enable the SCW to operate at maximum field, some improvements to the wiggler outlet chamber and radiation shielding were required. The new design of the chamber was developed in cooperation with the engineering office at the department of physics of TU Dortmund, the company FMB in Berlin, and the DELTA group. The new chamber was delivered in its final version in summer 2024, approved, and directly installed in the summer shutdown (July to September 2024) at the storage ring (see Fig. 1).

The shutdown was also used for the exchange of wearing parts of the SCW which have been operated now for more than 3 years.

The chamber was placed with high metrological accuracy to its final mechanical position in the storage ring coordinate system by use of reference marks and planes as well as a high-precision water level and a laser tracker. Exchangeable copper absorbers take the main load of the radiation power. The water flow and temperature of all absorber cooling channels are monitored and

During tests at small beam currents with the old wiggler chamber and fields of the new device above 5 T, it was observed that the radiation background outside the shielding wall increased with the field of the wiggler. To allow for operation above 6 T, additional shielding was



Figure 3: Radiation shielding hutch enclosing the new outlet chamber and the three hard x-ray beamlines.

necessary. A lead housing around all components which could be hit by the wiggler radiation was therefore installed (see Fig. 3) and integrated in the personal interlock system of DELTA.

After the new chamber was installed, the beam lifetime recovered very fast. After only two weeks of operation, beam lifetimes comparable to those before the installation were achieved as shown in Fig. 4. To enable this short recovery of the beam lifetime, a bake-out of the chamber at a temperature of 270 °C had been performed for more than four weeks between the installation of the outlet chamber at the storage ring and the first electron beam operation. The SCW with the new outlet chamber was then operated with up to 6 T. As expected from the design, only one absorber shows an increase in cooling water temperature of about 5 °C. The alignment of the chamber is well within the specification so that the radiation is nearly perfectly transmitted through the chamber.

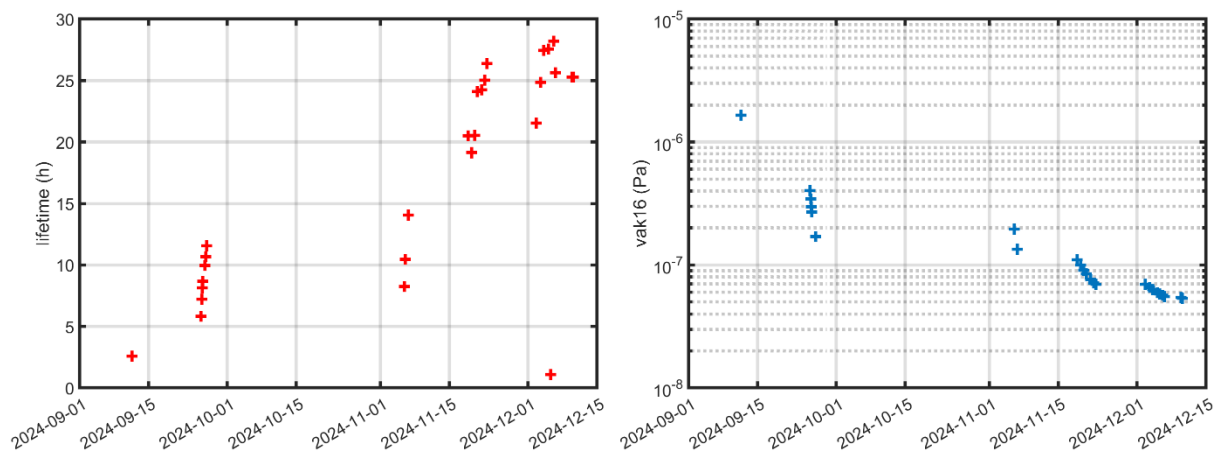


Figure 4: Left: Development of the electron beam lifetime at 100 mA stored beam current. Right: Pressure over time in the new outlet chamber at 100 mA stored beam current..

The radio frequency power was adapted to the higher beam power consumption allowing now an operation with one or two cavities and a beam current of 140 mA with a magnetic field of 5.5 T.

The first weeks of user operation with a field of 5.5 T lead to an increase of the flux at beamline 9 of around 30 % at a photon energy of 27 keV. Beamline 10 profits from an increase of 75 % at 14 keV. Beamline 8 is now able to operate at photon energies up to 27 keV (at 5 T, the maximum energy was 22 keV) and profits from a higher intensity and the improved signal-to-noise ratio of the measurements. To further increase the magnetic field in

user operation, additional work is needed to improve the beamline and monochromator cooling.

References

- [1] G. Schmidt et al., *Installation and Conditioning of the 7-T Superconducting Wiggler*, DELTA Annual Report 2020, p. 15.

High energy EXAFS at DELTA beamline 8

D. Lützenkirchen-Hecht

Faculty of Mathematics and Natural Sciences-Physics Department, University of Wuppertal,
Gauss-Str. 20, D-42119 Wuppertal, Germany

EXAFS is a well-established method to obtain the atomic short range order and the chemical valence of a selected element within solid, liquid or even gaseous materials [1]. So far, the energy range for EXAFS investigations was limited to higher energies because of the limited magnetic field of the superconducting wiggler SCW (i.e., 5.0 T) and the resulting horizontal width of the emitted radiation at higher energies (see, e.g. [2]). While beamline 9 operated by the TU Dortmund is located in the center of the horizontal fan, the spectroscopy beamlines BL8 [3] and BL10 [4] are aligned ± 15 mrad to both sides, so that BL8 and BL10 will directly profit from a higher magnetic field and the resulting increase of the radiation fan horizontal width.

Here we will present first EXAFS experiments at the Pd K-edge (24350 eV) and the Ag K-edge (25514 eV), respectively, measured for an increased magnetic field of 5.6 T in the wiggler and an accordingly larger horizontal radiation fan. The Si(311) monochromator of BL8 was used together with Ar-filled ionization chambers, and Ag and Pd metal foils with different thickness served as samples. A typical scan took about 30 minutes for an energy range of 1400-1600 eV around the related edges. In Fig. 1, an experiment at the Ag K-edge is presented for a 20 μm Ag foil, and in Fig. 2, a 5 μm thick Pd foil was studied.

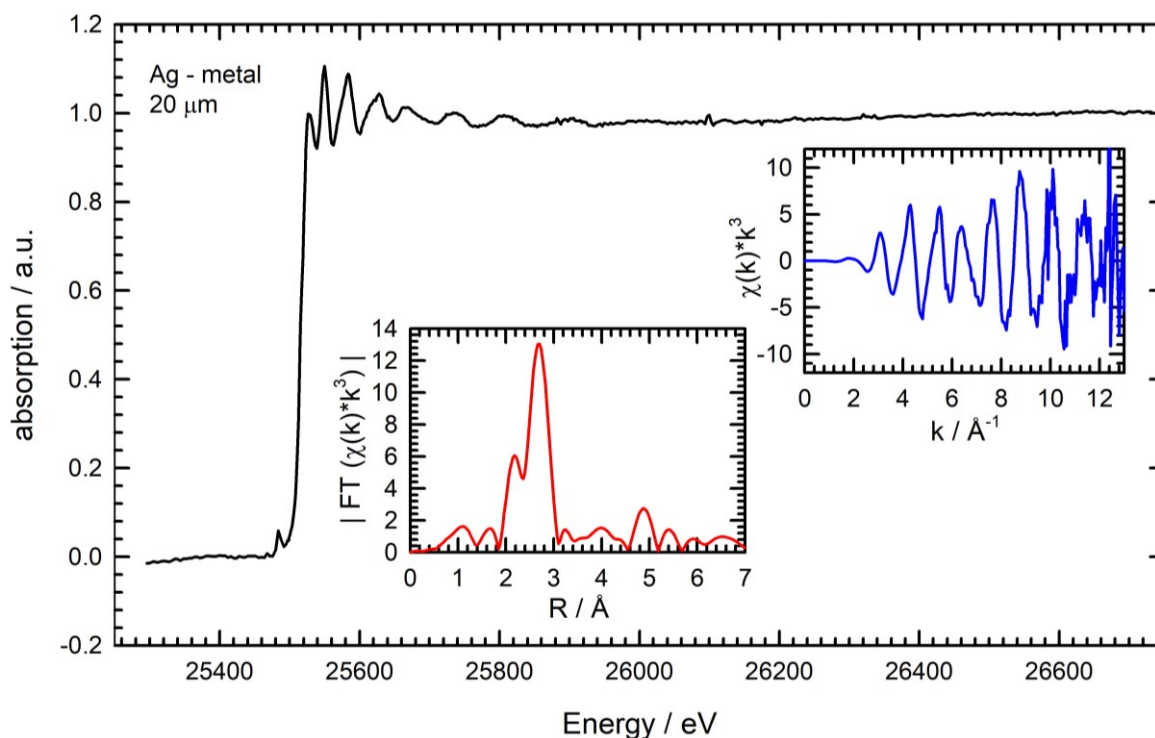


Fig. 1: Example for a transmission mode EXAFS experiment at the Ag K-edge (25514 eV) of a 20 μm Ag metal foil. A scan range of 1600 eV was measured within about 30 minutes of experimental time. In the insets, the extracted k^3 -weighted EXAFS fine structures $\chi(k) \cdot k^3$ as well as the magnitude of the Fourier-transform $|\text{FT}(\chi(k) \cdot k^3)|$ of the data are presented (k -range for the FT: $2.08 \text{ \AA}^{-1} < k < 11.6 \text{ \AA}^{-1}$).

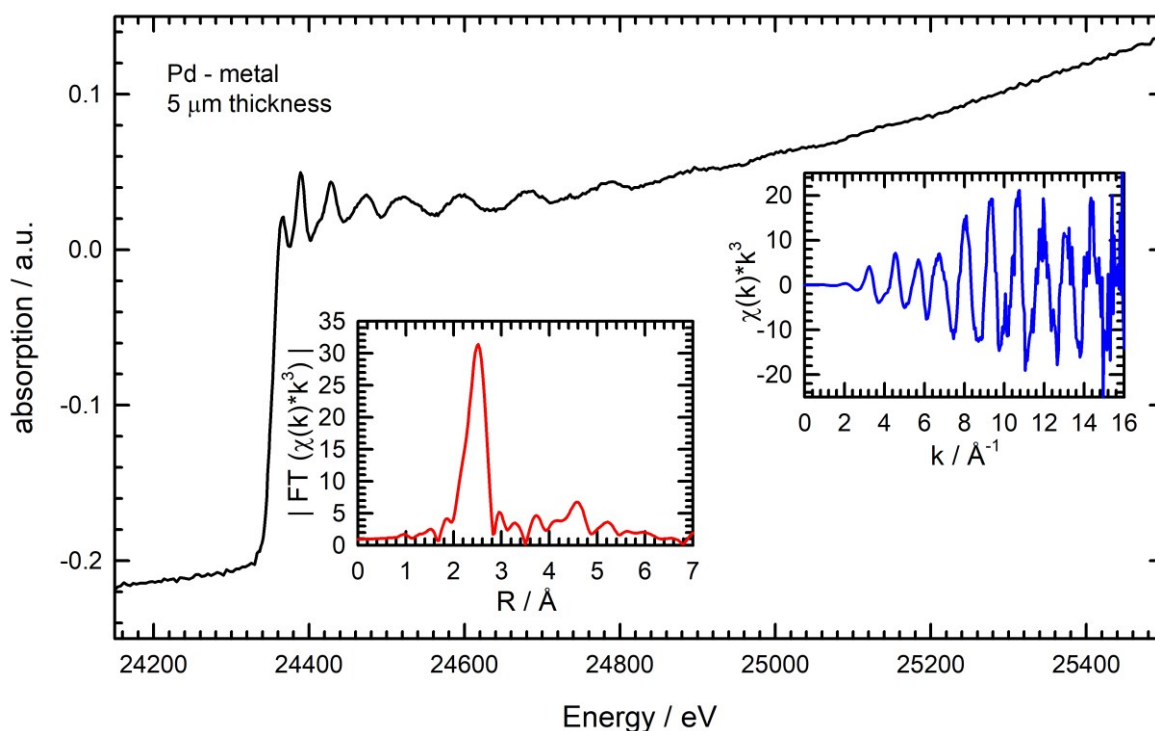


Fig. 2: Example for a transmission mode EXAFS experiment at the Pd K-edge (24350 eV) of a 5 μm Pd metal foil. A scan range of ca. 1400 eV was measured with a total of about 30 minutes of integration time. In the insets, the extracted k^3 -weighted EXAFS fine structures $\chi(k)*k^3$ as well as the magnitude of the Fourier-transform $|FT(\chi(k)*k^3)|$ of the data are presented (k -range for the FT: $1.60 \text{ Å}^{-1} < k < 14.0 \text{ Å}^{-1}$).

Clear fine structure oscillations characteristic for both Ag and Pd are detectable, respectively, and the FT provides information about the nearest neighbor environment of the samples. In particular the measurements from the relatively thin Pd foil with an edge jump of only about 0.2 are very promising for future investigations of real samples such as catalysts, with small concentrations of the active metal center. For example, we plan to conduct experiments on Ag-containing catalyst materials for, e.g. lignin depolymerization [5]. Furthermore, also studies of thin film growth processes by reactive sputtering are planned [6]. Last not least, we will investigate the feasibility of EXAFS experiments at even higher energies such as at the Sn K-edge at 29200 eV, e.g., for structure investigations of superconducting Nb_3Sn thin films [7].

Acknowledgements

We gratefully acknowledge the DELTA machine group for providing synchrotron radiation reliably.

References

- [1] D. C. Koningsberger, R. Prins (Eds.): X-Ray Absorption, Principles, Applications, Techniques of EXAFS, SEXAFS and XANES, John Wiley + Sons, New York, Chichester, Brisbane, Toronto, Singapore 1988.
- [2] S. Khan, B. Büsing, J. Friedl, C. Mai, G. Schmidt, DELTA annual report (2021) 5.
- [3] D. Lützenkirchen-Hecht et al., J. Synchrotron Rad. 16 (2009) 264.
- [4] D. Lützenkirchen-Hecht et al., J. Synchrotron Rad. 21 (2014) 819.
- [5] L. Lindenbeck et al., Polymers 16 (2024) 3325.
- [6] F. Braun et al., Rad. Phys. Chem. 204 (2023) 110707.
- [7] N. Schäfer, et al., J. Appl. Phys. 134 (2023) 043903.

Time-resolved X-ray absorption spectroscopy at DELTA beamline 10

D. Lützenkirchen-Hecht, S. Paripsa, L. Voss, F. Braun, F. Eckelt

Bergische Universität Wuppertal – Fakultät für Mathematik und Naturwissenschaften, Gauß-Str. 20, 42097 Wuppertal, Germany.

In a continuation of previous experiments, we have further investigated the feasibility of time-resolved X-ray absorption spectroscopy (quick-EXAFS) at beamline 10. In general, quick-EXAFS scans are measured on-the-fly, while the monochromator with the channel-cut crystal is moving at a constant speed, and each data point is integrated for some few milliseconds only. This technique is thus eliminating all overheads associated with the normal point-wise detection of an energy scan, resulting in acquisition times in the order of 30 seconds and less for an EXAFS spectrum extending over about 1000 eV, with a scan speed of about 30 eV/s [1, 2]. Therefore, quick-EXAFS is a valuable technique for, e.g., time-resolved investigations of chemical reactions [3], battery charging and discharging [4], and corrosion processes [5].

Thanks to the high photon flux available at the superconducting wiggler at DELTA beamline 10, that has been further improved in 2024 by an increase of the magnetic field of the wiggler from 5.0 T to 5.6 T in the standard user operation, we have analysed the resulting opportunities for time-resolved EXAFS studies accordingly. Here, a 5 μm thick gold foil served as a model sample, and spectra were collected for different scan speeds and scan ranges covering the L-edges of gold (11919 eV, 13734 eV, and 14353 eV, respectively). While the ionization chamber in front of the sample was filled with nitrogen at atmospheric pressure, the second ionization chamber behind the sample was filled with argon. In Fig. 1, some selected spectra measured with different scan speeds are presented. The integration time per data point was set to 50 ms, 10 ms and 7 ms, respectively, to lead to an adequate number of data points in the scan, i.e., a step width substantially smaller than 1 eV. As can be seen, an increase in the scan speed from ca. 16.9 eV/s (resulting in a total time of about 70 s for a single spectrum), to 66.5 eV/s (18 s) and 100 eV/s (12 s) does not lead to a smearing of the features in the edge or much more noisier absorption fine structure data $k^3 \cdot \chi(k)$, as can be seen in the insert in Fig. 1. Clear fine structure oscillations are detectable up to ca. 16 \AA^{-1} above the edge, allowing a meaningful EXAFS data analysis.

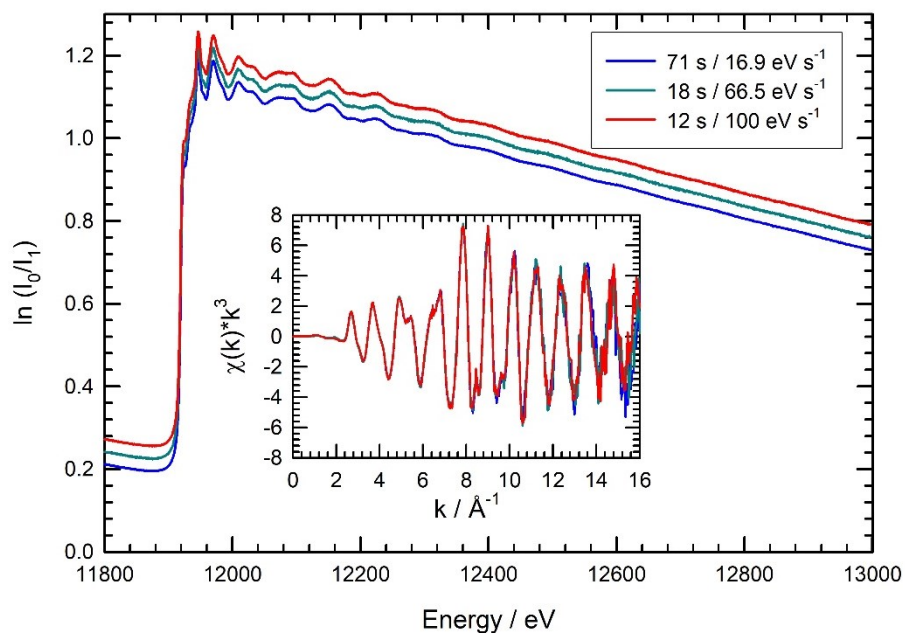


Fig. 1: Quick-scanning Au L3-edge EXAFS measurements of a 5 μm thick gold foil in transmission mode at room temperature for different scan speeds as indicated. In the insert, the k^3 -weighted EXAFS fine structures $\chi(k) \cdot k^3$ extracted at the Au L3-edge are shown.

In a second series of experiments, the energy width of the spectra was extended, so that not only the L3-edge is scanned, but also the L2 and the L1 edge, respectively. Some selected data are presented in Fig. 2, with the last scan covering 3700 eV in energy within 30 s only. Again, an excellent data quality was obtained, as can be deduced from the fine structures extracted at the L1-edge, that are shown in the insert. Keeping in mind that the edge step at the L1-edge is only 20% of that at the L3-edge, and an accordingly reduced intensity of the extracted EXAFS oscillations $\chi(k)*k^2$, the obtained results are very promising for investigations of multi-elemental samples such as high- and medium-entropy alloys [6], or other complex materials such as batteries [7] or catalysts in time-resolved EXAFS experiments.

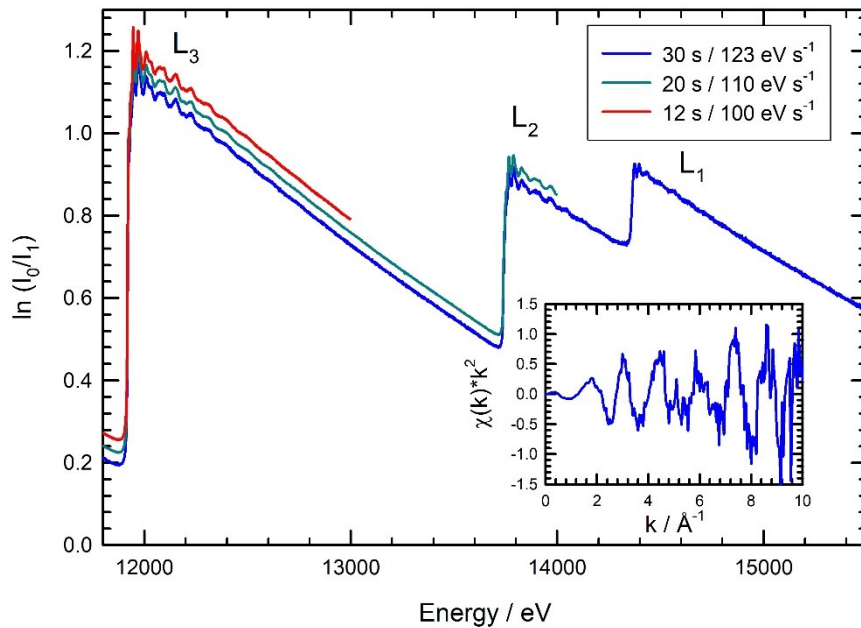


Fig. 2: Gold L-edges measured within about 10 seconds per edge, corresponding to about 100 eV s⁻¹ scan rate, and an integration time of 7 ms for each data point in the spectrum. In the inset, the EXAFS oscillations $\chi(k)*k^2$ extracted at the Au L1-edge are provided.

Acknowledgements:

The authors like to thank the DELTA machine group for the delivery of a high-quality beam.

References:

- [1] R. Frahm, Nucl. Instrum. Methods Phys. Res. A 270 (1988) 578.
- [2] D. Lützenkirchen-Hecht, S. Paripsa, L. Voss, F. Braun, F. Eckelt, DELTA annual report (2023), p. 23.
- [3] F. Eckelt, P. Rothweiler, L. Voss, et al., Materials 15 (2022) 8186.
- [4] G. Aquilanti, M. Giorgetti, R. Dominko, et al., J. Phys. D: Appl. Phys. 50 (2017) 074001
- [5] D. Lützenkirchen-Hecht, R. Frahm, J. Phys. Chem. B 105 (2001) 9988.
- [6] T. Trompeter, X. Tang, K. Yuan, Y. Chen, D. Lützenkirchen-Hecht, DELTA annual report (2023), p. 121.
- [7] L. M. Lindenbeck, D. Lützenkirchen-Hecht, A. Drichel, B. B. Beele, B. V. M. Rodrigues, A. Slabon, DELTA annual report (2024).

X-ray Scattering

An X-ray diffraction study on the structure of neat linear alkylamines

Lena Friedrich¹, Michael Paulus¹, Aurélien Perera², Martina Požar³, Christian Sternemann¹

¹Fakultät Physik/DELTA, TU Dortmund University, 44221 Dortmund, Germany

²Sorbonne Université, Laboratoire de Physique Théorique de la Matière Condensée (UMR CNRS 7600), F75252, Paris cedex 05, France ³University of Split, Faculty of Science, 21000 Split, Croatia

Amines are associative liquids capable of forming supramolecular structures through hydrogen bonding [1], which is essential for biochemical processes, providing stability in biomolecules like proteins and peptides and playing a key role in structuring molecular liquids [2]. Amines, significant in industrial applications and pharmaceuticals, are used in processes like amine scrubbing to remove gases such as hydrogen sulfide and carbon dioxide [3]. A frequently studied class of compounds that also form supramolecular structures through hydrogen bonding are monohydroxy alcohols [4-6]. Although linear amines and mono-ols share structural similarity due to their alkyl tail, significant differences are observed in their X-ray diffraction (XRD) patterns, namely the difference in the intensity of the so-called pre-peak. In this study, the reason for the weak expression of the pre-peak of the amines in comparison to that in the mono-ols is investigated with the aid of XRD studies and calculations of the scattering intensities based on computer simulation data [7].

The linear amines propylamine, butylamine, pentylamine, hexylamine, heptylamine, octylamine and nonylamine were filled into borosilicate glass capillaries with a diameter of 1.5 mm. The wide-angle XRD experiments were performed at BL9 at DELTA with an incident energy of 20 keV ($\lambda = 0.61992 \text{ \AA}$). For detection a MAR345 image plate scanner was used. Measurements were also taken both in air and with a helium pathway to reduce background scattering. Additional small-angle X-ray scattering (SAXS) measurements for propylamine to octylamine were carried out at an energy of 12 keV at BL2 at DELTA.

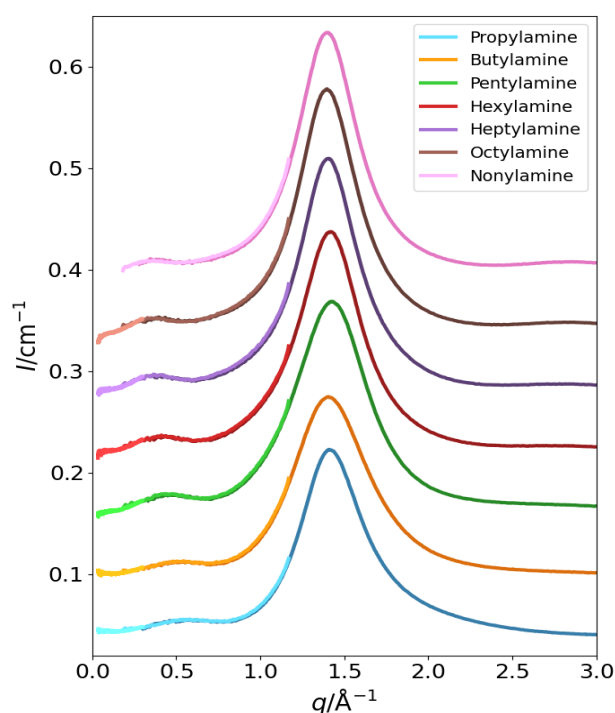


Figure 1: XRD patterns of propylamine to nonylamine. The different shades of color represent the different measurements: SAXS (lightest shade), WAXS with He pathway (medium shade) and WAXS with air scattering (darkest shade). The graphs are shifted vertically for better visibility.

The diffraction patterns of propylamine to nonylamine are shown in Fig. 1. The combined pattern of SAXS and the two WAXS measurements (with and without a He path) is displayed. In addition to the main peak typical of liquids, a broad, flat pre-peak can be seen. The main peak's position can be found at around 1.4 \AA^{-1} and is the result of atom-atom correlations typical for liquids. The pre-peak position shifts to smaller wave vector transfer q with increasing carbon chain length from propylamine to nonylamine. The occurrence of a pre-peak is typical for transient molecular association and indicates a supramolecular structure formation. Its position ranges from about 0.54 to 0.36 \AA^{-1} . Interestingly, the pre-peak is significantly weaker in intensity than in previously studied mono-ols which indicates a reduced clustering [6].

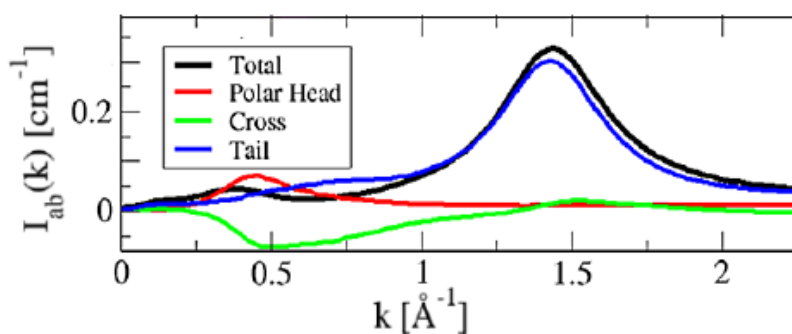


Figure 1: Breakdown of the intensity into head group contribution (red), alkyl chain contribution (blue) and mixed contribution (green) using octylamine as an example. The total intensity is shown in black. Modified from [7].

To further investigate the reason for the significant difference in the pre-peak behavior between amines and mono-ols, calculations of the diffraction intensities based on molecular dynamics simulations were carried out [7]. Figure 2 shows the calculated partial scattering contributions for octylamine. In black the total scattering intensity is displayed as a function of the wave vector

k which shows only a flat pre-peak. This is due to the polar head (red) and cross correlation (green) contributions which exhibit significant features in the vicinity of the pre-peak's q -range with opposite sign, so that they strongly cancel out, causing only a small pre-peak in the total intensity patterns. Moreover, it is found that owing to the fact that the amines have a more restricted geometry for formation of hydrogen bonds caused by the amine head group in comparison to the linear hydroxyl group, the formation of larger clusters is suppressed, which is in strong contrast to the observations for mono-ols. A detailed analysis and discussion of the results can be found in a recent publication [7].

References

- [1] L. Almásy, A. Kuklin, M. Požar, A. Baptista and A. Perera. Microscopic origin of the scattering pre-peak in aqueous propylamine mixtures: X-ray and neutron experiments versus simulations. *Physical Chemistry Chemical Physics*, 21:9317–9325, 2019.
- [2] A. Babusyte, M. Kotthoff, J. Fiedler and D. Krautwurst. Biogenic amines activate blood leukocytes via trace amine-associated receptors taar1 and taar2. *Journal of Leukocyte Biology*, 93:387–394, 2013.
- [3] S. Faramawy, T. Zaki and A. Sakr. Natural gas origin, composition, and processing: A review. *Journal of Natural Gas Science and Engineering*, 34:34–54, 2016.
- [4] F. Palombo, P. Sassi, M. Paolantoni, A. Morresi and R. S. Cataliotti. Comparison of hydrogen bonding in 1-octanol and 2-octanol as probed by spectroscopic techniques. *The Journal of Physical Chemistry B*, 110:18017–1805, 2006.
- [5] T. Kosztolányi, I. Bakó and G. Pálinkás. Hydrogen bonding in liquid methanol, methylamine, and methanethiol studied by molecular-dynamics simulations. *The Journal of Chemical Physics*, 118:4546–4555, 2003.
- [6] M. Požar, J. Bolle, C. Sternemann and A. Perera. On the x-ray scattering pre-peak of linear mono-ols and the related microstructure from computer simulations. *The Journal of Physical Chemistry B*, 124:8358–8371, 2020.
- [7] M. Požar, L. Friedrich, T. Millet, M. Paulus, C. Sternemann and A. Perera. Microscopic Structure of Neat Linear Alkylamine Liquids: An X-Ray Scattering and Computer Simulation Study. *The Journal of Physical Chemistry B*, 128:10925–10936, 2024.

Acknowledgments

The authors gratefully acknowledge the support of the Bundesministerium für Bildung und Forschung (BMBF) for funding via DAAD in the scope of the French-German collaboration PROCOPE 2024-2025 (Project-IDs 57704875 and 50951YA).

Structural changes of entangled and disentangled UHMWPE powders during melting

Ulrich A. Handge, Christopher Krüsener, Louisa Neumann
(Chair of Plastics Technology, TU Dortmund)

Gerrit A. Luinstra, Adrian Vaghar
(Institute of Technical and Macromolecular Chemistry, University of Hamburg)

Christian Sternemann, Michael Paulus
(Fakultät Physik/DELTA, TU Dortmund)

Ultra-high molecular weight polyethylene (UHMWPE) is a polymer with a high number of entanglements because of its high molecular weight. Consequently, UHMWPE is associated with a pronounced elasticity. The elastic properties of UHMWPE have a significant contribution to its flow behavior. Furthermore, the high number of entanglements leads to a lower crystallinity compared to a polyethylene (PE) with a lower molecular weight. A so-called disentangled UHMWPE (*dis*-UHMWPE) has a lower number of entanglements than conventional UHMWPE. Therefore, the viscosity shortly after melting should be reduced which facilitates processing.

In our work, we focused on the dynamics of melting of a *dis*-UHMWPE in comparison to conventional UHMWPE grades. Small angle and wide angle X-ray scattering (SAXS/WAXS) were carried out in order to elucidate the temporal evolution of the microstructure during melting of these UHMWPE grades with different degrees of entanglements.

WAXS measurements were performed at beamline BL9 of the DELTA synchrotron radiation source. For static measurements we applied the MAR345 image plate detector at a distance of about 330 mm from the sample position to cover the amorphous peak together with the [110] and [200] reflections of polyethylene. The incident X-ray energy was set to 27 keV and a beam size of $0.8 \times 0.7 \text{ mm}^2$ (h x v) was used. The samples were prepared in sealed glass capillaries of 1.5 mm diameter and mounted into a Linkam stage temperature-control unit. The SAXS investigations were carried out at beamline BL2 utilized with the corresponding MAR345 detector setup with an incident energy of 12 keV and a beam size of $0.5 \times 0.5 \text{ mm}^2$. Sample treatment and temperature control was identical to the WAXS experiments.

Both, SAXS and WAXS data show differences between *dis*-UHMWPE and commercial UHMWPE. SAXS data revealed the highest long period for the *dis*-UHMWPE, which results from a higher crystallinity and a high molecular weight.

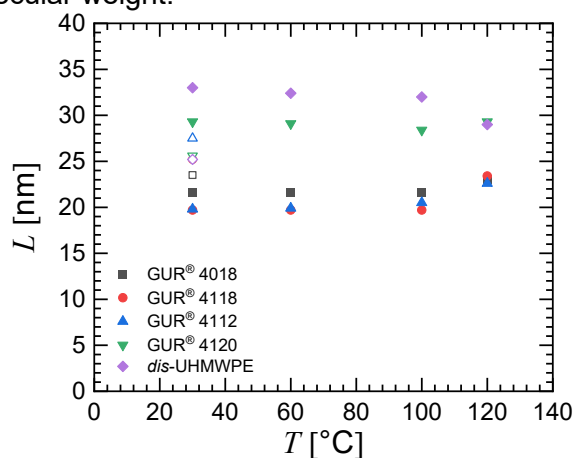


Figure 1. Long period L as a function of temperature T for the polyethylene grades with different average molecular weights. The open symbols reflect the state after recrystallization. The molecular weights are $0.6 \times 10^6 \text{ g/mol}$ for GUR 4018 and 4118, $1.7 \times 10^6 \text{ g/mol}$ for GUR 4112, $1.9 \times 10^6 \text{ g/mol}$ for *dis*-UHMWPE and 4.7×10^6 for GUR 4120.

WAXS data revealed one major difference, which was not observed before. During the first heating of the nascent *dis*-UHMWPE, the intensity of the [110] and [200] peaks of the WAXS data first decrease and then increase again with temperature at about 80°C. On the contrary, during the second heating of *dis*-UHMWPE the Bragg peaks monotonically decrease with temperature. For the conventional UHMWPE grades we observe the onset of the intensity increase only at much higher temperature about 120°C at first heating.

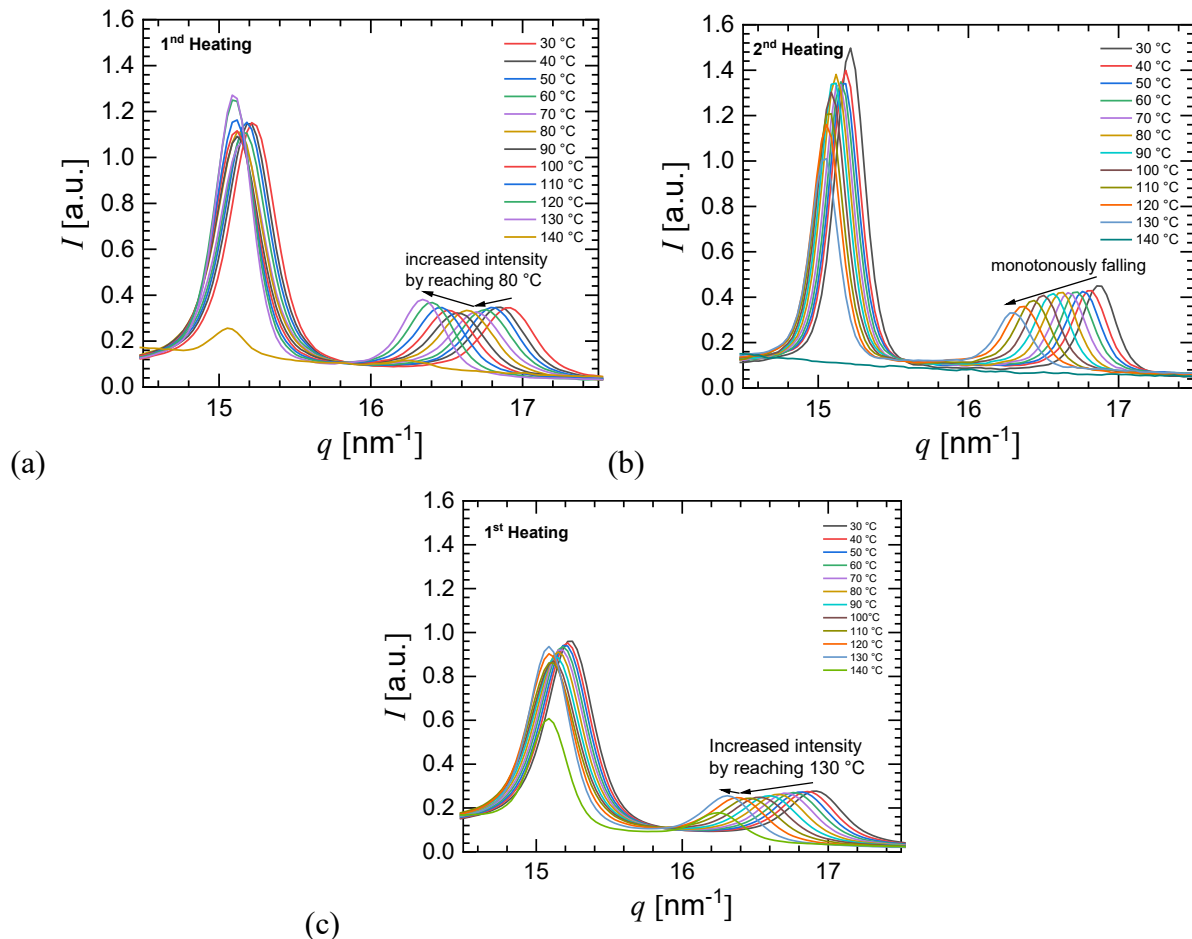


Figure 2. WAXS pattern as function of temperature for (a) first and (b) second heating of *dis*-UHMWPE and (c) first heating of GUR® 4120

We interpret this effect by a local rearrangement of chain segments and a growth of existing crystals during heating of nascent *dis*-UHMWPE. This is verified by the fact that the crystal size, which was calculated by using Scherrer's equation, starts to increase at 80 °C for *dis*-UHMWPE. For the commercial UHMWPE a higher temperature is needed to initiate the growth of crystals, because of the higher number of entanglements the mobility is only sufficiently high at a higher temperature. Consequently, during the first heating cycle the remaining crystallinity of the commercial UHMWPE at 140 °C is higher, because the mobility is so restricted that more time/temperature is needed to initiate melting. This effect is denoted as "superheating" for UHMWPE and is less pronounced for the *dis*-UHMWPE, because of its higher mobility.

Influence of perfluorodecalin on the structure of proteins and lipid vesicles

Jaqueline Savelkouls^{1*} and Michael Paulus¹

¹Technische Universität Dortmund, Fakultät Physik / DELTA, 44227 Dortmund, Germany

*jaqueline.savelkouls@tu-dortmund.de

Multilamellar lipid vesicles and proteins play a central role in biomedical research due to their unique properties and various applications. Lipid vesicles serve as useful models for the study of biological membranes and are also of interest for targeted drug delivery [1,2].

Human serum albumin (HSA) is the most common protein in human blood plasma and can bind various molecules such as drugs, fatty acids, and hormones, making it an important model protein for transport and release studies [3-7].

Perfluorocarbons (PFCs) such as perfluorodecalin (F-Decalin) are also of great interest in research for biomedical applications due to their physicochemical properties. PFCs are characterized by their high oxygen solubility and inertness, which makes them ideal candidates for applications such as oxygen transport and diagnostics [8]. The combination with lipid vesicles or transport proteins enables the development of innovative systems for targeted drug delivery, oxygen therapies and imaging techniques that can potentially increase the effectiveness of modern therapies [8]. However, the interaction between these three components is currently relatively poorly understood.

To investigate the interactions between F-Decalin and possible transport vehicles, the small-angle X-ray scattering method (SAXS), which was carried out on beamline BL2 [9], is used.

For the study, HSA (CAS number: 70024-90-7, Sigma-Aldrich) was used at a concentration of 10 mg/ml dissolved in Sørensen buffer [10]. On the other hand, multilamellar vesicles were produced from the zwitterionic lipid 1,2-dipalmitoyl-sn-glycero-3-phosphocholine (DPPC) (CAS number: 63-89-8, Avanti). The powdered DPPC was dried in a rotary evaporator for several hours and then dissolved in Sørensen Buffer in an ultrasonic bath to form multilamellar vesicles. The resulting sample solutions were then measured using SAXS and subsequently flushed with F-Decalin (CAS number: 306-94-5, Sigma-Aldrich)-saturated nitrogen for a limited period.

The prepared samples were then filled into a borosilicate glass capillary (\varnothing 1.5 mm) and were placed in a temperature-controlled sample environment (Linkam Stage) [11]. All SAXS measurements were performed at a temperature of 25 °C. SAXS images were acquired with an exposure time of 350 s. The SAXS data were detected by a MAR345 image plate detector (marXperts, Norderstedt, Germany) at an incident photon energy of 12 keV with a beam size at the sample position of (0.5 x 0.5) mm² (h x v) and a sample detector distance of 1562 mm. Measurements were also carried out in a pure buffer solution to determine the scattering background.

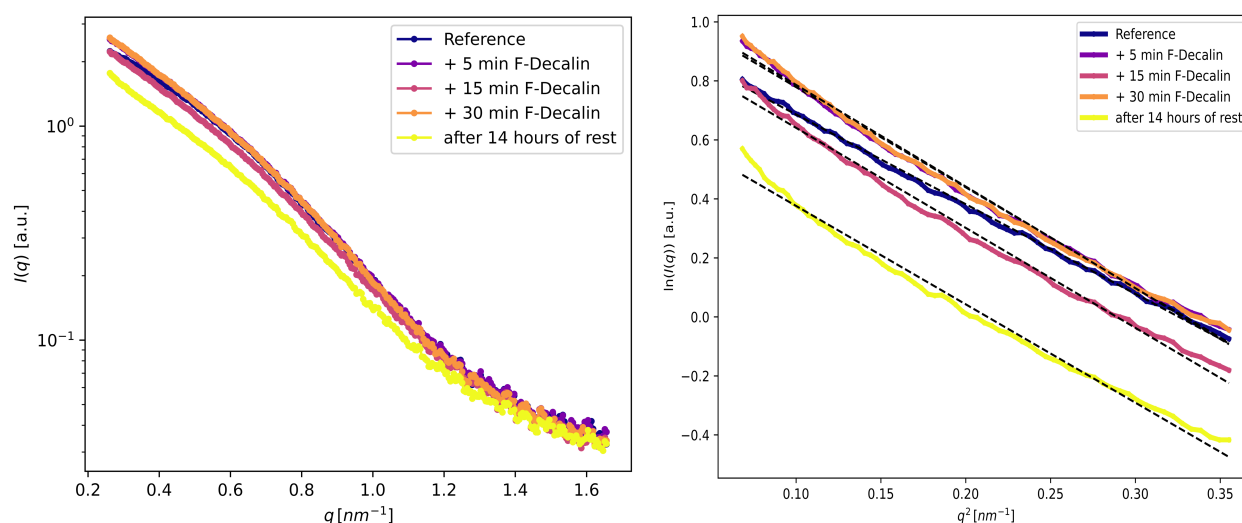


Figure 1: Left: SAXS data of HSA before and after flushing with F-Decalin. Right: The Guinier regions with the corresponding fit to the data (black lines).

First, the influence of F-Decalin on the protein structure of the HSA was analyzed. The corresponding SAXS curves are shown in Figure 1 (left), while the resulting Guinier regions with the corresponding fit

to the data (black lines) are shown on the right. The sample solution was analyzed once before flushing with F-Decalin and then after flushing for different lengths of time.

The curve in the Guinier range shows a linear behavior for the untreated HSA, which indicates a monodisperse system. A fitting results in a gyration radius of $R_G = (2.88 \pm 0.01)$ nm. After the addition of F-Decalin, however, there is a clear deviation from the linear course, especially at low q values where the intensity increases significantly. This clearly indicates a polydisperse system, which contains large clusters due to aggregation of the proteins. A simple radius of gyration is therefore no longer meaningful. Even if the sample is stored in an air atmosphere for 14 hours after treatment with F-Decalin, the aggregation can no longer be reversed, which indicates an irreversible disruption of the protein structure by the F-Decalin. The destabilizing effect of F-Decalin was also observed with the protein lysozyme (data not shown).

Finally, the influence of F-Decalin on multilamellar DPPC vesicles was investigated. The corresponding SAXS signal is shown in Figure 2. Based on the positions of the three Bragg reflections, a regular lamellar structure and an approximate diameter of the multilamellar vesicle of approx. 382.68 Å can be assumed. After the reference measurement, the system was flushed once with F-Decalin for 2 minutes and then again for 10 minutes. The sample was measured again after each flush. It can be seen that after flushing with F-Decalin, the regular lamellar structure of the vesicle remained the same. Only the half-widths decrease minimally, which would indicate improved order and homogeneity. Consequently, a slight stabilisation effect of F-Decalin can be inferred. Furthermore, the peak positions shift minimally to higher q -values, which is accompanied by a decrease in the distance between neighboring layers of the multilamellar vesicles, suggesting more densely packed layers. After a further rinse with F-Decalin, these effects are minimally reduced again.

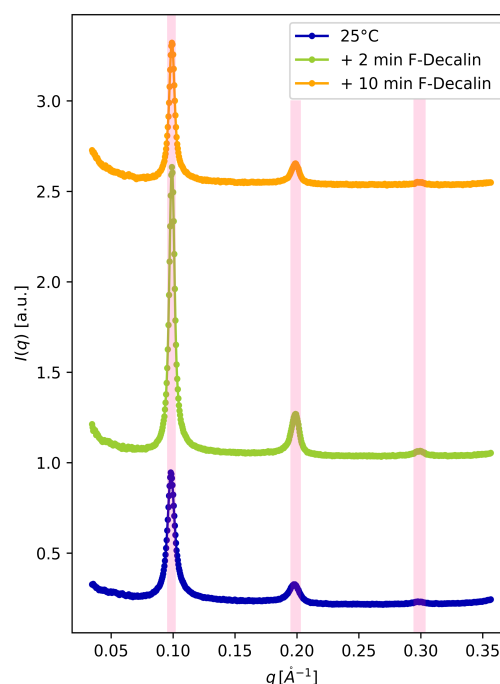


Figure 2: SAXS data of multilamellar DPPC vesicles before and after flushing with F-Decalin.

In summary, it can be concluded that F-Decalin has a destabilizing effect on proteins, while it might have a minimal stabilizing effect on the lipid vesicles but causes no other significant structural changes.

References

- [1] Chem Phys Lipids. 1986 Jun-Jul;40(2-4):145-66. doi: 10.1016/0009-3084(86)90068-x.
- [2] H. M. G. Barriga et al. Angew. Chem. 2019, 131, 2984 – 3006, Doi: 10.1002/anie.201804067
- [3] S. Curry, P. Brick, N. P. Franks, Biochimica et Biophysica Acta. 1999, 1441, pp. 131-140
- [4] M. Paul, A. M. Itoo, B. Ghosh, S. Biswas, Expert Opinion on Drug Delivery. 2022, 19, pp. 1449-1470
- [5] C. Li, D. Zhang, Y. Pan, B. Chen, Polymers. 2023, 15, 3354, DOI: 10.3390/polym15163354
- [6] J. Wasko, M. Wolszczak, Z. Zajaczkowska, M. Dudek, B. Kolesinska, Bioorganic Chemistry 2024, 143, 107104
- [7] D. Shastri, V. Raj, S. Lee, Ageing Research Reviews 2024, 99, 102379
- [8] N. Kakaei et al., Front Bioeng Biotechnol. 2023 Aug 3;11:1115254. doi: 10.3389/fbioe.2023.1115254
- [9] M. Dargasz, J. Bolle, A. Faulstich, E. Schneider, M. Kowalski, C. Sternemann, J. Savelkoul, B. Mur-phy, M. Paulus, Journal of Physics: Conference Series 2380, 012031, 2022
- [10] <http://www.aeisner.de/rezefte/puffer2.html>
- [11] <https://www.linkam.co.uk/thms350v>

Acknowledgments We thank the DELTA machine group for providing synchrotron radiation.

Influence of ibuprofen on the pressure stability of human serum albumin

Jaqueline Savelkouls^{1*}, Eric Schneider¹, Chang Hee Whoo¹ and Michael Paulus¹

¹Technische Universität Dortmund, Fakultät Physik / DELTA, 44227 Dortmund, Germany

*jaqueline.savelkouls@tu-dortmund.de

The globular protein human serum albumin (HSA) is the most frequently occurring protein in the human blood, which contributes to the osmotic colloid pressure, regulates the blood pH and acts as a plasma transporter for various substances [1-3]. Due to its ability to bind and transport hydrophobic substances through the bloodstream, it is of particular interest in medicine and pharmacy as a potential nanocarrier for various drugs [4-7]. For example, Abraxane is a drug where nanoparticles of HSA are produced under high hydrostatic pressure [8].

To investigate the interactions between hydrophobic substances and the protein, pressure-dependent measurements using the small-angle X-ray scattering (SAXS) method were performed at beamline BL2 [9]. The pressure-dependent measurements serve as an indirect indicator of the interaction between the substances and the protein, via the denaturation behavior of the proteins.

For the study, HSA (CAS number: 70024-90-7, Sigma-Aldrich) was used at a concentration of 10 mg/ml in pressure-stable 25 mM Bis-Tris buffer (CAS number: 6976-37-0, Sigma-Aldrich). In addition, 5 mM ibuprofen (CAS number: 15687-27-1, Sigma-Aldrich) were added in solubilized form. The prepared samples were then filled into sample holders and placed directly into the high-pressure cell [10]. All pressure dependent SAXS measurements were performed at a temperature of 25 °C. After closing the pressure cell, the pressure was increased in steps of 250 bar to a final pressure of 3500 bar and SAXS images were acquired with an exposure time of 300 s each. The SAXS data were collected using a MAR345 image plate detector (marXperts, Norderstedt, Germany) at an incident photon energy of 12 keV with a beam size at the sample position of (0.5 x 0.5) mm² (h x v) and a sample detector distance of 1568 mm.

The pressure-dependent SAXS data for the fatty acid-free HSA (A3782) and HSA (A8763) mixed with fatty acid are presented as examples in Figure 1. Furthermore, the calculated Guinier plots are presented in the inset plots. At low pressures, the typical shape curve of a globular protein can be identified in both cases. At higher pressures, the curves reveal a shift in the slope, with the fatty acid-free HSA showing a change at $p = 1000$ bar and the HSA at $p = 2500$ bar. At these specified pressure points, the proteins lose their typical globular shape. Additionally, a change in the slope can be observed in the Guinier region too, indicating an increase in the radius of gyration. Moreover, a reduction in intensity is noted, which can be attributed to a decrease in the scattering contrast between the protein and the compressed water phase.

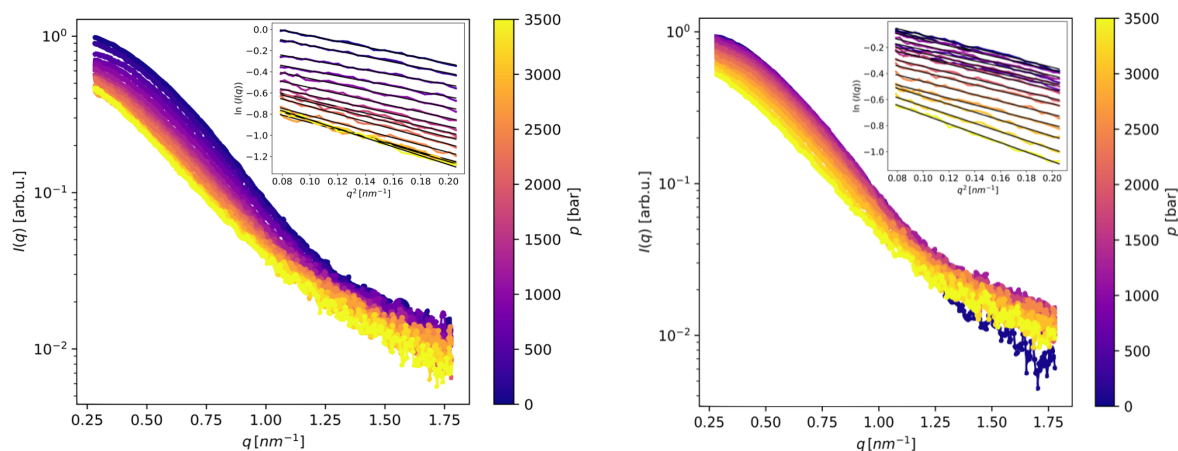


Figure 1: Pressure-dependent SAXS data of the samples HAS A3782 (left, fatty acid free) and HSA A8763 (right). The insets show the Guinier regions with corresponding fit to the data (black lines).

The pressure-dependent radius of gyration, which were determined by a Guinier analysis of the SAXS data at low q values is shown in figure 2. As can be observed, the radius of gyration at ambient pressure

is found to be approximately $R_g = 2.9$ nm for all samples, which is in accordance with the documented characteristics of a folded heart-shaped structure of human serum albumin (HSA) [11].

Furthermore, it is notable that the structure of the fatty acid free HSA remains stable only up to about 1000 bar. This is evidenced by a significant increase in the radius of gyration above 1000 bar up to $R_g = 3.3$ nm, which indicates denaturation. At higher hydrostatic pressures, a slight unfolding of the protein structure into the F-Form occurs [12], caused by the penetration of solvent molecules into the cavities of the HSA protein [13]. In comparison, HSA mixed with fatty acid stays stable up to 2500 bar.

Meanwhile, the structure of the fatty acid-free protein remains unaffected over the entire pressure range when the drug ibuprofen is added. It can therefore be concluded that hydrophobic substances such as ibuprofen increase the pressure stability of the protein structure.

The main reason for this is the interaction of the hydrophobic substances with the hydrophobic core of the HSA. Depending on the geometry and hydrophobicity of the added substance, the cavity volume of the protein is filled to a higher level so that by increasing the pressure fewer solvent molecules can penetrate and the protein structure is not affected.

A more detailed description of the results and the influence of other hydrophobic substances such as caffeine or histamine can be found in the following article [14].

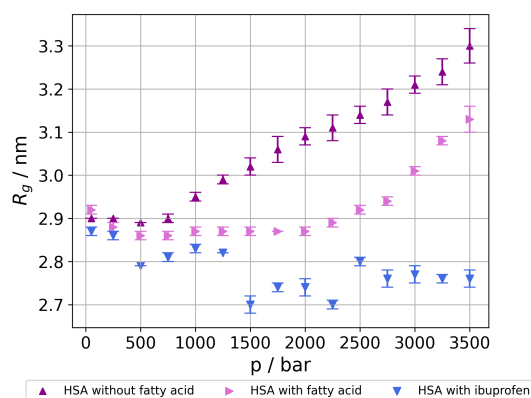


Figure 2: Pressure-dependent radius of gyration, which were determined by a Guinier analysis of the SAXS data at low q values.

References

- [1] D. C. Carter, J. X Ho, *Advances in protein chemistry*. 1994, 45, pp. 153–203,
- [2] T. Peters Jr., *Advances in Protein Chemistry*. 1985, 37, pp.161-245, 9780120342372
- [3] S. Curry, P. Brick, N. P. Franks, *Biochimica et Biophysica Acta*. 1999, 1441, pp. 131-140
- [4] M. Paul, A. M. Itoo, B. Ghosh, S. Biswas, *Expert Opinion on Drug Delivery*. 2022, 19, pp. 1449-1470
- [5] C. Li, D. Zhang, Y. Pan, B. Chen, *Polymers*. 2023, 15, 3354, DOI: 10.3390/polym15163354
- [6] J. Wasko, M. Wolszczak, Z. Zajaczkowska, M. Dudek, B. Kolesinska, *Bioorganic Chemistry* 2024, 143, 107104
- [7] D. Shastri, V. Raj, S. Lee, *Ageing Research Reviews* 2024, 99, 102379
- [8] Jonas Kaltbeitzel and Peter R. Wich, *Angew. Chem. Int. Ed.* 2023, 62, e202216097
- [9] M. Dargasz, J. Bolle, A. Faulstich, E. Schneider, M. Kowalski, C. Sternemann, J. Savelkouls, B. Mur-phy, M. Paulus, *Journal of Physics: Conference Series* 2380, 012031, 2022
- [10] C. Krywka, C. Sternemann, M. Paulus, M. Tolan, R. Royer, R. Winter, *ChemPhysChem*, 2008, 9, 2809
- [11] C. E. Merzougui, P. Roblin, P. Aimar, A. Venault, Y. Chang, C. Causserand, P. Bacchin, *Soft Matter* 2020, 16, 9964.
- [12] Ted Lee, Kenneth A. Smith, and T. Alan Hatton *Biochemistry* **2005** 44 (2), 524-536 DOI: 10.1021/bi048556c
- [13] J. Roche and C. A. Royer, *Interface*. 2018, 15, 20180244
- [14] J. Savelkouls, E. Schneider, C. Whoo, M. Paulus, *Phys. Status Solidi A*, 2024, 2400608, DOI: 10.1002/pssa.202400608

Acknowledgments We thank the DELTA machine group for providing synchrotron radiation.

The concentration-dependent structure factor of dextran and Ficoll®

Michael Paulus¹, Michelle Dargasz², Jaqueline Savelkous¹, Chang Hee Woo¹,

Christian Gutt²

¹Fakultät Physik/DELTA, TU Dortmund, 44221 Dortmund, Germany

²Department Physik, Universität Siegen, Walter-Flex-Str. 2, 57072 Siegen, Germany

In living organisms, proteins are important building blocks that can take on many different functions. They often move in densely packed environments and constantly interact with many other molecules. In order to investigate protein dynamics in cell-like systems, for example using X-ray photon correlation spectroscopy (XPCS), various sugars can be used as model

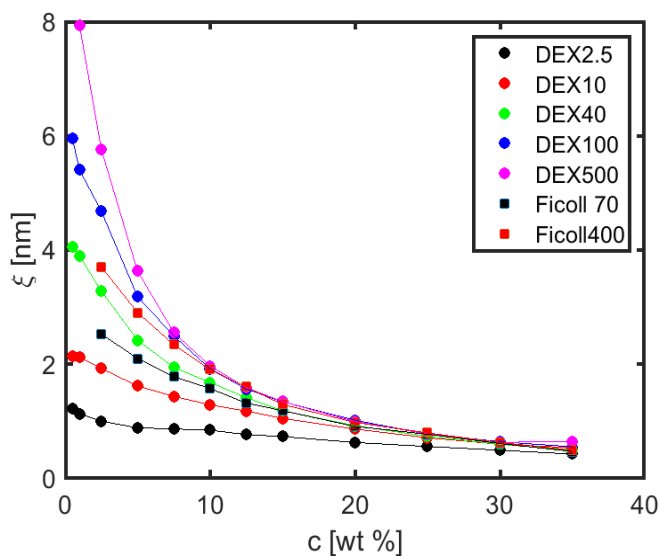
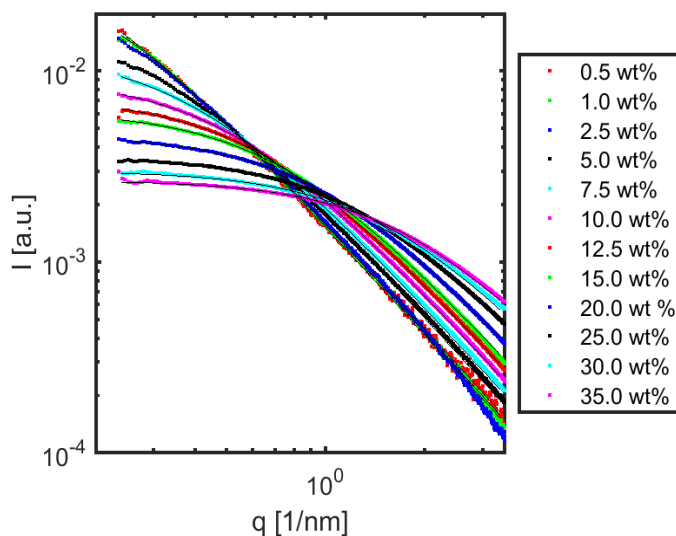


Figure 1, top: Concentration-dependent SAXS data of DEX100 in aqueous solution. The lines show the fit by equation 1. Bottom: Correlation lengths obtained from the fit of equation 1 for the different samples.

molecules that do not interact specifically with the proteins, but mainly restrict the space available for protein diffusion. Typical representatives are, for example, dextrans which consist of branched chains of polysaccharides. The chain length can vary significantly depending on the molecular weight of the dextran. Dextrans are highly soluble in water and are used in medicine as well as in the manufacture of cosmetic products due to their biocompatibility. Another macromolecule that can be used in the study of densely packed environments is so called Ficoll®, a sucrose epichlorohydrin copolymer which is also used in medicine. Compared to dextran, it is more highly branched and therefore has a more compact structure in aqueous solution.

In small-angle X-ray scattering (SAXS) experiments, the structure factor $S(q)$ of well soluble polymer chains in aqueous solution can be described by

$$S(q) = S(0) / (1 + (q\xi)^b) \quad (1)$$

with the wave vector transfer q , the correlation length ξ and the exponent b , which varies between 1.7 and 2 depending on

the polymer chain. If the polymers are highly diluted in aqueous solution, ξ is linked to the radius of gyration of the polymer chain, while increasing polymer concentration can lead to an overlap of the individual chains and ξ only describes the space available for a single chain segment. ξ is therefore a variable that is strongly dependent on the concentration of the polymer in solution.

At the beamline BL2, various dextrans (DEX2.5, DEX10, DEX40, DEX100 and DEX500, where the number stands for kg/mol) as well as Ficoll[®] 70 and Ficoll[®] 400 were investigated in aqueous solution as a function of concentration using SAXS. Concentrations in a range between 1 wt% and 35 wt% were used. The photon energy was 12 keV and the sample-to-detector distance was about 1.5 m. The beam size was set to 0.8 x 0.8 mm². The exposure time was between 60 s and 180 s, depending on the concentration of the polymer. To determine the scattering background, a scattering profile of pure water was recorded and the scattering intensity was subtracted from the measurements with polymer. Figure 1, top shows an example of a concentration series for the DEX100. The data was normalized to the integral of the total scattering intensity. All data were fitted using equation 1. It was found that for all dextrans the decrease in intensity in the Porod-region (high q) scaled with $b=1.91$ while for both Ficoll[®] samples $b= 2.6$ was found, indicating a more compact structure of Ficoll[®] compared to the dextrans. Figure 1, bottom shows the correlation lengths of the different polymers resulting from the fits of equation 1 as a function of concentration. It is clear that at low polymer concentrations there are strong differences between the observed correlation lengths ξ , which are caused by the different molecular weight of the polymers. However, as the concentration increases and the polymer chains touch each other, the different molecular weights and polymer types become less important and all the curves overlap.

The results obtained from this study will now be used in a further step to interpret the dynamics of proteins in a crowded environment measured at the European XFEL.

Acknowledgments We thank the DELTA machine group for providing synchrotron radiation.

Probing the structural evolution of starch solutions during gelation

Mohammad Agha Raza¹, Michelle Dargasz¹, Jaqueline Savelkouls², Michael Paulus²,
Christian Gutt¹

¹Department of Physics / X-ray science, Universität Siegen, 57076 Siegen, Germany

²Fakultät Physik/DELTA, TU Dortmund, 44221 Dortmund, Germany

Starch has a wide range of application for example in food, cosmetics, and textile industries due to its unique properties of gelling, thickening, binding, and stabilizing. This polysaccharide is an essential component of food plants like wheat, rice, corn, and potato [1]. The heat-induced gelatinization of starch, in which the structure of the granules changes from crystalline to amorphous, is particularly important for the resulting quality of starch-containing foods [2]. Following this structural evolution is the key to understanding the interaction and aggregation of starch molecules.

Revealing the dynamic processes such as particle motion and relaxation during gelation can be done by performing X-ray photon correlation spectroscopy (XPCS) at P10 (DESY) and ID02/ID10 (ESRF). To gain insights into their nanoscale organization during heating and cooling in preparation for the XPCS measurements, small angle X-ray scattering (SAXS) experiments were conducted at beamline BL2 of the synchrotron radiation source DELTA [3]. Using a photon energy of 12 keV the experiments were performed under varying thermal conditions and salt concentrations. The combined use of SAXS and XPCS offers a comprehensive approach to studying starch systems, supporting advances in food science and biotechnology.

Four sample systems were prepared for this study: corn starch at 100 mg/ml in water, corn starch at 120 mg/ml in water, corn starch at 100 mg/ml in a 2M NaCl solution, and corn starch at 120 mg/ml in a 2M NaCl solution. The measurement protocol included rapid heating of the samples from room temperature to 60 °C at a rate of approximately 15 °C per minute. This was followed by slower heating from 60 °C to 80 °C at a rate of approximately 5 °C per minute. The samples were then held at 80 °C to observe gelatinization phase. This was followed by a slow cooling down to room temperature at a rate of 2 to 5 °C per minute.

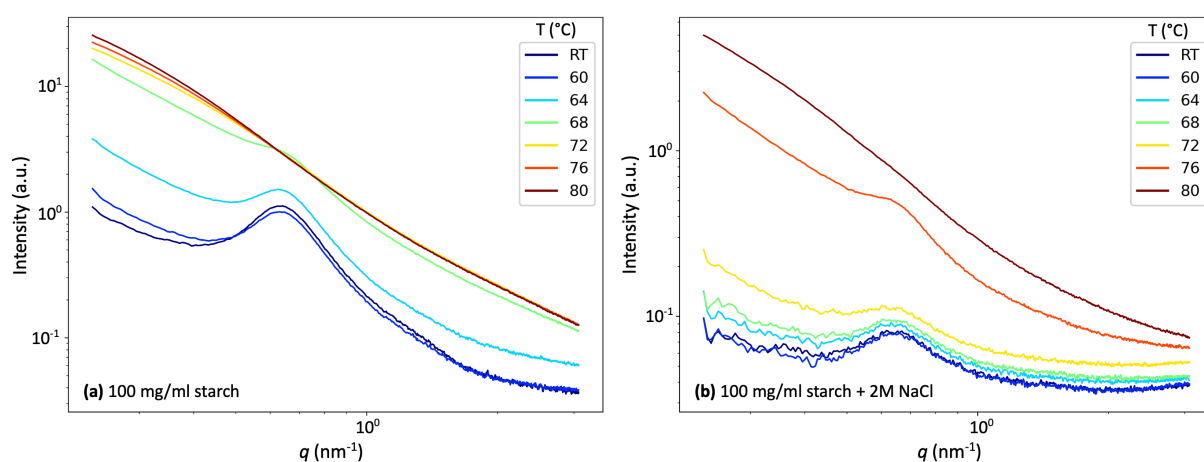


Figure 1: SAXS intensities of 100 mg/ml starch solutions during heating from room temperature, 25°C, (blue) to 80°C (red) (a) without addition of NaCl to the solution and (b) with 2 M NaCl within the solution.

In Figure 1 the SAXS intensities of 100 mg/ml starch (a) without NaCl and (b) with 2 M NaCl collected during heat treatment are shown. For all samples, sedimentation appeared to have occurred prior to heating, which was expected since starch is water insoluble. This results in a weak scattering signal before thermal treatment. For low temperatures the SAXS curves exhibit a strong scattering peak at approximately 0.7 nm^{-1} . This peak arises from the semicrystalline starch structure, where linear and branched macromolecules are organized radially in form of granules with an average lamellar thickness of approximately 9 nm [4][5]. These structures are lost during the gelation process, which is reflected in a change in the shape of the SAXS curves, but especially in the disappearance of the peak at higher temperatures. In this way, the temperature at which gelation sets in can be determined. Gelation in the presence of NaCl is observed to begin at higher temperatures compared to samples without NaCl, suggesting that salt may stabilize the starch structure or alter hydration effects.

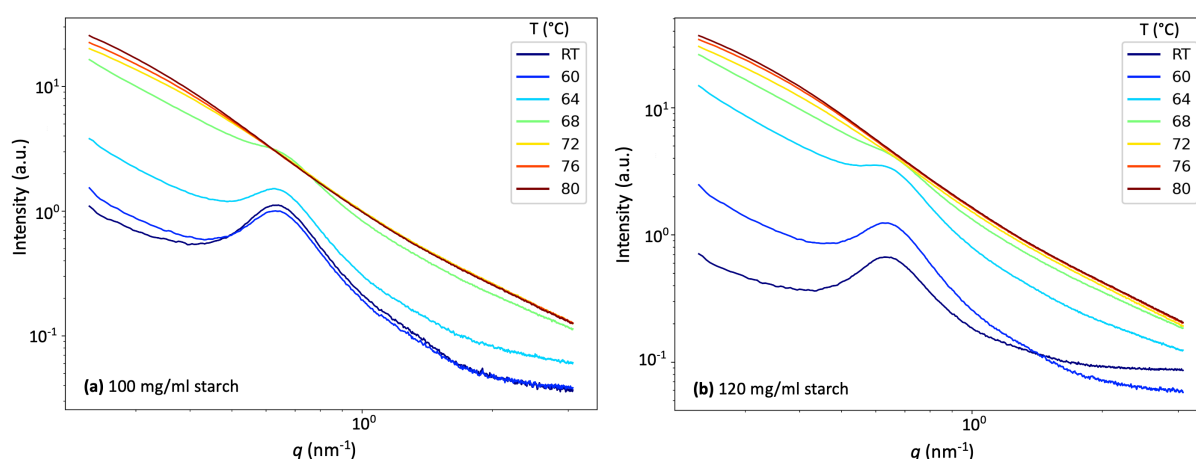


Figure 2: SAXS intensities of starch solutions containing (a) 100 mg/ml and (b) 120 mg/ml starch during heat treatment from room temperature, 25°C, (blue) to 80°C (red).

In Figure 2 the SAXS intensities of solution containing (a) 100 mg/ml and (b) 120 mg/ml are visualized. In terms of concentration effects, the differences between the 100 mg/ml and 120 mg/ml starch samples are relatively minor. However, the peak at e.g., 64 °C seems to be less pronounced in case of the 120 mg/ml sample, indicating that higher starch concentrations appear to promote earlier gelation, potentially due to increased polymer interactions.

In conclusion the initial temperatures for gelatinization processes of starch were determined and the influence of starch and salt concentration on this effect was investigated. These results will now be used to perform XPCS experiments at ESRF and DESY to gain insights into the dynamics of the system at the temperatures of interest.

Acknowledgments We thank the DELTA machine group for providing synchrotron radiation.

- [1] M. Tako et al. Food and Nutrition Sciences (2014), 5, 280-291
- [2] X. Wang et al. Food Hydrocolloids (2022), 129, 107658
- [3] M Dargasz et al. (2022) J. Phys.: Conf. Ser. 2380 012031
- [4] M. P. Cereda, in Starchy Crops Morphology, Extraction, Properties and Applications (2023), Vol. 1, Chapter 10
- [5] L. Zhang et al. International Journal of Biological Macromolecules (2020), 154, 521-527

Protein adsorption on solid supported lipid membranes

Jaqueline Savelkouls¹, Michelle Dargasz², Eric Schneider¹, Gordon Scholz¹, Christian Sternemann¹ and Michael Paulus¹

¹Fakultät Physik/DELTA, Technische Universität Dortmund, 44221 Dortmund, Germany

²Department of Physics / X-ray science, Universität Siegen, 57076 Siegen, Germany

*jaqueline.savelkouls@tu-dortmund.de

Proteins and lipids are the most significant biomolecules in living organisms, as they are responsible for all physiological functions. To comprehend the biochemical processes of an organism, it is essential to understand the structural conformation of proteins and lipids, the factors that influence alterations in structure, and the interactions between protein and lipid interfaces. Some diseases are caused by the adsorption of proteins to lipid layers, as exemplified by the acute respiratory distress syndrome [1]. To identify suitable therapies for this type of diseases, it is important to understand biochemical processes in living organisms. This knowledge can help to answer current questions in the pharmaceutical industry as well as in bio- and nanotechnology, i.e. the development of new therapeutic options, biosensors, protein chips, implants, contact lenses, nano-carrier systems, or immunoassays [2,3,4].

In this study, the adsorption of the protein human serum albumin (HSA) on substrate-bound lipid bilayers was investigated. HSA (CAS number: 70024-90-7, Sigma-Aldrich) is a surface-active plasma protein that is primarily found in the blood. It plays a key role in regulating pH and transporting a range of substances [5,6,7]. Lipids are amphiphilic macromolecules that can self-assemble into a variety of structures within an aqueous environment. They represent the primary components of cell membranes. Solid-supported lipid systems consisting of lipid bilayers are well established as biomimetic models to study various biological processes at membranes [8,9]. To create the model membrane, a lipid solution of the zwitterionic phospholipid 1,2dimyristoyl-sn-glycero-3-phosphocholine (DMPC) in an organic solvent (CAS number: 18194-24-6, Avanti) was applied onto a (10 x 18) mm² hydrophilized silicon wafer. Subsequently, a spin coater was used to generate a highly ordered and stable bilayer [10,11]. The prepared substrate-bound lipid layers on silicon substrate were mounted in a custom-made polytetrafluorethylene-sample cell and studied by X-ray reflectivity (XRR) to analyze their structure at the solid/liquid interface. The cell was installed at the six-circle diffractometer of beamline BL9 at DELTA. At beamline BL9, XRR measurements were utilized to investigate the interaction between the protein and the lipid membrane, as well as the structural changes in the bilayer in an aqueous environment at pH 7, *in situ*. The XRR data were collected using a PILATUS 100k area detector (Dectris, Baden-Dättwil, Switzerland) at an incident photon energy of 27 keV with a beam size at the sample position of (1.0 x 0.1) mm² (h x v) up to wave vector transfers of $q_z = 0.7 \text{ \AA}^{-1}$. All measurement were performed at room temperature.

The influence of protein concentration and pH on the structural changes of the lipid membrane during protein adsorption was examined. Figure 1 (left) presents the Fresnel-normalized reflectivities as a function of the HSA concentration, as well as the electron density profiles resulting from the fit function (black curve) with a schematic drawing of the lipid membrane (right). All data were analyzed using the LSFIT program [12]. The electron density profile exhibits a bilayer shape, which is characteristic of the lamellar phase of lipid membranes. Additionally, a notable asymmetry is observed, whereby the inner head group exhibits a consistently higher electron density because of van der Waals interactions with the silicon dioxide (SiO₂) layer present on top of the silicon substrate. The addition of HSA results in a significant structural change in the lipid membrane. We observe an increase in electron density in the tail groups and the outer head group, accompanied by a compression of the outer lipid layer, which reduces the overall thickness of the bilayer. In contrast, the electron density of the inner head group decreases. If the protein concentration increases further, the formed membrane structure remains the same, indicating that the adsorption sites are saturated, and no additional proteins can be absorbed at

the interface due to repulsive interactions between the adsorbed proteins and the proteins in the solution.

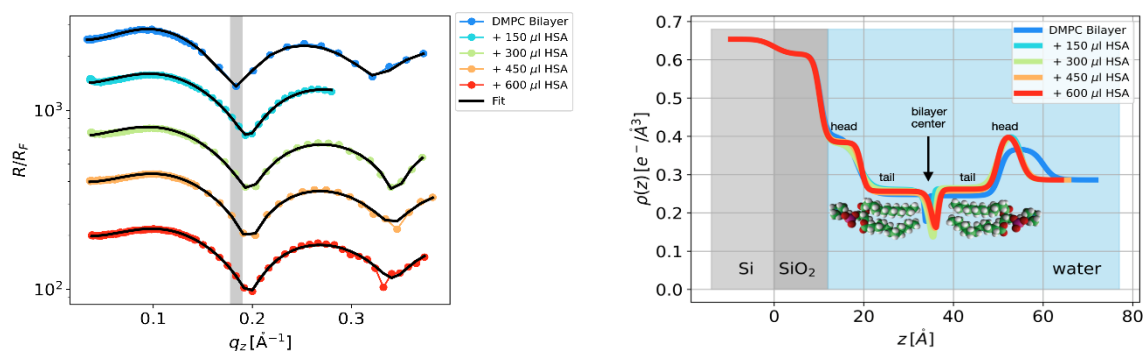


Figure 1: Left: Fresnel normalized XRR curves of concentration-dependent HSA measurements at DMPC bilayer. XRR curves shifted vertically for better visibility. Right: Corresponding electron density profiles including a schematic of the bilayer structure.

Furthermore, the impact of pH value was also investigated. From previous measurements in the absence of proteins, it was shown that a reduction in pH does not result in any substantial changes to the solid-supported DMPC bilayer structure [13]. Nevertheless, when HSA is present, a reduction in pH results in a notable effect on the membrane structure (see Figure 2). After addition of HSA, a significant structural change in the membrane occurs at a pH value of 7 due to the integration of HSA into the membrane. A further reduction in the pH value results again in a change in the membrane structure. It causes an increase in electron density, roughness, and layer thickness. The change in the membrane structure between pH 7 and lower pH values can be explained by the pH-dependent conformational transition of the protein from a heart-shaped to an unfolded structure in the bilayer.

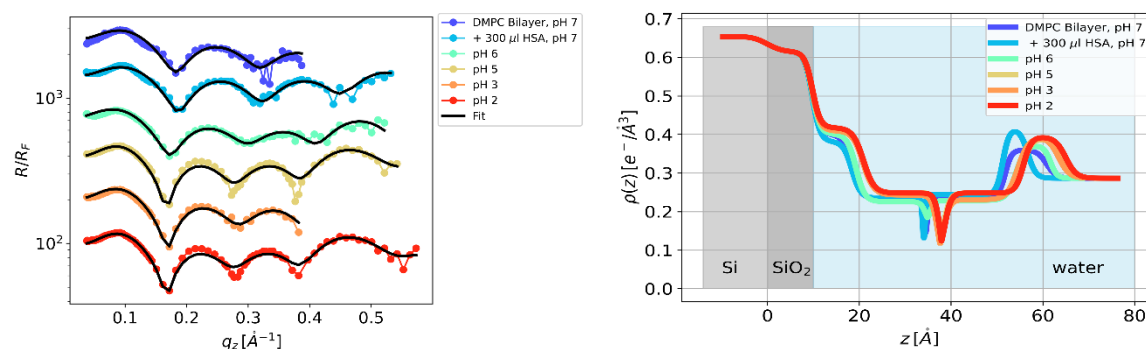


Figure 2: Left: Fresnel normalized XRR curves of pH-dependent HSA measurements at DMPC bilayer. XRR curves shifted vertically for better visibility. Right: Corresponding electron density profiles.

In addition to the analysis of the adsorption of the HSA protein, other proteins, including lysozyme and immunoglobulin G, were also examined. The analysis and subsequent interpretation of the comprehensive XRR data are ongoing.

References

- [1] M. P. Krafft, "Overcoming inactivation of the lung surfactant by serum proteins: a potential role for fluorocarbons?", in: *Soft Matter*, 2015, 11, 5982
- [2] Ulrike Mennicke et. al.; "Structure and interaction potentials in solid-supported lipid membranes studied by x-ray reflectivity at varied osmotic pressure", in: *The European Physical Journal E* 20.2 (2006), pp. 221–230.
- [3] M. Tanaka, E. Sackmann, "Supported membranes as biofunctional interfaces and smart biosensor platforms", in: *phys.stat.sol. (a)* 203, No.14, 2006, pp. 3452-3462
- [4] Q. Xhen, G. A. Thouas, "Metallic implant biomaterials", in: *Materials Science and Engineering R* 87, 2015, pp. 1–57
- [5] D. C. Carter, J. X. Ho, *Adv. Protein Chem.* 1994, 45, 153.
- [6] T. Peters Jr., *Adv. Protein Chem.* 1985, 37, 161.
- [7] S. Curry, P. Brick, N. P. Franks, *Biochim. Biophys. Acta* 1999, 1441,131
- [8] Ulrike Mennicke et. al.; "Structure and interaction potentials in solid-supported lipid membranes studied by x-ray reflectivity at varied osmotic pressure", in: *The European Physical Journal E* 20.2 (2006), pp. 221–230
- [9] Jeffrey J Gray, "The interaction of proteins with solid surfaces", in: *Current opinion in structural biology* 14.1 (2004), pp. 110–115;
- [10] U. Mennicke et al., "Preparation of Solid-Supported Lipid Bilayers by Spin-Coating", in: *Langmuir*, (2002), pp. 8172–8177.
- [11] Benedikt Nowak et al., "Solid-supported lipid multilayers under high hydrostatic pressure", in: *Langmuir* 32.11 (2016), pp. 2638–2643.
- [12] O.H. Seeck, LSFIT: Available on request from the author. Software for X-ray and neutron reflectivity calculation. 1999.
- [13] J. Savelkoul, S. Dogan, M. Moron, C. Sternemann, M. Paulus, "Apo ferritin adsorption on solid-supported DMPC bilayers", in: *DELTA Annual Report*, 2022, pp.61-62

Acknowledgments We thank the DELTA machine group for providing synchrotron radiation.

An X-ray diffraction study on the structure and phase behaviour of water-amine mixtures

Lena Friedrich¹, Michael Paulus¹, Aurélien Perera², Martina Požar³, Dirk Lützenkirchen-Hecht⁴, Nicola Thiering¹, Jaqueline Savelkoul¹, Christian Sternemann¹

¹Fakultät Physik/DELTA, TU Dortmund University, 44221 Dortmund, Germany

² Sorbonne Université, Laboratoire de Physique Théorique de la Matière Condensée (UMR CNRS 7600), F75252, Paris cedex 05, France ³ University of Split, Faculty of Science, 21000 Split, Croatia, ⁴ Fakultät für Mathematik und Naturwissenschaften, Bergische Universität Wuppertal, 42097 Wuppertal, Germany

Amines are associative liquids that can form supramolecular structures via hydrogen bonding [1]. This property is crucial for biochemical processes, as it influences the organization of molecular liquids and contributes to the stability of biomolecules [2]. Amines are widely used in industry, e.g. for gas removal [3]. Despite their structural similarity to monohydroxy alcohols [4], linear amines and mono-ols exhibit significant differences in their X-ray diffraction (XRD) patterns, notably in the extent of the pre-peak [5]. The addition of water to amines fundamentally changes the pre-peak behavior and thus the underlying structure within the liquid [1]. This study investigates the qualitative changes in supramolecular structure formation in amine-water mixtures as a result of water content and temperature.

The linear amines propylamine, butylamine, pentylamine, hexylamine, heptylamine, octylamine, nonylamine, and their mixtures with up to 33 vol% water (70 to 84 mol%, depending on the amine) were filled into borosilicate glass capillaries (\varnothing 1.5 mm). XRD experiments were carried out at BL8 of DELTA with an incident energy of 14 keV, corresponding to a wavelength of 0.8856 Å. The mixtures were placed in a temperature-controlled sample environment (Linkam Stage). The scattered intensity was detected by a MAR345 image plate detector. Diffractograms of twelve mixing ratios were taken for each amine. In addition, the temperature dependence was measured for each amine type for two mixing ratios (20 vol% and 33 vol%).

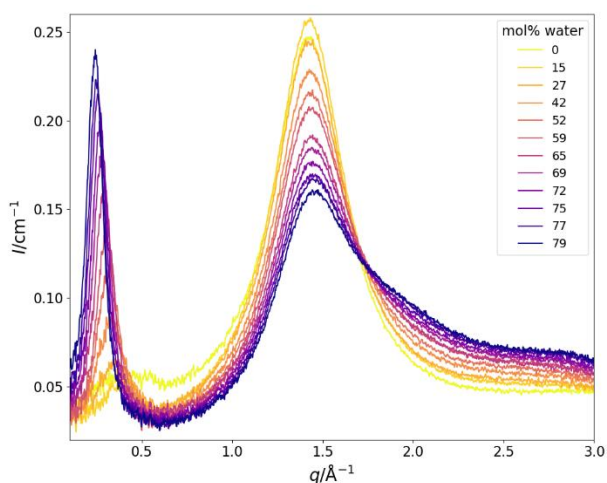


Figure 1: XRD patterns of hexylamine-water mixtures. The different shades of color represent the different ratios of water in mol%, going from pure hexylamine (yellow) to the mixture with 79 mol% of water.

The diffraction patterns of hexylamine-water mixtures are presented in Fig. 1. The most noticeable observation is the significant increase in pre-peak intensity with increasing water concentration, even surpassing the liquid's main peak. This is accompanied by a decrease in peak width and a shift of the pre-peak position to smaller wave vector transfer q . While pure hexylamine only exhibits a broad and weak pre-peak, adding only small amounts of water induces a remarkable change in shape and position. Since the occurrence of a pre-peak in associating liquids is closely linked to the formation of supramolecular clusters, this indicates that water acts as a structure former in amines. Molecular dynamics simulations suggest that the nitrogen atoms adhere to the surface of the water pockets, stabilized by the unique arrangement of water-nitrogen pairs at the amine-water interfaces.

During the investigation of the mixtures, deviating behavior also occurred in addition to the phenomena already described. Fig. 2 displays the diffraction patterns of nonylamine-water mixtures. While the mixtures up to 70 mol% water show the behavior exemplified in Fig. 1, very sharp peaks and a clear increase in intensity can be observed for the mixtures with more water. These Bragg peaks including higher-order maxima can be seen in the inset of the figure indicate the transition to another phase, which brings with it a certain degree of long-range order. In fact, the literature refers to the presence of a liquid-smectic phase in amine-water mixtures, comparable to that found in liquid crystals [6].

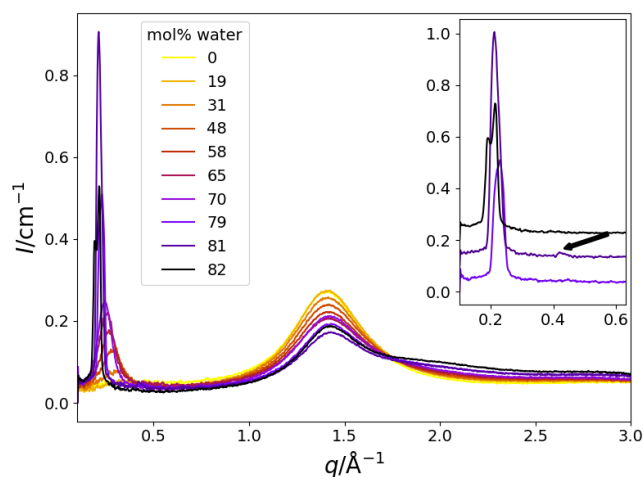


Figure 2: XRD patterns of nonylamine-water mixtures. The different shades of color represent the different ratios of water. The mixtures with high water content show Bragg-like peaks as well as maxima of higher order, as shown in the inset.

In addition to concentration-dependent measurements, temperature-dependent experiments were carried out on the mixtures, as exemplarily shown for 78 mol% octylamine-water mixture in Fig. 3 measured in a temperature range from 0°C to 100°C. Additionally to the already mentioned Bragg peaks, now appearing at low temperature, some different effects are noticeable at high temperatures. On the one hand, there is a change in trend in the pre-peak position, as can be seen in the inset. From around 70°C upwards, its position shifts back to larger q . On the other hand, an increase in intensity in the higher q range from about 2 \AA^{-1} can be found. Both are signs that a further phase, the two-liquid phase, is being passed through. In this phase, demixing effects occur, which reduce the effective mixing ratio.

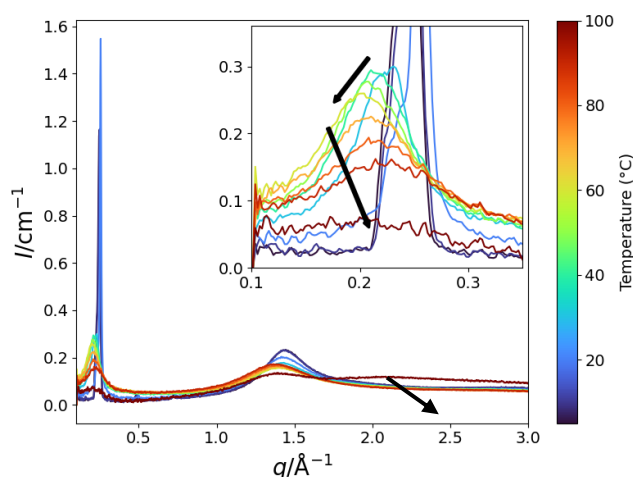


Figure 3: Temperature-dependent XRD patterns of the 78 mol% octylamine-water mixture. At 100°C an increased intensity in the high q range can be observed. The inset shows the pre-peak behavior in detail, with the arrows underlining a trend change in the peak

References

- [1] L. Almásy, A. Kuklin, M. Požar, A. Baptista and A. Perera. Microscopic origin of the scattering pre-peak in aqueous propylamine mixtures: X-ray and neutron experiments versus simulations. *Physical Chemistry Chemical Physics*, 21:9317–9325, 2019.
- [2] A. Babusyte, M. Kotthoff, J. Fiedler and D. Krautwurst. Biogenic amines activate blood leukocytes via trace amine-associated receptors taar1 and taar2. *Journal of Leukocyte Biology*, 93:387–394, 2013.
- [3] S. Faramawy, T. Zaki and A. Sakr. Natural gas origin, composition, and processing: A review. *Journal of Natural Gas Science and Engineering*, 34:34–54, 2016.
- [4] M. Požar, J. Bolle, C. Sternemann and A. Perera. On the x-ray scattering pre-peak of linear mono-ols and the related microstructure from computer simulations. *The Journal of Physical Chemistry B*, 124:8358–8371, 2020.
- [5] M. Požar, L. Friedrich, T. Millet, M. Paulus, C. Sternemann and A. Perera. Microscopic Structure of Neat Linear Alkylamine Liquids: An X-Ray Scattering and Computer Simulation Study. *The Journal of Physical Chemistry B*, 128:10925–10936, 2024.
- [6] J. Glinski, G. Chavepey, J.K. Platten, C. De Saedeleer. Phase diagrams and interfacial properties of water-hexylamine, water-heptylamine, and water octylamine systems. *Journal of Colloid and Interface Science*, 162(1):129–134, 1994.

Acknowledgments

The authors gratefully acknowledge the support of the Bundesministerium für Bildung und Forschung (BMBF) for funding via DAAD in the scope of the French-German collaboration PROCOPE 2024-2025 (Project-IDs 57704875 and 50951YA).

Liquid-solid phase transformations in macromolecular liquids under cryogenic temperatures

Michelle Dargasz¹, Jaqueline Savelkouls², Nimmi Das Anthuparambil¹, Michael Paulus², Christian Gutt¹

¹Department of Physics / X-ray science, Universität Siegen, 57076 Siegen, Germany

²Fakultät Physik/DELTA, TU Dortmund, 44221 Dortmund, Germany

Freezing is a widely employed method to extend shelf life during storage in both the food and pharmaceutical industries. In the pharmaceutical sector, frozen storage enhances flexibility in filling and processing procedures [1]. In the food industry, freezing helps preserve nutritional content, texture, taste, and color [2], as lowering the temperature slows down chemical reactions and microbial growth [3]. Macromolecules play a critical role in products from both fields. Cooling macromolecules in solution can lead to phenomena such as buffer crystallization or phase separation, which may disrupt the native structure and functionality of these macromolecules. Consequently, understanding the effects of freezing on macromolecular structure is of significant interest.

To address this, two distinct sample systems were studied. The first sample system consisted of concentrated ferritin solutions. Ferritin, a hollow-spherical protein with an outer diameter of 12 nm, can store up to 4500 iron atoms in its cavity [4], serving as an iron storage protein in the human body. Ferritin in a saline solution containing 9 g/L NaCl was bought from Sigma Aldrich (F4503). Through centrifugation the ferritin solution was concentrated to final protein concentrations of 70 mg/ml, 190 mg/ml, and 270 mg/ml. The second sample system used was egg yolk plasma, the liquid fraction of egg yolk, which consists of approximately 85% low-density lipoproteins (LDLs) and 15% glycoproteins [5]. LDLs are spherical particles with a diameter of approximately 22 nm, composed of a monolayer of apoproteins surrounding triglycerides and cholesterol esters [6]. To extract egg yolk plasma, fresh eggs were purchased from a supermarket, and the yolks were centrifuged at 10 000g for 48 hours. This process allowed the large granules to settle, enabling the separation of the plasma. The plasma was analyzed in its pure form and in a 50:50 mixture with glycerol, which acted as a cryoprotectant.

Temperature dependent structural changes in these sample systems were investigated using small-angle X-ray scattering (SAXS). SAXS measurements were conducted at beamline BL2 of the DELTA with a photon energy of 12 keV. The scattering signal of a SAXS experiment is determined by two components, the protein's form factor $P(q)$ and the effective structure factor $S_{eff}(q)$: $I(q) \sim r_0^2 N P(q) S_{eff}(q)$ [7], where q denotes the scattering vector $q = 4 \pi / \lambda \cdot \sin(\theta)$. $P(q)$ gives information about the particle's expansion in solution and $S_{eff}(q)$ about interactions between the solution's components. With increasing particle concentration, the interactions within the system become stronger and the $S(q)$ gets visible in form of a correlation peak at $q = q_{max}$, where the correlation length $\xi = 2\pi/q$ reflects the typical particle distances within the solution.

Fig. 1 (a) shows the SAXS intensities for the 70, 190 and 270 mg/ml ferritin solution at 25°C (red) and -22°C (blue). Comparing the intensities collected at the two different temperatures, a development of a pronounced correlation peak is observed at -22°C. Both the amplitude of the correlation peak and the q -value for q_{max} increase. Since this reflects an increase of repulsive interactions as well as a reduction of the correlation length within the system, it becomes apparent that areas of very high protein concentration develop during cooling down. This phenomenon is known as freeze concentration, which was already observed in ferritin and lysozyme solutions [8][9]. Decreasing the temperature causes a part of the water molecules in the solution to form a crystalline ice phase. The proteins and the remaining water molecules are excluded from this ice phase, resulting in very highly concentrated amorphous phases. As the concentration of the initial ferritin solutions increases, the correlation peak is

even more pronounced and shifted to higher q -values, which indicates even more concentrated ferritin regions within the partly frozen solution.

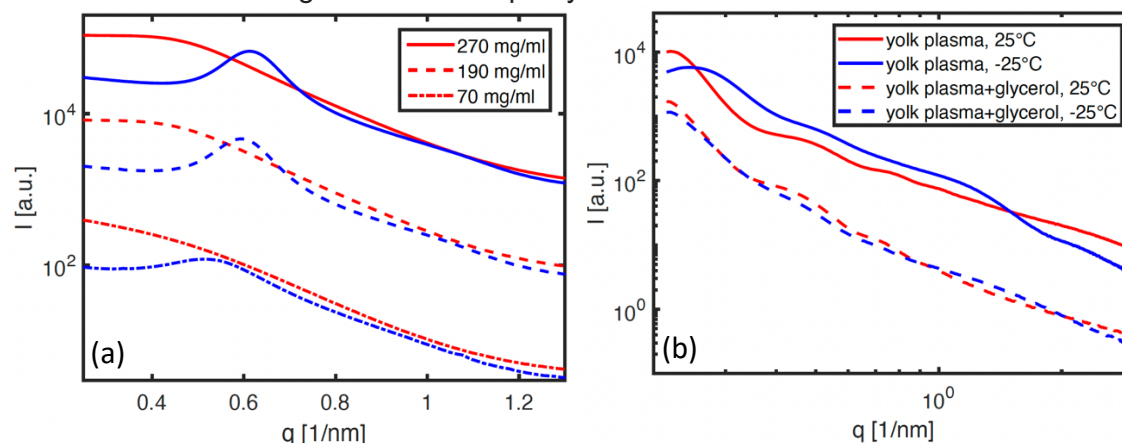


Figure 1: Scattering intensity of (a) ferritin solutions with protein concentrations of 70 (dashed dotted lines), 190 (dashed lines) and 270 mg/ml (solid lines) at room temperature (25 °C) (red) and at -20°C (blue) and (b) egg yolk plasma at room temperature (red) and -25°C (blue) for pure plasma (solid lines) and a 50:50 mix of plasma with glycerol (dashed lines). The SAXS intensities were shifted on the y-axis in order to display the comparison of the curves more clearly.

The shift in the correlation peak is also visible when egg yolk plasma is cooled, as shown in **Fig. 1** (b), whereas when glycerol is used, which prevents the formation of an ice phase, no shift can be seen. In this special case a second effect is observed. This is illustrated more clearly in **Fig. 2**, which displays the SAXS intensities during cooling down with smaller temperature steps. A peak develops at 1.6 nm^{-1} when temperatures fall below -5°C , as indicated by the black arrow. Similar effects were observed in solutions of human LDL where a phase transition is detected at temperatures between $15 - 30^\circ\text{C}$ [10]. In SAXS studies the evolution of a peak at 0.16 \AA^{-1} was observed [11], which was attributed to a layering of the normally isotopically organized cholesterol esters inside the LDL particle [12]. This results in a three-layer internal lamellar structure with 3.6 nm distance between the layers [6]. Since the observed peak in this study of yolk LDL arises at similar q -values, it is reasonable to assume that a layering of cholesterol esters within the LDL particles also occurs due to a cool down of the yolk plasma. In this case, however, the temperature for the phase transition is at significantly lower temperatures between -5°C and -10°C . After reheating the system, the peak disappears which indicates the reversibility of the transition.

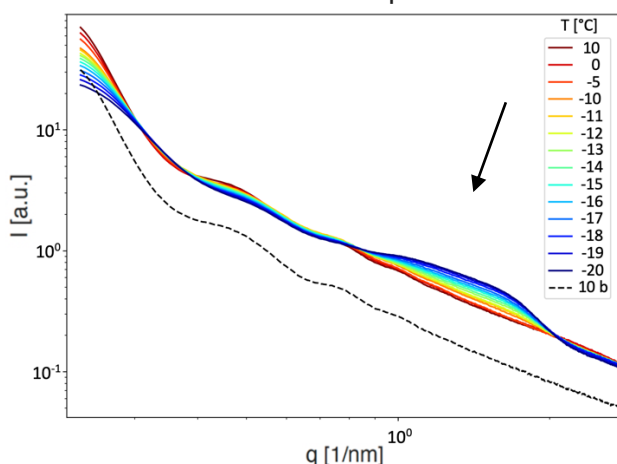


Figure 2: SAXS intensities of egg yolk plasma without glycerol during cooling from 10°C (red) to -20°C (blue). The dashed black line represents the SAXS intensity after heating up to 10°C .

Acknowledgments We thank the DELTA machine group for providing synchrotron radiation.

- [1] N. Rathore et al. *Biotechnol. Prog.* 2008, 24, 504–514 [2] A. Soyer et al. *Food Chem.* 2010, 120, 1025–1030. [3] B. Minatovicz et al. *Journal of Drug Delivery Science and Technology.* 2020, 58, 101703 [4] P. M. Harrison, P. Arosio, *Biochimica et Biophysica Acta (BBA) – Bioenergetics.* 1996, 1275, 3, 161-203 [5] A. Laca et al. *LWT - Food Science and Technology.* 2015, 22, 7-10 [6] R. Prassl *Journal of Lipid Research.* 2011, 52, 2, 187 - 188 [7] J. Als-Nielsen; D. McMorrow. *Elements of Modern X-Ray Physics.* 9781119998365. John Wiley und Sons, 2011 [8] J. E. Curtis et al. *The Journal of Physical Chemistry B* (2012), 116, 32, 9653–9667 [9] S. Boutet, I. K. Robinson *PHYSICAL REVIEW* (2007) E 75, 021913 [10] E. V. Orlova et al. *Proc. Natl. Acad. Sci. USA.* 1999, 96, 8420–8425 [11] D. Jakubauskas et al. *Nanotechnology, Biology, and Medicine* (2021), 31, 102318 [12] Y. Liu et al. *J Lipid Res.* (2011), 52, 2, 256–262

Phase transition in $\text{Eu}_2\text{LiC}_3\text{H}$

T. Kleinöder and U. Ruschewitz*

Department of Chemistry and Biochemistry, University of Cologne, 50939 Cologne, Germany

*email: uwe.ruschewitz@uni-koeln.de

By reaction of LiH with carbon black in an Eu/Li flux, single crystals of $\text{Eu}_2\text{LiC}_3\text{H}$ were obtained. The compound crystallizes in the $\text{Ca}_2\text{LiC}_3\text{H}$ type structure^[1] in the tetragonal space group $P4/m\bar{b}m$ (no. 127) with $Z = 2$. It consists of $\text{C}=\text{C}=\text{C}^{4-}$ and isolated H^- anions (Figure 1, left). A close inspection of the low temperature single crystal structure data reveals that a phase transition to an orthorhombic modification occurs ($Pbam$ (no. 55), $Z = 4$), which has not been reported for the calcium congener. This phase transition can be described by a group-subgroup formalism, as developed by *H. Bärnighausen* (Figure 1, right).^[2,3]

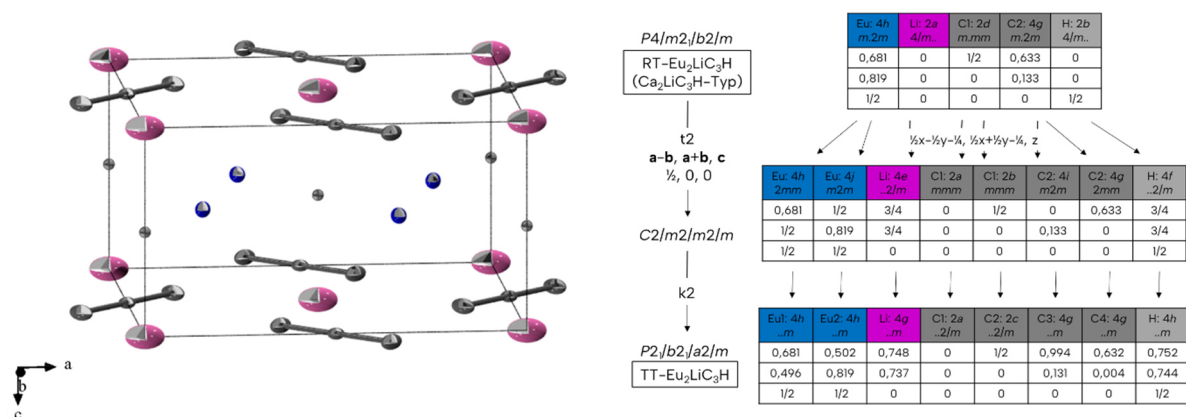


Figure 1. Left: crystal structure of $\text{Eu}_2\text{LiC}_3\text{H}$ at RT (blue: Eu, purple: Li, black: C, grey: H); right: group-subgroup scheme of the phase transition of $\text{Eu}_2\text{LiC}_3\text{H}$ between RT and 240 K.

To analyse this phase transition in more detail with a specific focus on the Li mobility in dependence of the temperature, synchrotron powder diffraction data was recorded at beamline BL9 of the DELTA synchrotron facility. They reveal an almost “textbook-like” behaviour. The splitting of some reflections (Figure 2, left) as well as the occurrence of additional superstructure reflections is clearly visible. The resulting lattice parameters of the Rietveld refinements are plotted in Figure 2 (right). They show that the phase transition starts at approx. 240 K upon cooling. While the c parameter shows the expected decrease upon cooling, the tetragonal a parameter is split into a_{ortho} and b_{ortho} . Note: above the phase transition temperature, a_{tet} is multiplied by $\sqrt{2}$ in Figure 2 (right) for a clearer presentation. A close inspection of the structural changes reveals that the Li^+ cations show the highest mobility upon heating, which also affects the orientation of the C_3^{4-} anions. Currently, we are investigating the structural behaviour of $\text{Eu}_2\text{LiC}_3\text{H}$ at temperatures above RT as well as some of its properties like magnetism or thermal stability.

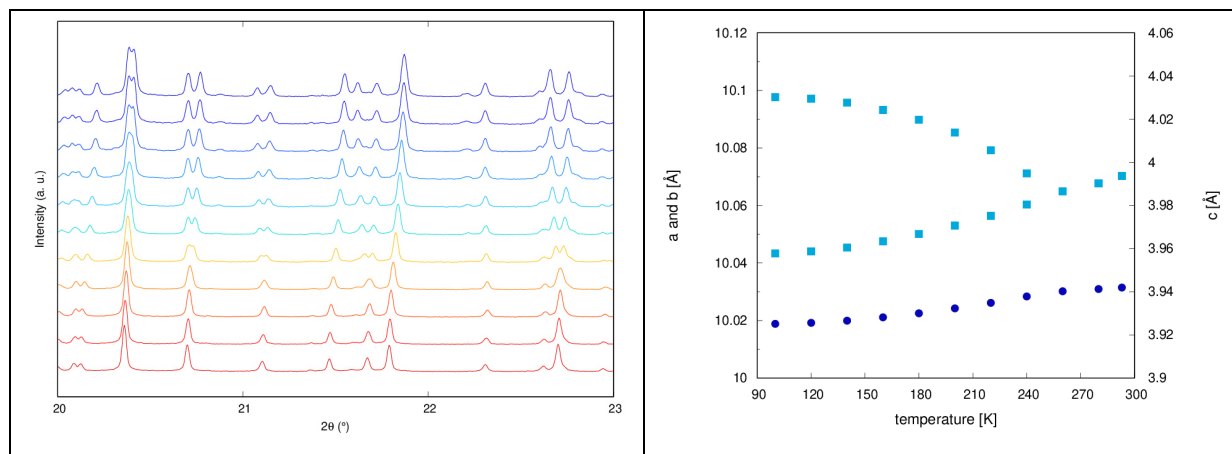


Figure 2. Left: sections of synchrotron powder diffraction patterns of $\text{Eu}_2\text{LiC}_3\text{H}$ upon cooling; right: lattice parameters of $\text{Eu}_2\text{LiC}_3\text{H}$ upon cooling as extracted by Rietveld fits. For details, see text.

- [1] D. A. Lang, J. V. Zaikina, D. D. Lovingood, T. E. Gedris, S. E. Lattner, *J. Am. Chem. Soc.* **2010**, *132*, 17523-17530.
- [2] H. Bärnighausen, *Commun. Math. Chem.* **1980**, *9*, 139-175.
- [3] T. Block, S. Seidel, R. Pöttgen, *Z. Kristallogr. – Cryst. Mater.* **2022**, *237*, 215-218.

X-ray diffraction analysis via synchrotron radiation of various natural rocks coated with TiN

Wolfgang Tillmann¹, Dominic Graf^{1,*}, Nelson Filipe Lopes Dias¹, Bernd Breidenstein²,
Berend Denkena², Benjamin Bergmann², Hilke Petersen²

¹Institute of Materials Engineering, TU Dortmund University, Leonhard-Euler-Str. 2, D-44227 Dortmund

²Institute of Production Engineering and Machine Tools (IFW), Leibniz University Hannover, An der
Universität 2, 30823 Garbsen, Germany

*corresponding author: dominic.graf@tu-dortmund.de

Cemented carbide is a commonly used cutting material, but its production is expensive and energy-intensive [1]. Particularly the elements cobalt and tungsten are scarce and often originate from ethically problematic sources [2-4]. Intensive research is therefore being carried out into alternatives, with natural rocks showing considerable potential [5-6]. These offer ecological and economic advantages, as many energy-intensive production process steps have already been performed by nature. Their suitability depends on their mineral composition, microstructure and texture influenced by rock formation [7]. The natural rocks investigated were flint (sedimentary), lamellar obsidian (magmatic), two quartzites (metamorphic) and pure quartz. All investigated rocks have a significantly high SiO₂ content above 90 %. Previous investigations have proven that rocks can be used as cutting material under suitable conditions [5, 6, 8-11]. Parameters such as tensile strength, hardness and texture are decisive for their machinability. Grinding tests with diamond-bonded grinding wheels showed that smaller grain sizes and higher grain concentrations improve the cutting-edge quality. Natural rocks are especially suitable for machining soft materials such as polyetheretherketone (PEEK) and aluminum alloys [8]. Lubrication and high cutting speeds (up to 1000 m/min) can reduce wear mechanisms such as material adhesion and abrasion. Preliminary results show that TiN thin films applied by PVD increase surface hardness and improve performance [10]. To obtain a comprehensive understanding on the crystallographic structure of TiN on the natural rocks, high resolution 2D XRD measurements were performed at BL9.

Figures 1 and 2 illustrate the two-dimensional diffraction data from synchrotron experiments. The diffraction pattern of uncoated lamellar obsidian shows only a diffuse scattering ring, characteristic of glassy SiO₂. The synchrotron data of all crystalline natural rocks show low SiO₂ reflections (spacegroup: P3₂21); in particular, the (100), (101) and (112) reflections are detectable. These reflections appear as distinct intensity spots for the highly crystalline quartz. Similarly, uncoated alta quartzite and silver quartzite show pronounced intensity spots along

the characteristic Laue rings indicating the presence of large crystallites. In addition, the quartzite diffraction data contain reflections of layered aluminosilicate compounds. In the case of the uncoated flint sample, the Laue ring pattern is consistent with a polycrystalline material, with SiO_2 being the main phase. For all coated natural rocks, the two-dimensional diffraction patterns contain characteristic TiN reflections with an fcc structure and reflections of the natural rock substrates. The substrate reflection positions vary significantly between uncoated and TiN-coated quartz, a typical phenomenon when measuring large crystallites with different orientations. The TiN reflections, especially the (111), (200), (220) and (311) planes, exhibit a distinct intensity pattern. Similar intensity distributions can be observed for all TiN-coated natural rocks. The (111) and (200) reflexes show higher intensity at azimuth angles of 45° , 90° , and 135° , while the (220) reflex is more intense between 55° and 125° [12]. The distinctive intensity pattern indicates a strong texturing of the TiN thin film [13].

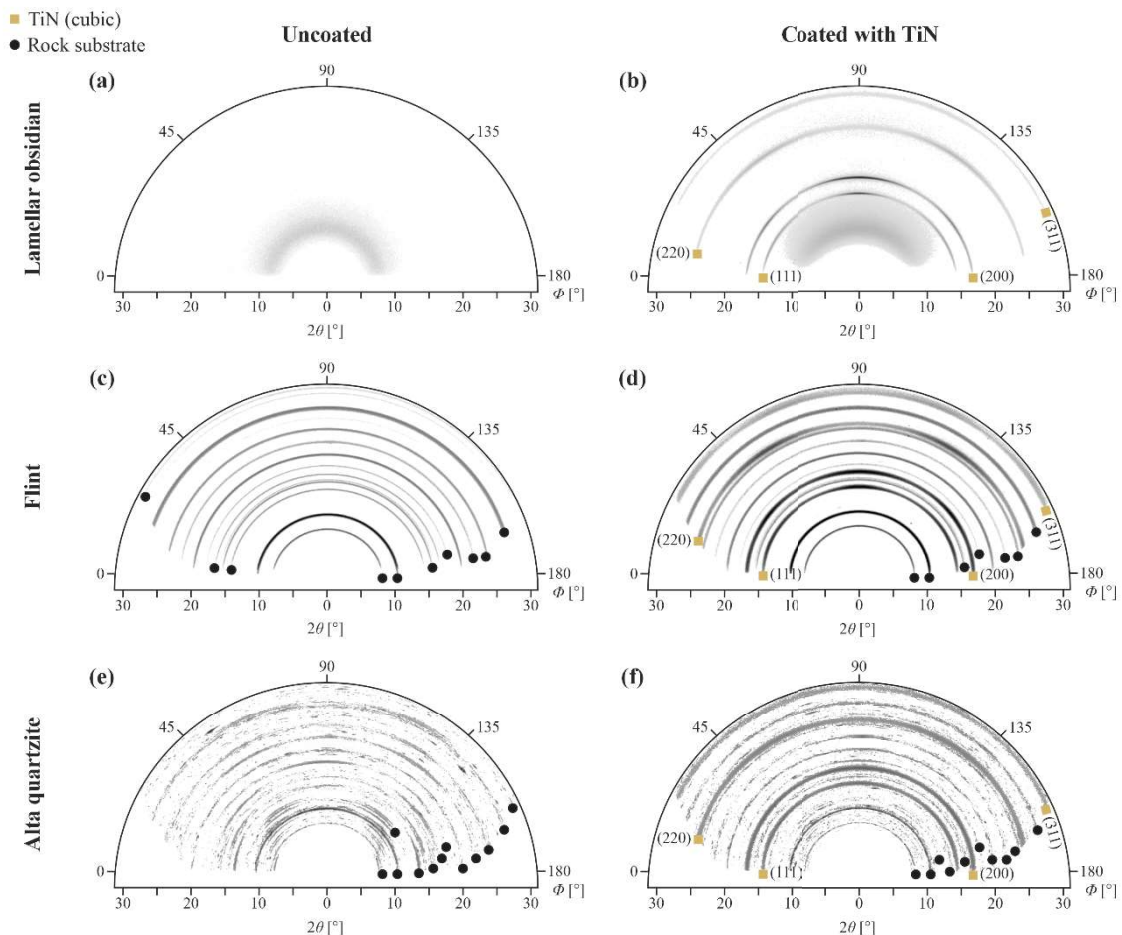


Figure 1. Two-dimensional diffraction pattern of different samples obtained by synchrotron experiments: (a) uncoated lamellar obsidian, (b) TiN-coated lamellar obsidian, (c) uncoated flint, (d) TiN-coated flint, (e) uncoated Alta quartzite, (f) TiN-coated Alta quartzite. (Reproduced from [12] under the terms of the CC BY 4.0)

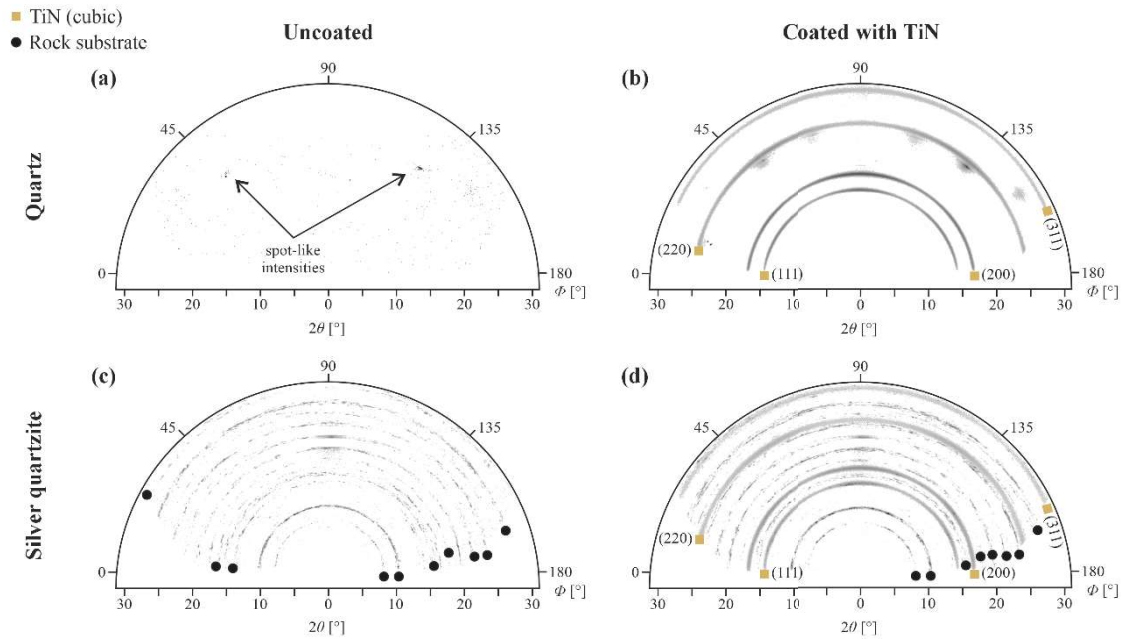


Figure 2: Two-dimensional diffraction pattern of different samples obtained by synchrotron experiments: (a) uncoated quartz, (b) TiN-coated quartz, (c) uncoated silver quartzite, (d) TiN-coated silver quartzite. (Reproduced from [12] under the terms of the CC BY 4.0)

Analyzing the microstructure of TiN thin films on natural rocks is essential to gain insights into the crystallographic orientation and texturing of the thin films on the different substrates. Understanding these correlations is crucial as the interaction between substrate properties and film growth has a major influence on the formation of the structural features of the deposited TiN thin films. Particularly, the correlation between the mineralogical characteristics of the substrate and the resulting thin film properties provides valuable information about the mechanisms that allow to improve the cutting performance of TiN-coated natural rocks for machining applications.

Acknowledgements: The authors gratefully acknowledge the financial support by the Deutsche Forschungsgemeinschaft (DFG, German Research Foundation) in the project “*Development of PVD-coated tools made of rocks*” (funding numbers BR 2967/35-1 and TI 343/217-1). In addition, the authors thank the DELTA for providing synchrotron radiation and for the technical support at beamline BL9 during the X-ray diffraction.

Publication of the results: The study “*Physical-Vapor-Deposition-Coated Natural Rocks as Sustainable Cutting Material: First Insights into the Effect of Substrate Integrity on Properties of TiN Thin Film*” includes the previously presented results and was published in the journal *Coatings* (2024, 14(10), 1333).

References

- [1] Bobzin, R.: High-performance coatings for cutting tools. *CIRP J. Manuf. Sci. Technol.* 2017, 18, S. 1–9, doi: 10.1016/j.cirpj.2016.11.004
- [2] Denkena, B.; Dittrich, M. A.; Liu, Y.; Theuer, M.: Automatic Regeneration of Cemented Carbide Tools for a Resource Efficient Tool Production. *Procedia Manuf.* 2018, 21, S. 259–265, doi: 10.1016/j.promfg.2018.02.119
- [3] Young, S. B.: Responsible sourcing of metals: certification approaches for conflict minerals and conflict-free metals: *Int. J. Life Cycle Assess.* 2018 23, S. 1429–1447, doi: 10.1007/s11367-015-0932-5
- [4] Rizzo, A.; Goel, S.; Grilli, M. L.; Iglesias, R.; Jaworska, L.; Lapkovskis, V.; Novak, P.; Postolnyi, B. O.; Valerini, D.: The critical raw materials in cutting tools for machining applications: A review. *Materials (Basel)* 2020 13, doi: 10.3390/ma13061377
- [5] Wolters, P.; Picker, T.; Breidenstein, B.; Krödel, A.; Denkena, B.: Application of natural rocks in cutting aluminum. *Production at the Leading Edge of Technology* 2021 doi: https://doi.org/10.1007/978-3-030-78424-9_26
- [6] Denkena, B.; Breidenstein, B.; Krödel, A.; Bergmann, B.; Picker, T.; Wolters, P.: Suitability of natural rocks as materials for cutting tools- *SN Appl. Sci.* 2022 4, doi: 10.1007/s42452-021-04883-z
- [7] Wittke, W.: *Rock mechanics – theory and applications with case histories.* Springer-Verlag, Berlin Heidelberg, 1990
- [8] Breidenstein, B., Denkena, B., Bergmann, B., Wolters, P., Picker, T.: Turning Copper and Aluminum Alloys with Natural Rocks as Cutting Tools. *Materials* 2022 15, doi: 10.3390/ma15062187
- [9] Breidenstein, B., Denkena, B., Bergmann, B., Picker, T., Wolters, P.: Tool wear when using natural rocks as cutting material for the turning of aluminum alloys and plastics. *Prod. Eng.* 2023 17, S. 425–435, doi: 10.1007/s11740-022-01159-2
- [10] Breidenstein, B., Denkena, B., Wolters, P., Keitel, M., Tillmann, W., Stangier, D., Lopes Dias, N.F.: A novel development of sustainable cutting inserts based on PVD-coated natural rocks. *Mater. Today Sustain.*, 2023, 24, doi: 10.1016/j.mtsust.2023.100507
- [11] Denkena, B., Breidenstein, B., Bergmann, B., Wolters, P.: Investigation of the material separation behaviour of rocks using scratch tests for the design of tool grinding processes. *SN Appl. Sci.* 2022 4, doi: 10.1007/s42452-022-05038-4
- [12] Petersen H., Graf D., Lopes Dias, N. F., Tillmann, W., Wolters, P., Bergmann, B., Breidenstein, B.: PVD-Coated Natural Rocks as Sustainable Cutting Material: First Insights into the Effect of Substrate Integrity in TiN Thin Film Properties. *Coatings*, 2024, 14, doi: 10.3390/coatings14101333
- [13] Tillmann, W., Hagen, L., Stangier, D., Lopes Dias, N.F., Görtz, J., Kensy, M. D.: Lapping and polishing of additively manufactured 316L substrates and their effects on the microstructural evolution and adhesion of PVD CrAlN coatings. *Surf. Coat. Tech.*, 2021, 428, doi: 10.1016/j.surfcoat.2021.127905

Investigating the long-range structural evolution of multivariate ZIF-76 derivatives during exothermic melting and glass formation properties

Guoqiang Li, Sebastian Henke*

Anorganische Materialchemie – TU Dortmund, Otto-Hahn-Str. 6, 44227 Dortmund

1. Scientific context

Melting, the transition from a crystalline solid to a liquid, is a critical process in materials science with widespread applications, particularly for glass manufacturing^[1]. Thermodynamically it is described as a first-order phase transition occurring at the melting temperature (T_m), where the Gibbs free energies of solid and liquid phases are equal. While the well-known Lindemann criterion^[2] attributes melting to atomic vibrations exceeding a critical amplitude, it does not account for mechanical instability, a significant factor in porous materials such as zeolites and metal-organic frameworks (MOFs).

Zeolitic imidazolate frameworks (ZIFs) are a subclass of MOFs built from divalent metal ions (e.g., Zn^{2+} , Co^{2+}) and imidazolate-based linkers^[3]. Their porous nature, while advantageous for applications, reduces mechanical stability and influences melting behaviour^[4]. Most meltable ZIFs collapse irreversibly during melting due to internal stress relaxation and framework destabilisation^[5]. This collapse introduces additional entropy and reduces the melting temperature below predictions based solely on thermal vibrations^[6].

ZIF-76 ($Zn(im)(Clbim)$, im^- = imidazolate, $Clbim^-$ = 5-chlorobenzimidazolate; Figure 1), a high-porosity framework, does not melt in its pure form due to strong linker interactions^[7]. To overcome this, we synthesised multivariate ZIF-76 derivatives ($Zn(im)_x(Clbim)_y(WBL)_z$; $x + y + z = 2$) by partially replacing the $Clbim^-$ linker with a weaker binding linker (WBL). This modification enabled exothermic melting of the porous framework, followed by glass formation upon cooling. The exothermic behaviour likely results from substantial internal stress release during melting. In the present study, we investigate the structural evolution and thermal properties of these ZIF-76 derivatives using variable-temperature powder X-ray diffraction (VT-PXRD) at beamline 9 of DELTA and differential scanning calorimetry (DSC), shedding light on their unique melting and glass formation mechanisms.

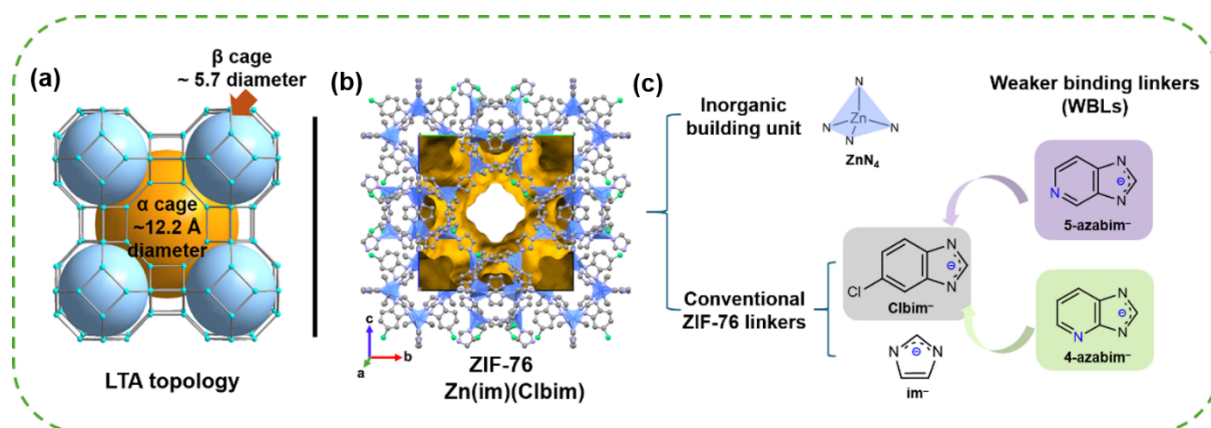


Fig. 1. The LTA (Linde Type A) topology of the highly porous ZIF-76 (a) and its crystal structure (b). Unit cells are shown as thin black lines. The void space (51.8% of the crystal volume) is calculated using Mercury software with a probe radius of 1.6 Å and a grid spacing of 0.2 Å and is shown in pale yellow. The inorganic and organic building units of ZIF-76 and weaker binding linkers are shown on the right (c).

2. Experiment setup and aim

The aim of the current proposal is to investigate the long-range structural evolution of meltable multivariate ZIF-76 derivatives when heated across their melting point, with a particular focus on the liquid phases formed during exothermic melting. We collected VT-PXRD data for 16 different ZIF-76- $im_xClbim_yWDL_z$ with varying fractions of $Clbim^-$ exchanged by the WBLs 5-azabenzimidazolate

(5-azabim⁻), 4-azabenzimidazolate (4-azabim⁻) or purine (pur⁻) in the temperature range from 25 °C up to their melting temperature (300 °C to 460 °C) in steps of 10 to 25 °C (as appropriate) using the Anton Parr heating stage with a graphite dome at beamline 9 of DELTA. After crossing the melting temperature, the sample was returned to ambient temperature for another data collection to check whether the sample maintained its amorphous (glassy) state after cooling the melt.

3. Results

Before this beamtime, we conducted thermogravimetric analysis (TGA) and DSC measurements for ZIF-76 and its derivatives. Here, we present ZIF-76 (ZIF-76-im_{1.13}Clbim_{0.87}) and two representative derivatives (ZIF-76-im_{1.07}Clbim_{0.59}4-azabim_{0.35} and ZIF-76-im_{1.08}Clbim_{0.59}5-azabim_{0.33}) to highlight the key results. For ZIF-76, Bragg peaks remain visible at 450 °C, although they become weaker, indicating incomplete amorphisation via partial structural collapse upon thermal treatment. This observation aligns with the DSC data, where the first upscan shows a weak exothermic signal prior to the decomposition temperature. For the two-representative multivariate ZIF-76 derivatives, the VT-PXRD patterns at 25 °C are consistent with the simulated pattern of the ZIF-76 crystal structure, confirming their structural purity. Upon heating to the exothermic region observed in DSC, the Bragg peaks disappear, indicating that the exothermic event is associated with amorphisation, likely due to framework collapse. At the offset temperature of the exothermic feature in the DSC, both ZIF-76 derivatives exhibit complete amorphisation, consistent with the melting of the materials. Interestingly, the Bragg peak intensities of ZIF-76-im_{1.07}Clbim_{0.59}4-azabim_{0.35} decrease and disappear at ~400 °C, a temperature notably higher than that observed for ZIF-76-im_{1.08}Clbim_{0.59}5-azabim_{0.33}. This discrepancy can be attributed to the higher Zn–N binding energy of 4-azabim⁻ compared to 5-azabim⁻, as determined by supporting density functional theory (DFT) calculations. The stronger Zn–N interaction in 4-azabim⁻ provides enhanced thermal stability, delaying the collapse of the crystalline structure.

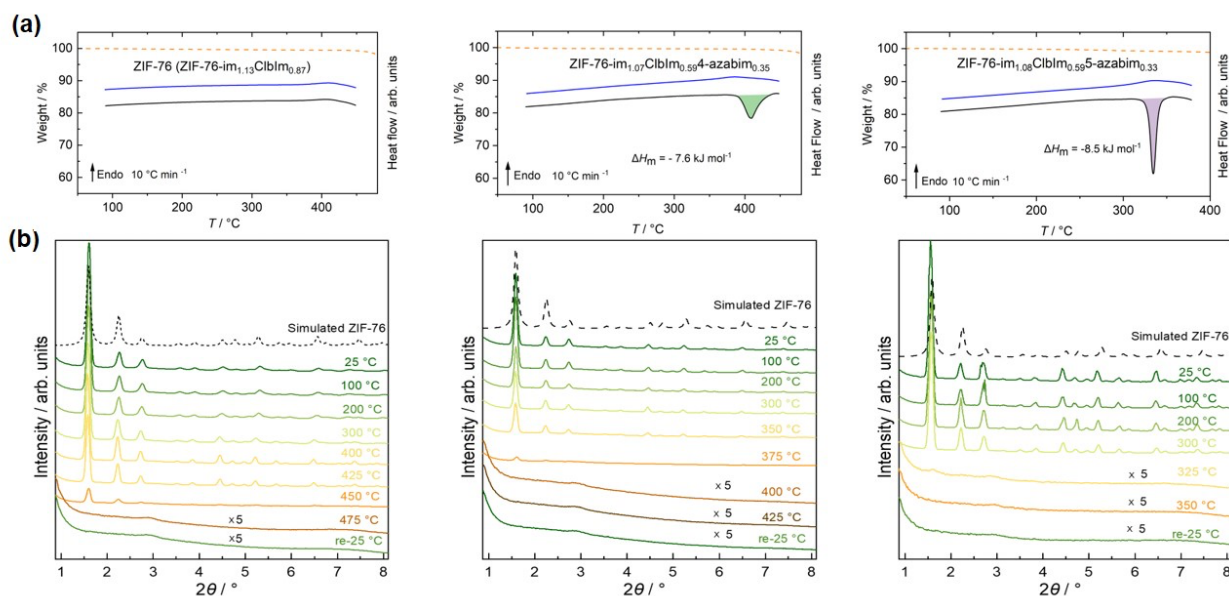


Fig. 2. (a) The TGA (dotted line at the top, left vertical scale) and DSC (black and blue solid line for the 1st and 2nd upscan, right vertical scale) trace of ZIF-76 (left), ZIF-76-im_{1.07}Clbim_{0.59}4-azabim_{0.35} (middle), and ZIF-76-im_{1.08}Clbim_{0.59}5-azabim_{0.33} (right). The samples were cycled from 90 °C to 380 °C or 450 °C with a heating rate of 10 °C min⁻¹. (b) VT-PXRD data of ZIF-76 (left), ZIF-76-im_{1.07}Clbim_{0.59}4-azabim_{0.35} (middle), and ZIF-76-im_{1.08}Clbim_{0.59}5-azabim_{0.33} (right).

In summary, the data collected at beamline 9 enabled us to monitor the phase transitions of ZIF-76 and various ZIF-76 derivatives. The results clearly indicate that weaker binding linkers lower the collapse and melting temperatures of the porous frameworks.

The VT-PXRD data acquired during this beamtime are part of a manuscript that will be submitted for publication soon. The authors thank the DELTA group for the granted beamtime and the beamline

scientists C. Sternemann and M. Paulus for their invaluable support during the experiments.

4. References

- [1] a) N. Ma, S. Kosasang, E. K. Berdichevsky, T. Nishiguchi, S. Horike, *Chem. Sci.* **2024**, *15*, 7474; b) D. Umeyama, S. Horike, M. Inukai, T. Itakura, S. Kitagawa, *J. Am. Chem. Soc.* **2015**, *137*, 864.
- [2] F. A. Lindemann, *Physik. Zeitschr.* **1910**, *11*, 609-612.
- [3] a) T. D. Bennett, J.-C. Tan, Y. Yue, E. Baxter, C. Ducati, N. J. Terrill, H. H.-M. Yeung, Z. Zhou, W. Chen, S. Henke et al., *Nat. Commun.* **2015**, *6*, 8079; b) L. Frenzel-Beyme, M. Kloß, P. Kolodzeiski, R. Pallach, S. Henke, *J. Am. Chem. Soc.* **2019**, *141*, 12362.
- [4] a) W.-L. Xue, C. Das, J.-B. Weiß, S. Henke, *Angew. Chem. Int. Ed. Engl.* **2024**, *63*, e202405307; b) A. M. Bumstead, M. F. Thorne, A. F. Sapnik, C. Castillo-Blas, G. I. Lampronti, T. D. Bennett, *Dalton Trans.* **2022**, *51*, 13636.
- [5] a) L. Frenzel-Beyme, P. Kolodzeiski, J.-B. Weiß, A. Schneemann, S. Henke, *Nat. Commun.* **2022**, *13*, 7750; b) J. Song, L. Frenzel-Beyme, R. Pallach, P. Kolodzeiski, A. Koutsianos, W.-L. Xue, R. Schmid, S. Henke, *J. Am. Chem. Soc.* **2023**, *145*, 9273.
- [6] R. Gaillac, P. Pullumbi, K. A. Beyer, K. W. Chapman, D. A. Keen, T. D. Bennett, F.-X. Coudert, *Nat. Mater.* **2017**, *16*, 1149.
- [7] A. M. Bumstead, M. L. Ríos Gómez, M. F. Thorne, A. F. Sapnik, L. Longley, J. M. Tuffnell, D. S. Keeble, D. A. Keen, T. D. Bennett, *CrystEngComm*, **2020**, *22*, 3627–3637.

Alloy Development of Austenitic Stainless Steels for Additive Manufacturing

Mahmoud Hussein¹, Arne Röttger¹, Christian Sternemann²

(1) Lehrstuhl Neue Fertigungstechnologien und Werkstoffe (FUW), Bergische Universität Wuppertal, 42651 Solingen, Germany

(2) Fakultät Physik/DELTA, Technische Universität Dortmund, 44221 Dortmund, Germany

Additive manufacturing (AM) builds parts layer by layer from CAD models, enabling complex geometries, efficient material use, and reduced waste compared to smelting and powder metallurgy techniques. Powder Bed Fusion-Laser Beam/Metal (PBF-LB/M) and Directed Energy Deposition-Laser/Arc (DED-L/DED-Arc) offer unique benefits for processing metals, including austenitic stainless steel AISI316L, valued for its corrosion resistance and mechanical properties. However, this steel was developed for conventional arc welding, and its processability, especially the microstructure formation process during the solidification and the subsequent multiple heat insertion behavior of AISI316L under AM conditions, remains underexplored, presenting opportunities for further optimization. Controlling the microstructure is a key challenge in metal additive manufacturing (AM). Unlike conventional methods, which involve uniform thermal conditions, AM processes are characterized by rapid solidification and cyclic thermal exposure, leading to distinct microstructures. These microstructural variations can occur across different AM techniques and within a single build due to the complex thermal cycles caused by repetitive rapid heating and cooling. Such variations influence grain size, phase distribution, and defect formation for austenitic stainless steels, whereby all aspects are critical to material performance. Therefore, optimizing the properties of AM parts requires a thorough understanding of how process conditions, chemical composition, and microstructure interact [1, 2].

Austenitic stainless steels produced through PBF-B/M are often reported to exhibit a fully austenitic microstructure. This outcome is attributed to the high solidification rate, which kinetically favors austenite formation over ferrite. Despite primary ferrite formation being thermodynamically promoted during solidification, its formation is bypassed due to the faster growth kinetics of austenite under rapid cooling conditions. Ferrite provides advantages such as a higher solubility for the elements sulfur (S) and phosphorus (P) and a lower thermal expansion coefficient than austenite. Because of the higher solubility of S and P in ferrite, the formation of low melting phases (Fe_3P , FeS) and the hot cracking susceptibility can be thus reduced. In this study, the alloy composition of 316L will be adapted for the PBF-LB process by adjusting the nickel content, a key austenite stabilizer. Reducing the nickel content is expected to promote primary ferritic solidification and facilitate the retention of the δ -ferrite phase in the PBF-LB/M processed microstructure despite the high solidification rate. [3]

Casted cylindrical samples with a diameter of 20 mm were developed using an Indutherm MC16 melting furnace. The samples were used for surface remelting over a flat area of 100 mm² via PBF-LB/M utilizing Aconity MIDI (parameters see **Table 2**) to imitate the additive manufacturing process concerning the last applied layer of a solid part. The chemical

compositions of the investigated samples are listed in **Table 3** and were determined by optical spark emission spectrometry of the casted samples.

Table 3: chemical composition of casted samples in weight percentage (wt. %)

Element	C	Si	Mn	Cr	Mo	Ni	P	S	Fe
Sample 1	0.03	0.27	1.23	17.33	2.06	8.67	0.04	0.02	Bal.
Sample 2	0.04	0.35	1.61	17.40	2.13	9.57	0.06	0.02	Bal.
Sample 3	0.04	0.35	1.60	17.40	2.14	10.65	0.06	0.02	Bal.
Sample 4	0.03	0.34	1.30	17.37	2.23	11.90	0.06	0.02	Bal.
Sample 5	0.03	0.31	1.21	17.47	2.05	12.90	0.04	0.02	Bal.

Table 2: parameters for surface melting

Laser Power (W)	120
Scan Speed (mm/s)	800
Hatch distance (mm)	0.08

Table 1: Ferrite phase content in each sample (vol.%)

Sample 1	55 %
Sample 2	47 %
Sample 3	30 %
Sample 4	5 %
Sample 5	4 %

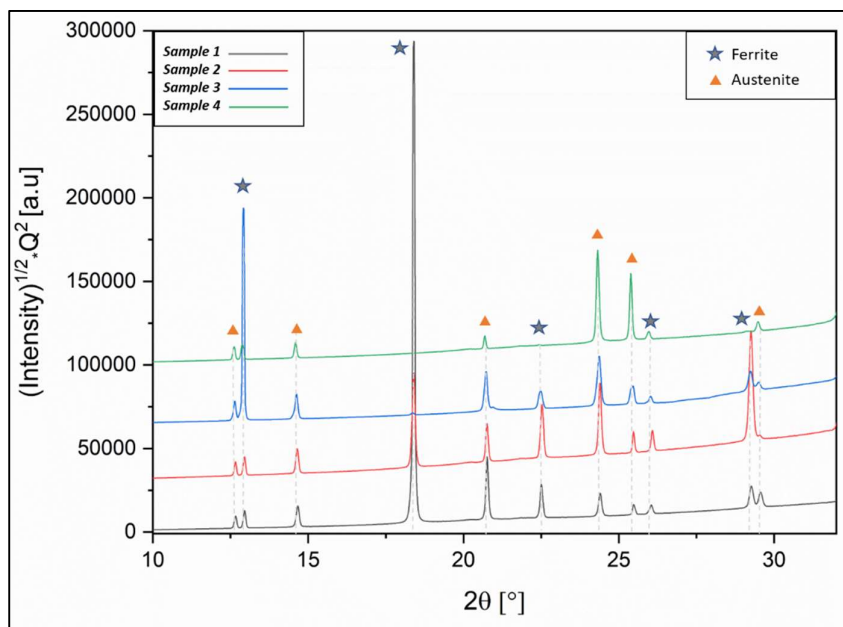


Figure 1: Synchrotron XRD diffraction peaks for the designed alloys

The synchrotron XRD diffractogram shown in **Figure 1** revealed only two phases, austenite, and ferrite, with δ -ferrite content decreasing significantly as Ni concentration increased. Sample 5 was measured separately with different experimental parameters and therefore it is not

included due to misalignment with the other spectrums, it was nevertheless characterized in terms of phase volume fractions. In **Table 1**, Sample 1, with the lowest Ni content (8.67 wt.%), showed the highest δ -ferrite content (55 vol.%), while Sample 5, with the highest Ni content (12.9 wt.%), had just 4 vol.%. Correspondingly, ferrite-related peaks in the spectra weakened and disappeared at higher Ni levels, including a prominent peak at $2\theta \approx 17^\circ$ absent in Samples 3 & 4. The findings indicate that Ni strongly stabilizes the austenite phase, suppressing δ -ferrite formation by altering the solidification pathway. These results highlight the potential for microstructural tailoring through Ni content adjustment for each additive manufacturing process depending on the different corresponding process conditions.

References

- [1] T. Pereira, J. V. Kennedy, and J. Potgieter, "A comparison of traditional manufacturing vs additive manufacturing, the best method for the job," *Procedia Manufacturing*, vol. 30, pp. 11–18, 2019, doi: 10.1016/j.promfg.2019.02.003.
- [2] D. Ding, Z. Pan, D. Cuiuri, and H. Li, "Wire-feed additive manufacturing of metal components: technologies, developments and future interests," *Int J Adv Manuf Technol*, vol. 81, 1-4, pp. 465–481, 2015, doi: 10.1007/s00170-015-7077-3.
- [3] J. M. Vitek, A. Dasgupta, and S. A. David, "Microstructural modification of austenitic stainless steels by rapid solidification," *Metallurgical transactions A*, vol. 14, pp. 1833–1841, 1983.

X-ray diffraction analysis of chemically complex TiSiBCN nanocomposites

Wolfgang Tillmann¹, Julia Urbanczyk^{1,*}, Ahmad Zahid Ebady¹, Nelson Filipe Lopes Dias¹
Alexander Thewes², Günther Bräuer²

¹Institute of Materials Engineering, TU Dortmund University, Leonhard-Euler-Str. 2, D-44227 Dortmund

²Institute for Surface Technology, TU Braunschweig, Field Office Dortmund, Eberhardstr. 12, D-44145 Dortmund, Germany

*corresponding author: julia.urbanczyk@tu-dortmund.de

Tools used in forming processes experience high mechanical and tribological stresses. Tailored nanocomposites offer a high potential to enhance tool durability by improving wear resistance and mechanical performance [1,2]. Among these, TiSiBCN thin films have demonstrated promising tribo-mechanical properties, dependent on their nanostructure [3,4]. Previous studies have shown that the chemical composition of TiSiBCN influences its phase structure and, consequently, the tribo-mechanical properties. However, mainly the effect of varying one element at a time like N has been investigated [4]. By considering the sub-systems of TiSiBCN it becomes clear that the phase formation is an interaction of the content levels of either B [5,6], C [7,8], and N [8]. In a magnetron sputtering process using a Design of Experiments (DoE) approach, varying B, C, and N, the impact of the chemical composition on the phase structure, which ultimately influences the tribo-mechanical properties of TiSiBCN thin films was investigated. Therefore, the phase structure was analyzed by x-ray diffraction (XRD).

The thin films were applied on high-speed steel (AISI M2) discs ($d = 30$ mm, $t = 5$ mm) with a hardness of 60 HRC using an industrial magnetron sputtering device CC800/9 Custom (CemeCon AG, Germany). To ensure a sufficient adhesive strength of the TiSiBCN thin films a Ti/TiN/TiSiN interlayer system was applied [9]. Using a face-centered central composite design (CCD) with a central point the B content was changed by the cathode power P_c of the TiB₂/TiSi₂ targets (ratio of 80/20 mol. %) on the levels 3, 4, and 5 kW, the C content by the acetylene (C₂H₂) and the N content by the nitrogen (N₂) gas flow rate $q_{C_2H_2}$ on 5, 12.5, and 20 sccm and q_{N_2} on 10, 40, and 70 sccm, respectively, conducting a total of 15 experiments (see Table 1).

Table 1: Factor levels of the cathode power P_c on the TiB₂/TiSi₂ targets, C₂H₂ gas flow rate $q_{C_2H_2}$, and N₂ gas flow rate q_{N_2}

Factor		Level		
TiB ₂ /TiSi ₂ cathode power	P_c (kW)	3	4	5
C ₂ H ₂ gas flow rate	$q_{C_2H_2}$ (sccm)	5	12.5	20
N ₂ gas flow rate	q_{N_2} (sccm)	10	40	70

The crystalline structure was investigated with XRD at beamline BL9 of DELTA synchrotron radiation source equipped with an image plate detector (MAR345) with a photon energy of 27 keV, beam width of 0.7 mm and height of 0.1 mm under an incidence angle of 0.5 °.

Due to the TiN-based interlayer system, the diffraction angles show overlays and overlapping, which complicates a precise analysis. Therefore, the substrate and interlayer patterns are additionally analyzed (see Figure 1). The pattern of the substrate exhibits α -Fe at 12.9° and Me_6C metal carbides at 10.4° , 11.6° , 12.4° , 13.5° , and 18.4° . Ti/TiN/TiSiN exhibits a Bragg diffraction at 11.1° , corresponding to (111) β -Ti and (002) α -Ti, while the asymmetric reflection at 11.6° with a broader shoulder indicates (101) α -Ti from the first Ti interlayer. The broad TiN (111), (200), and (202) peaks result from overlapping TiN phases in the TiN and TiSiN interlayers, with right-shoulder broadening attributed to TiN crystallites in the TiSiN interlayer [9]. The described Bragg diffraction can also be found in the TiSiBCN top layers. Overall, the XRD patterns are very similar. The main differences appear at the angles from 10.5° to 11.0° and 17.3° to 18.0° as the intensity and distribution change. To examine the influence of the B, C, and N content the thin films with the highest concentration of each were compared. The reflections in the mentioned 2θ ranges consist of cubic TiC (10.6° , 12.3° , 17.4°), cubic TiN (10.7° , 12.4° , 17.6°) as well as cubic TiB (10.9° , 12.6° , 17.8°). A similar composition was observed by Tsai *et al.* [10]. The main focus is on (111) as it shows the most pronounced changes. For $\text{Ti}_{26}\text{Si}_9\text{B}_{46}\text{C}_4\text{N}_{12}$ with the highest B content (46.0 ± 0.7 at.-%), the (111) and (202) reflections shift toward lower angles indicating TiB superposition, which could be attributed to the incorporation of N in TiB [3,11]. Further, B incorporation into TiN broadens and diminishes the (111) TiN reflection, likely from reduced crystallite size [12]. Additionally, B may form amorphous phases like a-BN and a-TiB₂, inhibiting crystallite growth [3,8]. $\text{Ti}_{19}\text{Si}_7\text{B}_{28}\text{C}_{32}\text{N}_{11}$, with the highest C content (31.7 ± 0.4 at.-%), exhibits a shoulder formation for (111) TiC and a broadening of (111) and (202) occurs. In TiCN thin films, C promotes the formation of amorphous phases like a-C and a-CN, though TiC bonds increase with higher C content [13]. Shoulder formations and broadening of (111) and (202) diffractions suggest C incorporation into TiN as a solid solution. In TiBCN nanocomposites, C forms solid solutions of Ti(B,C) and Ti(N,C), reducing crystallite size [8]. Overall, TiN remains the dominant crystalline phase due to its lower Gibbs free energy [14]. $\text{Ti}_{18}\text{Si}_6\text{B}_{22}\text{C}_9\text{N}_{41}$, with the highest N content (40.6 ± 0.4 at.-%), shows a symmetric (111) TiN peak, as it is expected to be the main phase. The addition of N transforms α -Ti to Ti₂N and TiN, shifting α -Ti (002) peak to lower angles due to interstitial incorporation [15]. Superposed peak broadening could reflect crystallite refinement and the development of amorphous phases like a-C, a-CN, a-BN, a-Si₃N₄, and a-TiB₂ with varying C, N, and B content [3,5,8,16].

The noticed changes in peak position among the three XRD patterns reflect lattice distortion by the interstitial incorporation of atoms or as a result of the formation of solid solutions induced by the substitution of atoms, characterized by a peak shift towards smaller diffraction angles.

Additionally, a variation in the degree of crystallinity or ratio of TiC, TiN, or TiB changes the peak position and/or shape due to changes in intensities. Considering the potential nanocomposite structure, an increased ratio of amorphous-to-crystalline phase typically results in a reduced crystallite size broadening the diffraction peaks. However, no definitive correlation between phase composition and chemical composition has been identified. The XRD diffraction patterns indicate varying amounts of crystalline Ti(C,N) and TiB phases, which are likely embedded within different amorphous phases.

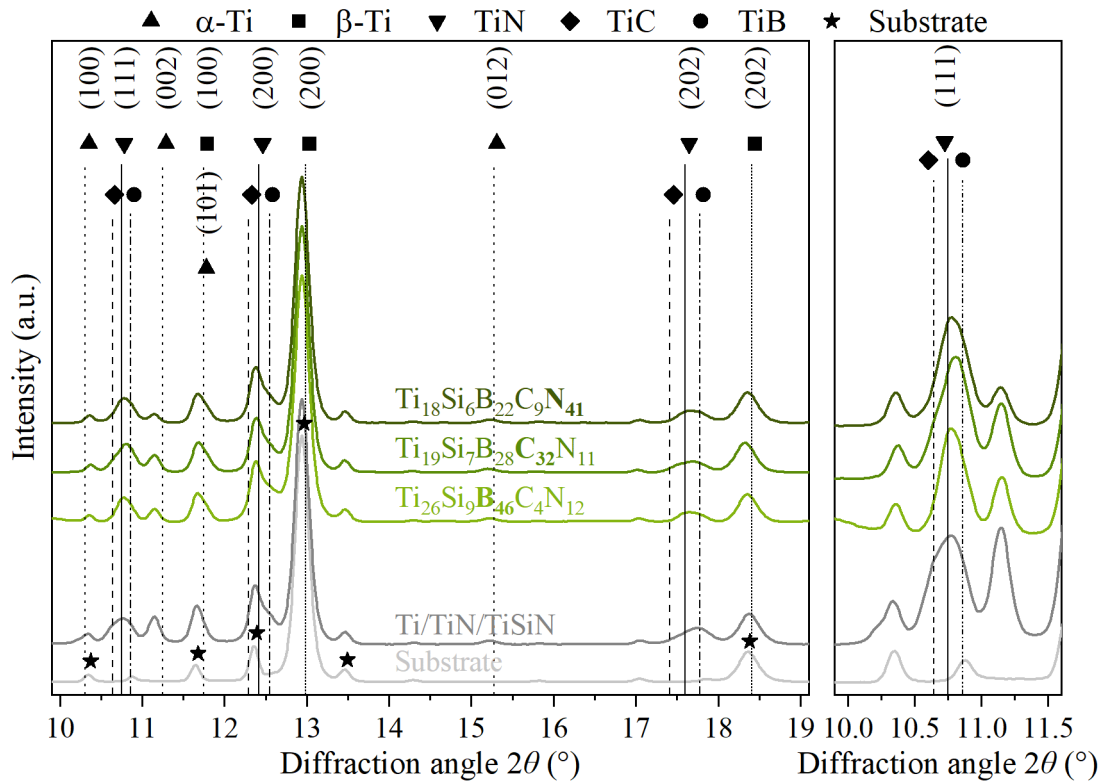


Figure 1: XRD patterns of the AISI M2 substrate, the Ti/Ti/TiSiN interlayer, and the TiSiBCN thin film systems with the highest B, C, and N content (left) and with the enlarged (111) diffraction (right)

The chemical composition of the TiSiBCN thin films affects phase formation. The XRD analyses performed at the BL9 were crucial for obtaining comprehensive understanding of the phase evolution of TiSiBCN depending on the amounts of N, C, and B. In complementary investigations, it was observed that the structural properties of the TiSiBCN thin films affect the tribomechanical properties. The introduced $(C+N+Si)/(Ti+B)$ chemical ratio is indicated by rising to a softer film with reduced hardness and elastic modulus. The DoE approach helps to predict and optimize these properties for specific tool applications.

Acknowledgments: The authors gratefully acknowledge the financial support by the Deutsche Forschungsgemeinschaft (DFG, German Research Foundation) in the project “*Fundamental investigations of the temperature-dependent self-organization of PECVD- and PVD-TiSiBCN thin films*” (funding numbers BR 2178-59-1 and TI 343/180-1). In addition, The authors thank

the DELTA for providing synchrotron radiation and for the technical support at beamline BL9 during the X-ray diffraction.

Presentation to a scientific audience: The study entitled “*Investigating the influence of B, C, and N on the tribo-mechanical properties of the chemically complex TiSiBCN thin films using design of experiments*” included the previously shown results and was presented as an oral talk at the 50th International Conference on Metallurgical Coatings and Thin Films, which took place on May 19-24, 2024 in San Diego.

References

- [1] E.O. Ezugwu, C.I. Okeke, Tool life and wear mechanisms of TiN coated tools in an intermittent cutting operation, *Journal of Materials Processing Technology* 116 (2001) 10–15. [https://doi.org/10.1016/S0924-0136\(01\)00852-4](https://doi.org/10.1016/S0924-0136(01)00852-4).
- [2] E.J.A. Armarego, S. Verezub, P. Samaranayake, The effect of coatings on the cutting process, friction, forces and predictive cutting models in machining operations, *Proceedings of the Institution of Mechanical Engineers, Part B: Journal of Engineering Manufacture* 216 (2002) 347–356. <https://doi.org/10.1243/0954405021520012>.
- [3] I.W. Park, B. Mishra, K.H. Kim, J.J. Moore, Multifunctional Ti-Si-B-C-N Tribological Nanocomposite Coatings for Aerospace Applications, *MSF* 539-543 (2007) 173–180. <https://doi.org/10.4028/www.scientific.net/MSF.539-543.173>.
- [4] A. Thewes, L. Bröcker, E.T.K. George, G. Bräuer, M. Paulus, C. Sternemann, H. Paschke, T. Brückner, S. Lechner, S. Müller, Ti-Si-B-C-N plasma enhanced chemical vapor deposition nanocomposite coatings for high temperature applications, *Thin Solid Films* 760 (2022) 139507. <https://doi.org/10.1016/j.tsf.2022.139507>.
- [5] K.H. Kim, J.T. Ok, S. Abraham, Y.-R. Cho, I.-W. Park, J.J. Moore, Syntheses and mechanical properties of Ti-B-C-N coatings by a plasma-enhanced chemical vapor deposition, *Surface and Coatings Technology* 201 (2006) 4185–4189. <https://doi.org/10.1016/j.surfcoat.2006.08.051>.
- [6] Y.H. Lu, Y.G. Shen, K.Y. Li, H. Chen, Effects of nitrogen content on nanostructure evolution, mechanical behaviors and thermal stability in Ti-B-N thin films, *Surface and Coatings Technology* 201 (2006) 1228–1235. <https://doi.org/10.1016/j.surfcoat.2006.01.045>.
- [7] Q.H. Luo, Y.H. Lu, Microstructure and mechanical properties of reactive magnetron sputtered Ti-B-C-N nanocomposite coatings, *Applied Surface Science* 258 (2011) 1021–1026. <https://doi.org/10.1016/j.apusc.2011.08.053>.
- [8] J. Lin, J.J. Moore, B. Mishra, M. Pinkas, W.D. Sproul, The structure and mechanical and tribological properties of TiBCN nanocomposite coatings, *Acta Materialia* 58 (2010) 1554–1564. <https://doi.org/10.1016/j.actamat.2009.10.063>.
- [9] W. Tillmann, J. Urbanczyk, A. Thewes, G. Bräuer, N.F. Lopes Dias, Effect of the TiSiN interlayer properties on the adhesion and mechanical properties of multilayered TiSiCN thin films, *Surface and Coatings Technology* 478 (2024) 130467. <https://doi.org/10.1016/j.surfcoat.2024.130467>.
- [10] P.-C. Tsai, W.-J. Chen, J.-H. Chen, C.-L. Chang, Deposition and characterization of TiBCN films by cathodic arc plasma evaporation, *Thin Solid Films* 517 (2009) 5044–5049. <https://doi.org/10.1016/j.tsf.2009.03.029>.
- [11] W. Gissler, Structure and properties of Ti-B-N coatings, *Surface and Coatings Technology* 68-69 (1994) 556–563. [https://doi.org/10.1016/0257-8972\(94\)90217-8](https://doi.org/10.1016/0257-8972(94)90217-8).
- [12] I. Asempah, J. Xu, L. Yu, H. Ju, F. Wu, H. Luo, Microstructure, mechanical and tribological properties of magnetron sputtered Ti-B-N films, *Surface Engineering* 35 (2019) 701–709. <https://doi.org/10.1080/02670844.2019.1575569>.
- [13] Y.H. Cheng, T. Browne, B. Heckerman, Influence of CH₄ fraction on the composition, structure, and internal stress of the TiCN coatings deposited by LAFAD technique, *Vacuum* 85 (2010) 89–94. <https://doi.org/10.1016/j.vacuum.2010.04.007>.
- [14] Thomas C. Allison, NIST-JANAF Thermochemical Tables - SRD 13, National Institute of Standards and Technology, 2013.
- [15] F. Vaz, J. Ferreira, E. Ribeiro, L. Rebouta, S. Lanceros-Méndez, J.A. Mendes, E. Alves, P. Goudeau, J.P. Rivière, F. Ribeiro, I. Moutinho, K. Pischow, J. de Rijk, Influence of nitrogen content on the structural, mechanical and electrical properties of TiN thin films, *Surface and Coatings Technology* 191 (2005) 317–323. <https://doi.org/10.1016/j.surfcoat.2004.01.033>.

- [16] P. Mahato, R.J. Singh, L.C. Pathak, S.K. Mishra, Effect of nitrogen on mechanical, oxidation and structural behaviour of Ti–Si–B–C–N nanocomposite hard coatings deposited by DC sputtering, *Surface & Interface Analysis* 48 (2016) 1080–1089. <https://doi.org/10.1002/sia.6030>.

Development and structure analysis of thermally sprayed Quasi-crystalline (QC) Al-Cu-Fe coatings

*Ingor Baumann¹, Mukul Aravind Kada¹, Jonas Zajaczkowski¹, Wolfgang Tillmann¹
Christian Sternemann², Michael Paulus², Marko Sipura³, Nenad Piljic⁴*

¹Institute of Materials Engineering, TU Dortmund University, Dortmund, Germany

²Faculty of Physics/ DELTA, TU Dortmund University, Dortmund, Germany

³MD Global Trading GmbH, Bad Wimsbach, Austria

⁴DANEN TRADE GmbH, Salzburg, Austria

**Corresponding author: ingor.baumann@tu-dortmund.de*

Quasicrystalline materials (QCM) were discovered in the early 1980s and are therefore a comparatively young group of materials. Because of their interesting properties, QCM have been the focus of various research works. The thermal and current transport properties make QCM ideal for instance for use in solar absorbers. Due to their unique atomic structure, QCMs are also suitable for storing gases such as hydrogen. The low surface energy, which leads to non-stick properties, has been investigated for use in frying pans and airplane trays as an alternative to thermally susceptible PTFE. QCM are usually ternary alloys with aluminium, zinc, cadmium, or titanium as the main constituent. The structure exhibits a five-, eight-, ten- or twelve-fold symmetry that fundamentally differs from crystalline materials. While atoms or molecules in crystalline materials are arranged in a periodic structure that repeats in each of the three spatial directions as an identical pattern, the elementary building blocks in QCM are arranged in an ordered but aperiodic structure. Studies using XRD analysis revealed a unique pattern with sharp diffraction points that exhibit the typical icosahedral or decagonal structure [1, 2]. Other studies showed that there is a relationship between quasicrystals and the Penrose tiling pattern [1, 7]. However, the fundamental relationships between the structure and the resulting properties of QCM are not yet fully understood. Many QCM materials have already been discovered. They are classified into two groups: Stable and metastable quasicrystals. Among them, metastable Al-Cu-Fe alloys with striking pentagonal facets, following an icosahedral (fivefold) symmetry, are mostly interesting and most-studied due to their favourable properties at low cost [3].

To incorporate surfaces of tools and components with QCM, thermal spray processes can be used in a very efficient way. Several studies have been conducted to determine the unique combination of physical and mechanical properties of these materials, such as high micro hardness, low coefficients of friction, low thermal and electrical conductivity as well as non-stick properties [3, 8]. However, QCM are complex alloys with individual elements having also very different properties, such as density and melting point for example. In addition,

they are very brittle and partially metastable. This complicates their processing by means of thermal spraying. In addition, the production of QCM is complex and costly due to the complex equilibrium compositions in ternary phase diagrams and the lack of clear guidelines for synthesis.

In this study plasma spraying (PS) of quasicrystalline (QC) Al-Cu-Fe powders with irregular structure and a size fraction of 40 – 63 μm was performed and investigated to explore the potentials of the material to produce sliding wear resistant and low friction coatings with anti-stick properties as part of a master's thesis. The powder feedstock was derived from a novel manufacturing process that enables the production of such powders on a large scale. Cross-section images taken by scanning electron microscopy (SEM) and a particle size distribution (PSD) of the powder, determined by laser diffractometry are demonstrated in **Figure 1**.

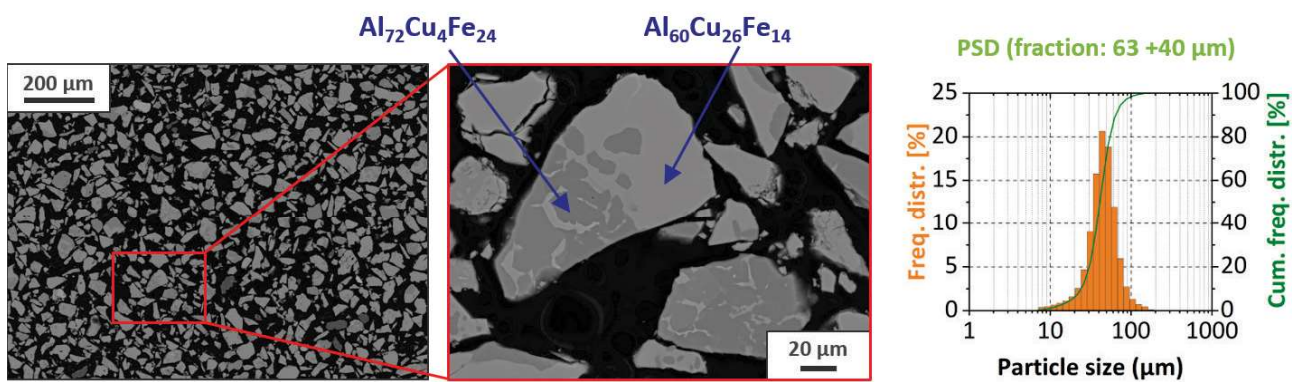


Figure 1: Effect of the spray parameters on the QC coating properties.

The percentiles of this powder fraction are: $d_{10} = 22.4 \mu\text{m}$, $d_{50} = 34.6 \mu\text{m}$ and $d_{90} = 53.4 \mu\text{m}$. It features an acceptable flowability when it was transferred from the powder feeder system into the plasma spray gun.

A “One Factor at a Time (OFAT)” parameter study was conducted to find suitable plasma spray parameters to process the QC powder and to study their effects on the coating of mild-steel samples. The coatings were characterised regarding their mechanical (layer thickness, porosity, roughness, micro hardness), morphological (qualitative assessment of the microstructure) and tribological (sliding wear behaviour, sliding wear coefficient) properties as well as their phase evolution with synchrotron radiation. During the spray experiments, the fraction of QC phases in the coatings was projected to be maximised and their influence on the microstructure as well as on the tribo-mechanical properties was examined. The parameters that were included as variables in the OFAT analysis were current (200; 300; 400 A), spray distance (90; 135; 180 mm), argon flow (40; 70; 100 l/min) and the hydrogen flow (2; 4; 6; 8 l/min). Each of the parameters were given a set of values based on previous experience and the analysis was conducted. hydrogen flow was specifically studied to understand the effect of introducing higher thermal energy into the process. It was also

essential to maintain the stability of the QC phases of the powder in the coating. From the OFAT analysis, trends and effective parameter sets were derived, which can be found in **Figure 2**. The in-flight velocity and temperature of the spray particles during plasma spraying were determined for all parameter sets to correlate and identify useful metrics. This assessment was done using an Accuraspray G3 sensor (Tecnar, Canada).

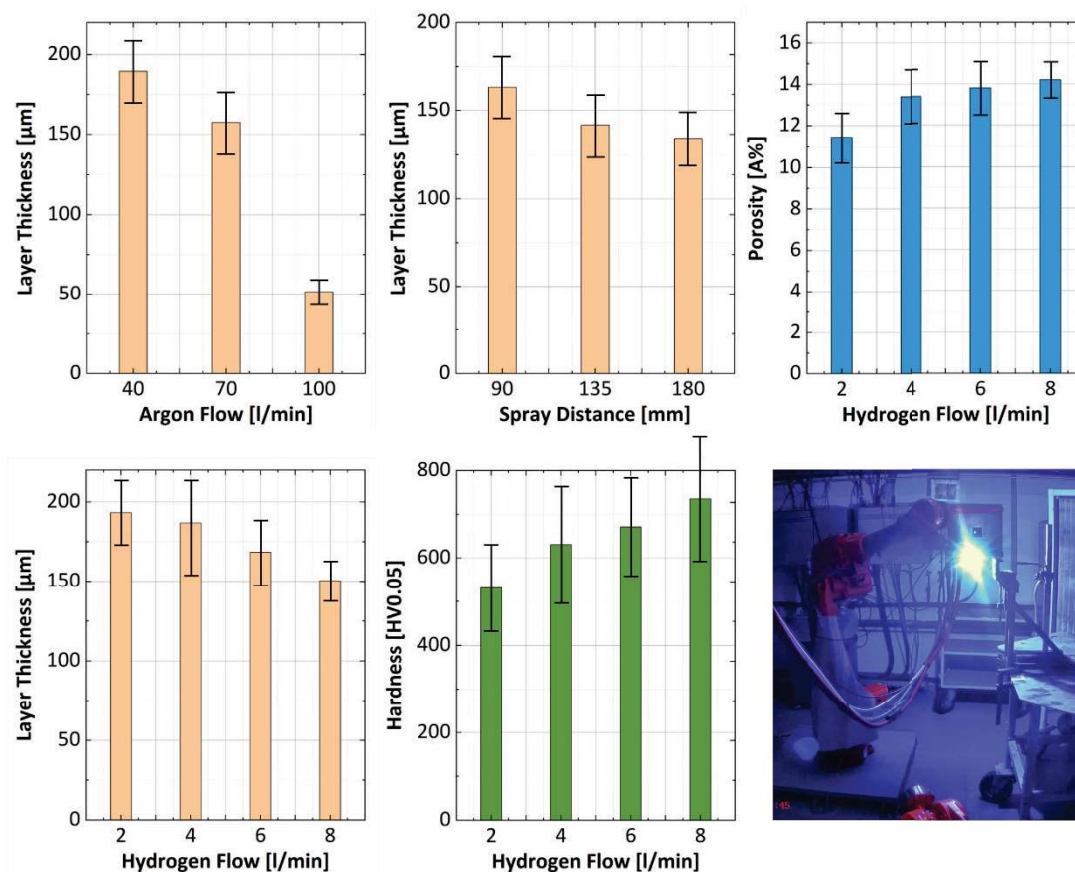


Figure 2: Effect of the spray parameters on the QC coating properties.

It was found that increasing the hydrogen flow rate from 0 to 8 l/min leads to a slightly higher plasma power (15.5 to 17.6 kW) and a higher particle temperature (2,460 to 3183°C). The coating thickness depends mainly on the argon flow rate and the spray distance. Lower argon flow rates (40 l/min) and shorter spray distances (90 mm) should be favoured for higher coating layer thickness. In addition, higher hydrogen flow rates also led to an increase in the micro hardness (531.6 ± 98.6 to 735.7 ± 115.7 HV 0.05) but also to higher coating porosity ($6.24 \pm 0.8\%$ to $15.46 \pm 3.4\%$). Since this microstructural relationship usually leads to the opposite result, special attention was paid to the phase development in the QC coating. The phase evolution in the powder (using a capillary) and the coatings were analysed with synchrotron radiation at Beamline 9 (DELTA, TU Dortmund University). **Figure 3** demonstrates the setup for both analyses. The following methods and parameters were chosen for the diffraction experiments:

- Detector: Mar345
- Photon energy in eV: 27 MeV
- Wavelength in Å: 0.4592009259259259
- Angle: 3°
- Measuring time powder: 10 seconds (in capillary)
- Measuring time coating: 200 seconds

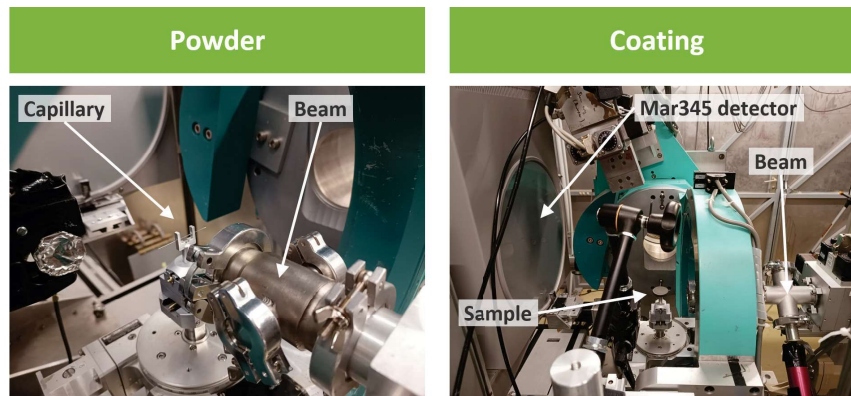


Figure 3: Experimental setup of the diffraction experiments for the powder and the coating on Beamline 9 (DELTA, TU Dortmund University).

Figure 4 shows cross-sectional images of the QC coating produced with the best parameters (sample C3.1: argon flow rate 70 l/min; spray distance 135 mm and current 400 A) as well as its properties and the deposition efficiency of the spray process.

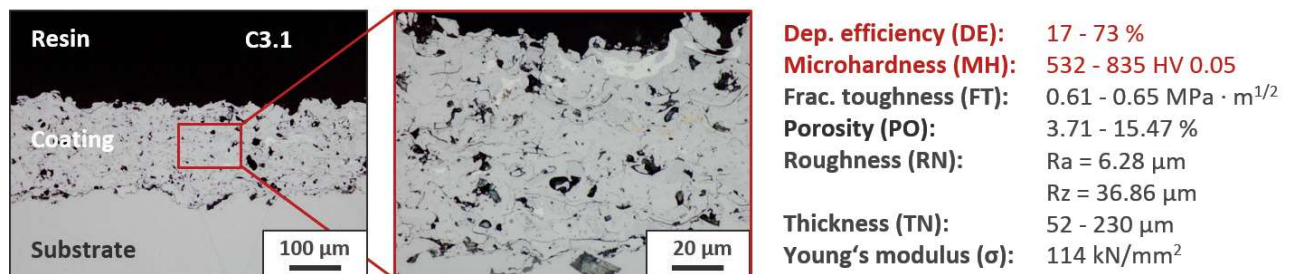


Figure 4: Cross-section images and properties of the coating sprayed with best parameters

The SEM images reveal a well-adhering QC coating on mild steel with high microhardness compared to other common (unhardened) metallic coatings, making the coating suitable for wear purposes. However, an inherent minimum porosity of around 3.7 % could not be eliminated during plasma spraying for technical reasons. In addition, a good deposition efficiency around 65 % could be realized.

Due to the special symmetry of the QC powders and coatings, a direct determination and assignment of the phases by means of a typical phase analysis for crystalline materials (using a database) was not possible. In the latter, it is assumed that the crystal is completely built

up by a periodical arrangement of elementary cells which, by displacements, fills the entire crystal without gaps. However, this does not apply to a quasicrystal with fivefold symmetry such as Al-Cu-Fe, as the atoms have a long-range atomic order without clear periodicity. The evaluation of the diffraction peaks was therefore conducted with the help of literature. The diffraction patterns of the works of Pillaca et al. [1], Fleury et al. [2] and Sordelet et al. [3] were used, since these researchers were able to prove that the peaks are quasicrystals by determining their Miller's indices.

Figure 5 illustrates the diffraction patterns with the determined peaks of the employed QC powder composed of Al = 45.42 at.-%, Cu = 32.90 at.-% and Fe = 21.68 at.-%. The red star symbolizes the quasicrystalline fractions determined from the literature comparison and the green triangle indicates the AlFe solid solution phase. The green squares represent a mixture of Fe/Al₂Cu according to Fleury et al. [2]. The powders were found to contain a high proportion of quasicrystalline phases. By combining XRD, EDS, WDS and differential thermal analyses (DTA) with CALPHAD simulations, the following well-known, but also other non-stoichiometric QC phases could be identified: Al₇Cu₂Fe, Al₆₅Cu₂₀Fe₁₅, Al₆₅Cu₂₂Fe₁₃, Al₆₅Cu₂₃Fe₁₂, Al₆₂Cu₂₅Fe₁₃, Al_{76.5}Cu_{5.5}Fe₁₈, Al_{68.5}Cu_{20.25}Fe_{11.25}.

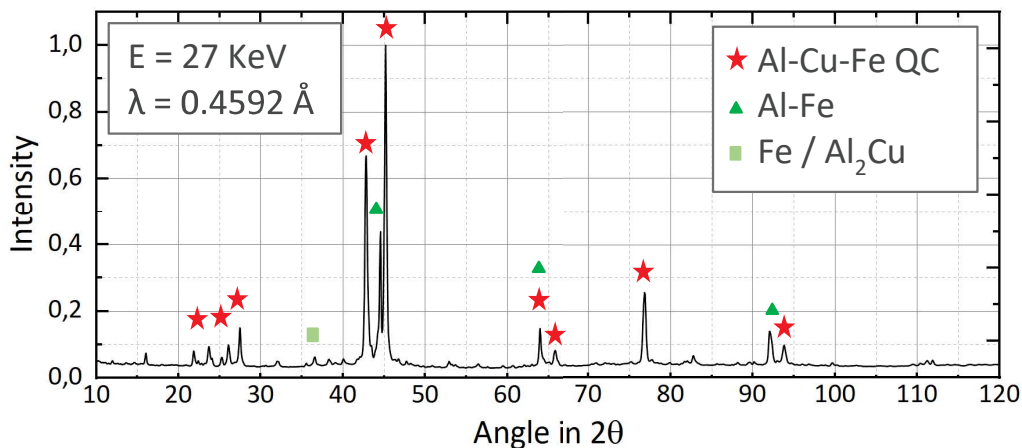


Figure 5: Diffraction patterns with the determined peaks of the Al-Cu-Fe QC powder.

The XRD profile obtained from the powder was compared to the plasma sprayed coatings with various parameters to determine the presence of a valid QC phase. This was done by comparing the peaks represented by red stars in the profile. The differences in the peaks obtained by different parameter sets were studied. In **Figure 6** as-sprayed coating with best parameters (sample C3.1) but no hydrogen flow rate was compared to the samples with low (2 l/min, W1.3) and high (8 l/min, W3.2) hydrogen flow rates. The C3.1 diffraction pattern shows a close similarity to the one of the powders. The aforementioned QC peaks denoted by red stars are mostly preserved in this coating with very slight oxide formation indicated by the green squares in the profile. It was found that the introduction of hydrogen flow in the process leads to a significant reduction of QC phases in the coating as visible from **Figure 6**. The QC peaks are found to be recessed with their heights reduced. Also, an

increase in oxide phases can be visualized when compared to the default spray coating. At a hydrogen flow rate of 2 l/min, however, there is a slight reduction in the QC peaks with added oxide phases, which are marked with green squares, but the QC phases remain largely intact throughout the range. At increased hydrogen flow of up to 8 l/min, there is complete elimination of most QC phases with a large dominance of oxide phases in the coating.

After the coating development and phase analyses the sliding wear behaviour of the plasma sprayed coatings with low hydrogen flow rate of 2 l/min was evaluated using a ball-on-disc test with a \varnothing 6 mm Al_2O_3 ball as a counter body, 800 m wear distance, a load of 10 N and a sliding velocity of $v = 0.4$ m/s.

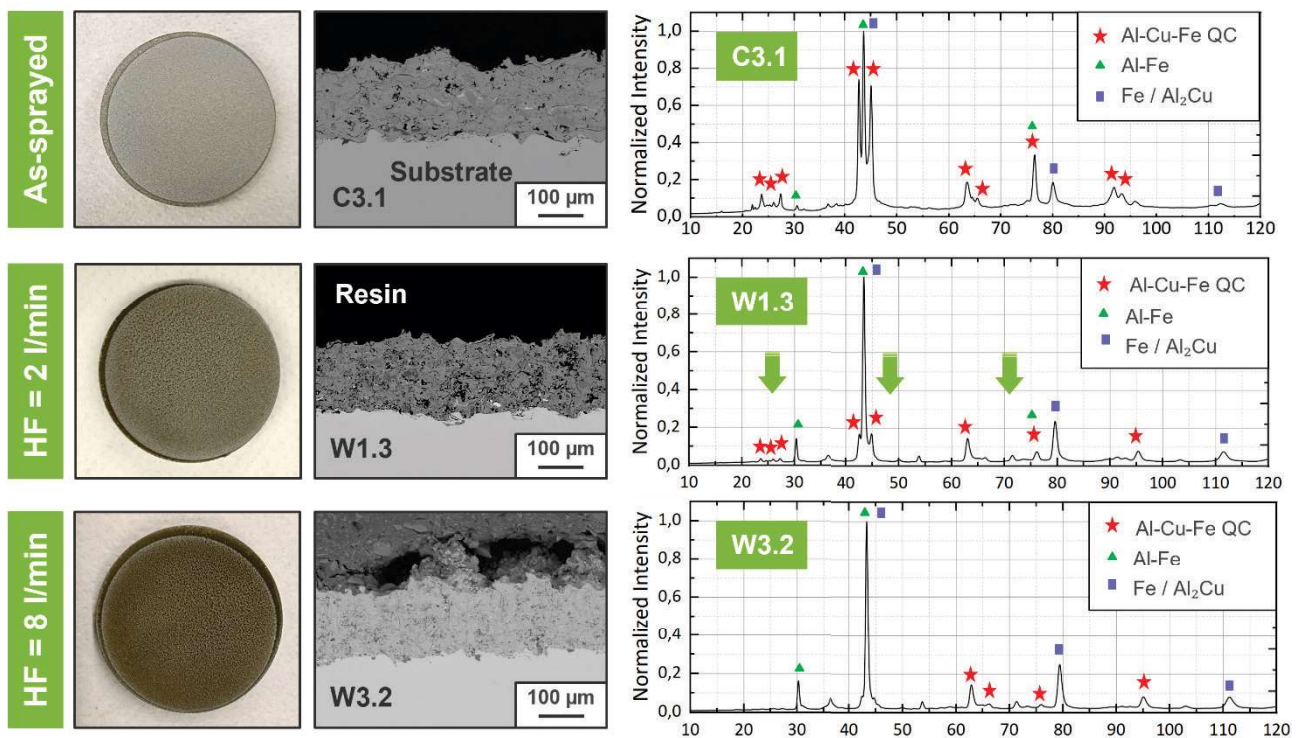


Figure 6: Coated samples, cross-section images of the microstructure and diffraction patterns of coatings sprayed with different hydrogen flow rates.

The friction coefficients and debris formation in the wear track for the coatings are shown in **Figure 7**. The friction performance of the coating was found to be satisfactory with a coefficient of friction around 0.43 - 0.49. The addition of hydrogen flow in the process improves the overall tribological performance, with a low sliding wear coefficient of $10.51 \cdot 10^{-5} \text{ mm}^3/\text{Nm}$. With this value the QC coatings achieve a better sliding wear performance compared to standard coatings in this field like Ni-5wt.%Al, FeVCrC, Cr_3C_2 - NiCr and tool steel [5, 6]. The oxide phases formed with inclusion of hydrogen flow increase both the micro hardness and the sliding wear behaviour.

It can be concluded from this study that plasma spraying of Al-Cu-Fe powders could be performed successfully. QC coatings with high micro hardness, acceptable porosity, moderate

friction coefficient and very good sliding resistance could be produced on mild steel. Suitable spray parameters were identified and their effects on the coating properties and QC phase evolution were examined. It was found that the coating thickness mainly depends on the argon flow rate and the spray distance, whereas higher hydrogen flow rates led to an increase in the micro hardness but also produces higher porosity. Plasma spraying with low hydrogen flow rates has proven to be particularly suitable for producing good wear properties.

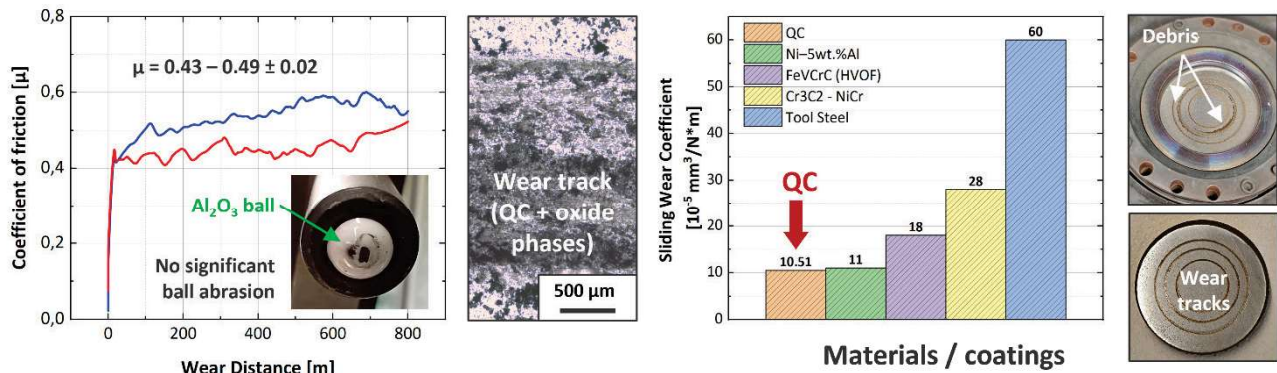


Figure 7: Friction coefficients and debris formation in the wear track of plasma coating.

Thanks to higher process temperatures, useful oxide phases develop in the coating microstructure which improved the sliding wear resistance of the coatings. Thus, a better wear performance compared to standard coatings in this field could be achieved. At the same time, however, there is no significant reduction in the QC phases, so that the coefficient of friction is not negatively affected. However, spraying with high hydrogen flow rates is not recommended due to the intense heat development during spraying resulting in a massive loss of QC phases. From a scientific point of view, these influences are highly interesting and should be investigated in further studies. The quasicrystalline material family of Al-Cu-Fe is a complex system that merits further development and research in the field of thermal spraying.

Acknowledgements

The authors would like to thank the DELTA of TU Dortmund University for the use of Beamline 9 and for the scientific support during the phase analyses.

Literature

- [1] M. Pillaca Quispe, C. V. Landauro, M. Z. Pinto Vergara, J. Quispe-Marcatoma, C. Rojas-Ayala, V. A. Peña-Rodríguez, E. Baggio-Saitovitch: „Influence of high energy milling on the microstructure and magnetic properties of the Al–Cu–Fe phases: the case of the i -Al 64 Cu 23 Fe 13 quasicrystalline and the ω -Al 70 Cu 20 Fe 10 crystalline phases", RSC Advances", 2016.
- [2] E. Fleury, S. Lee, W. Kim, D. Kim: „Effects of air plasma spraying parameters on the Al–Cu–Fe quasicrystalline coating layer", Journal of Non-Crystalline Solids", 2000.

- [3] D. J. Sordelet, M. F. Besser, J. L. Logsdon: „Abrasive wear behavior of Al–Cu–Fe quasicrystalline composite coatings", *Materials Science and Engineering: A*", 1998.
- [4] A. A. Lapeshev, O. A. Bayukov, E. A. Rozhkova, I. V. Karpov, A. V. Ushakov, L. Y. Fedorov: „Modification of the phase composition and structure of the quasicrystalline Al-Cu-Fe alloy prepared by plasma spraying", *Physics of the Solid State*", 2015.
- [5] Bolelli, G., Bonferroni, B., Laurila, J., Lusvarghi, L., Milanti, A., Niemi, K., & Vuoristo, P. (2012). Micromechanical properties and sliding wear behaviour of HVOF-sprayed Fe-based alloy coatings. *Wear*, 276-277, 29-47.
- [6] Shi, P., Wan, S., Yi, G., Sun, H., Yu, Y., Xie, E., Wang, Q., Shen, S. Z., & Alam, N. (2020). TiO₂–ZnO/Ni–5wt.%Al composite coatings on GH4169 superalloys by atmospheric plasma spray techniques and their elevated-temperature tribological behavior. *Ceramics International*, 46(9), 13527-13538.
- [7] Lapeshev, A. A., E. A. Rozhkova, I. V. Karpov, A. V. Ushakov, and L. Yu. Fedorov. 2013a. “Physical, mechanical, and tribological properties of quasicrystalline Al-Cu-Fe coatings prepared by plasma spraying.” *Physics of the Solid State* 55 (12): 2531–36.
- [8] Jean-Marie Dubois, *The applied physics of quasicrystals*, *Physica Scripta* 1993(1993)T49A, IOP Publishing Ltd, p. 17-23

Microstructure evolution of boron-containing tool steel under rapid solidification conditions

H. Sohaib¹, A. Röttger¹, C. Sternemann²

¹Lehrstuhl Neue Fertigungstechnologien und Werkstoffe (FUW), Bergische Universität Wuppertal, 42651 Solingen, Germany

²Fakultät Physik/DELTA, Technische Universität Dortmund, 44221 Dortmund, Germany

Cold-work tool steels are renowned for their outstanding wear resistance and hardness, attributed to a martensitic matrix combined with hard carbide phases. These properties make them indispensable in mining, machining, and die manufacturing [1]. However, the growing demand for improved performance and cost efficiency has driven advancements in alloying and processing techniques, particularly through additive manufacturing (AM) methods like powder bed fusion-laser beam/metal (PBF-LB/M). The latter is a layer-by-layer AM technique that facilitates the fabrication of complex geometries, such as integrated cooling channels, while producing refined microstructures with fine grain sizes [2], making it ideal for high-performance tool steels. Boron-alloyed steels have emerged as promising candidates for these applications due to their ability to form hard phases, such as borides (Cr_2B , Fe_2B , M_3B_2) and carbo-borides ($\text{Fe}_3(\text{C},\text{B})$, $\text{M}_{23}(\text{C},\text{B})_6$) [3-5]. However, the solidification sequence during PBF-LB/M significantly differs between high and low solidification rates, influencing the size, morphology, and distribution of hard phases and residual stresses, affecting the materials' properties. The current research focuses on developing new martensitic, hardenable boron-alloyed tool steels using the Low Transformation Temperature (LTT) approach described by Röttger et al. [6] to counteract the formation of high residual stresses during PBF processing.

The Fe-C-B alloy system was further alloyed with Cr (6, 8, and 10 mass%) and Mo to investigate its solidification behavior under non-equilibrium conditions, as summarized in **Table 1**. Laser surface remelting of as-cast $10 \times 10 \times 5$ mm³ samples was conducted using an AconityMINI L-PBF machine in a vacuum environment. As shown in Table 2, two distinct remelting parameters were applied to each of the three alloys to evaluate variations in hard phase formation due to differing solidification rates and sequences. The remelting parameters, P1 and P2, resulted in cooling rates of approximately 2×10^6 K/s and 3.5×10^6 K/s, respectively, directly influencing the secondary dendrite arm spacing (SDAS). The SDAS, a key indicator of cooling conditions, was measured from dendritic micrographs. Its relationship to cooling conditions was analyzed using the empirical relation $\text{SDAS} = k \cdot t^m$, where k is a material-dependent constant (in $\mu\text{m} \cdot \text{s}^m$), t is the local solidification time, and m is an exponent typically ranging between 0.3 and 0.5. A high-energy synchrotron beam was used, capable of distinctly resolving phase peaks even in finer-grain microstructures with better resolution. The experiments were conducted at the DELTA synchrotron facility, beamline BL9, at TU Dortmund. High-energy X-rays (20 keV, wavelength = 0.61992 Å) with a beam size of 0.3×1.0 mm² were directed at the sample surfaces at a 5° incidence angle. The diffracted phases produced Debye-Scherrer rings, which were captured using a MAR345 detector and processed into 2D diffractograms using the open-source software Fit2D. The experimental setup was calibrated using a cerium oxide (CeO_2) reference sample, with adjustments made for detector-sample distance, detector tilt, and beam center.

Table 1: Chemical composition of the alloys in wt. %.

Alloy	C	B	Cr	Mo	Mn	Si	S	P	Fe
X50CrMoB6-2-1	0.53	1.13	5.70	2.14	0.5	0.52	0.03	0.028	Bal.
X50CrMoB8-2-1	0.49	1.14	7.57	2.19	0.5	0.54	0.03	0.028	Bal.
X50CrMoB10-2-1	0.51	1.18	9.22	2.13	0.53	0.53	0.03	0.030	Bal.

Table 2: PBF-process parameters for each alloy.

Sample parameters	Laser power [W]	Hatch distance [μm]	Scan speed [mm/s]	Energy density [J/mm^2]
P1	150	80	200	9.4
P2	150	80	400	4.7

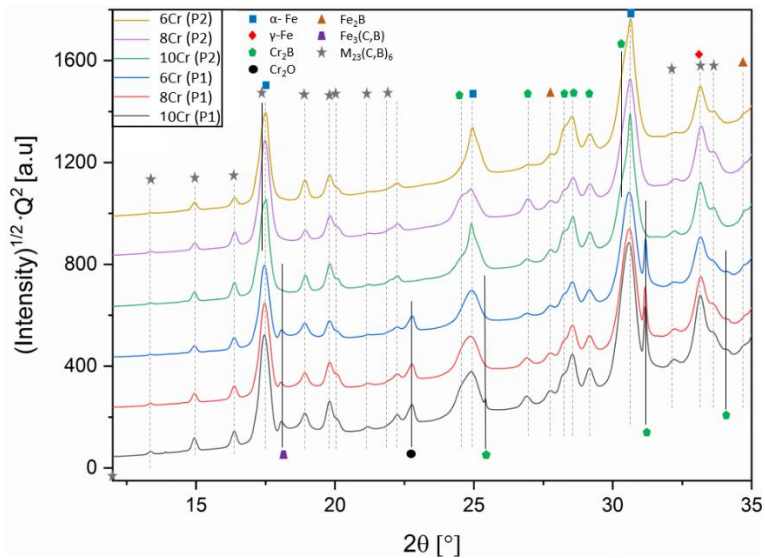


Figure 1: Synchrotron XRD diffraction peaks for the phases obtained under two different process parameters (P1 and P2) for each alloy: 6Cr, 8Cr, and 10Cr.

The differences in diffraction patterns are indicated by superimposed vertical solid lines. The broadness of the peaks is attributed to rapid solidification, which results in finer microstructures. At a 2θ angle of 14.46° , the peak corresponding to the $M_{23}(C,B)_6$ phase is observed prominently under the higher cooling rate condition (P2), while no boron-cementite is detected under these rapid solidification conditions. In contrast, boron-cementite appears under relatively lower cooling rates associated with P1 sample. Furthermore, in the latter, peaks corresponding to M_3B_2 , Cr_2B , and Cr_2O phases are distinctly visible, as indicated at the bottom of the diffractogram. The synchrotron XRD results aid in identifying the diffracted peaks corresponding to specific phases and provide detailed analysis of peak broadening in relation to different alloy compositions and processing conditions.

Acknowledgement: The authors sincerely thank the DELTA of TU Dortmund University for providing access to synchrotron radiation and offering support throughout the experiments conducted at beamline BL9.

References

- [1] J. Lentz, A. Röttger, and W. Theisen, "Solidification and phase formation of alloys in the hypoeutectic region of the Fe–C–B system," *Acta Materialia*, vol. 99, pp. 119–129, 2015.
- [2] T. DebRoy, H. L. Wei, J. S. Zuback, T. Mukherjee, J. W. Elmer, J. O. Milewski, *et al.*, "Additive manufacturing of metallic components – Process, structure and properties," *Progress in Materials Science*, vol. 92, pp. 112–224, 2018.
- [3] J. Lentz, A. Röttger, and W. Theisen, "Enhancement of hardness, modulus and fracture toughness of the tetragonal $(Fe,Cr)_2B$ and orthorhombic $(Cr,Fe)_2B$ phases with addition of Cr," *Materials & Design*, vol. 156, pp. 113–122, 2018.
- [4] J. Lentz, A. Röttger, and W. Theisen, "Hardness and modulus of Fe_2B , $Fe_3(C,B)$ and $Fe_{23}(C,B)_6$ borides and carboborides," *Materials Characterization*, vol. 135, pp. 192–202, 2018.
- [5] S. Ma, W. Pan, J. Xing, S. Guo, H. Fu, and P. Lyu, "Microstructure and hardening behavior of Al-modified Fe-1.5 wt% B-0.4 wt. % C high-speed steel during heat treatment," *Mater. Charact.*, vol. 132, pp. 1–9, 2017.
- [6] A. Röttger, J. Boes, F. Großwendt, and S. Weber, "Description of a new concept for the development of adapted hot-work tool steels for laser-powder bed fusion," *Additive Manufacturing*, vol. 61, Art. no. 103292, ISSN: 2214-8604, 2023.

The synchrotron XRD diffractogram of the PBF-remelted surfaces is shown in Figure 1, highlighting phase differences due to the distinct remelting parameters in terms of diffracted peaks. This study provides valuable insights into how cooling rates influence microstructural evolution during the rapid solidification of Fe-C-B-based alloys, particularly the formation of submicron-sized hard phases. In the diffractogram, further enhancement of the peaks at higher 2θ angles was performed in reciprocal space using the transformation $(\text{intensity})^{1/2} \cdot Q^2$.

Crystallographic analysis of arc-evaporated TiAlN thin films produced from differently manufactured cathode materials

Finn Rümenapf^{a,*}, Nelson Filipe Lopes Dias^a, Dominic Stangier^b, Nils Denkmann^c,
Alexander Meijer^d, Simon Jaquet^d, Rafael Garcia Carballo^d, Jörg Debus^c, Dirk Biermann^d,
Wolfgang Tillmann^a

^aInstitute of Materials Engineering, TU Dortmund University, Leonhard-Euler-Straße 2, 44227 Dortmund, Germany

^bOerlikon Balzers Coating Germany GmbH, Am Böttcherberg 30-38, 51427 Bergisch Gladbach, Germany

^cExperimental Physics 2, TU Dortmund University, Otto-Hahn-Straße 4a, 44227 Dortmund, Germany

^dInstitute of Machining Technology, TU Dortmund University, Baroper Straße 303, 44227 Dortmund, Germany

*corresponding author: finn.ruemenapf@tu-dortmund.de

Titanium aluminum nitride (TiAlN) thin films are widely used as wear protective thin films in cutting applications due to their high hardness, wear resistance, and thermal stability [1,2]. In the cathodic arc evaporation process, TiAl cathodes can be produced by either smelting metallurgical (SM) or powder metallurgical (PM) methods, which significantly influence the cathode microstructure and thereby the droplet emission, and resulting thin film properties [3,4]. Studies have shown differences in hardness, oxidation resistance, and plasma composition based on cathode type, with transformation processes at the cathode surface during arc discharge creating new phases such as Ti₃Al [5,6]. In addition to the cathode material, the deposition pressure shows an influence on the crystalline growth, where higher pressures lead to a compound layer on the cathode surface with a higher melting point, reducing droplet size and density in the thin film [7,8]. However, the interaction effects of cathode materials and deposition parameters on the crystallographic structure of TiAlN remain insufficiently explored. High-resolution XRD measurements can be applied to understand these effects. These measurements are fundamental for the understanding of the crystallographic structure of TiAlN thin films and their correlation to the tribo-mechanical properties.

TiAlN thin films were deposited using a customized METAPLAS.DOMINO kila flex PVD coater (Oerlikon Balzers, Germany) using different Ti₅₀Al₅₀ cathode materials (values in at.%): one produced via smelting metallurgical (SM) and two via powder metallurgical (PM) methods, labeled PM1 and PM2. SEM micrographs of the cathode materials before use revealed dense, defect-free structures across all manufacturing methods. Deposition was conducted at nitrogen-regulated pressures of 3000, 5000, and 8500 mPa. To determine the phase composition of the thin films, high-resolution XRD measurements were performed at the DELTA using 20 keV photons, a 2° incidence angle, and a MAR345 detector. Additionally, residual stresses were evaluated using a laboratory diffractometer via the $\sin^2\Psi$ method on the (111) TiAlN reflection, assuming isotropic stress.

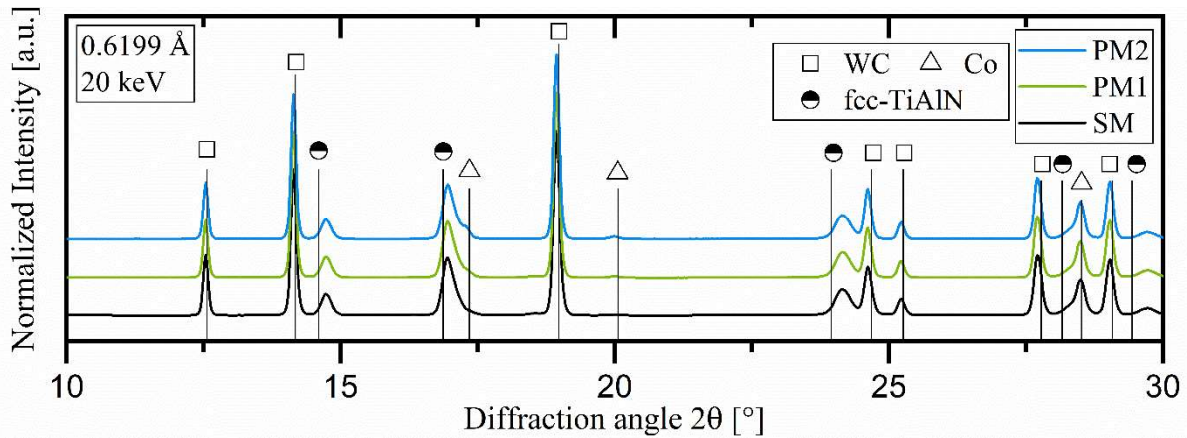


Figure 1: High resolution XRD patterns of the TiAlN thin films arc evaporated from differently manufactured TiAl cathodes at a deposition pressure of 8500 mPa

Figure 1 presents the integrated high-resolution XRD patterns of exemplary chosen arc-evaporated TiAlN thin films deposited at a deposition pressure of 8500 mPa, while the patterns are similar for the other deposition pressure values. The Bragg reflections corresponding to the WC and Co phases of the substrate are clearly visible due to the high penetration depth of the 20 keV X-rays, even at the low incidence angle of 2° . All analyzed thin films exhibit the fcc-TiAlN phase, consistent with the Al/Ti ratio of around 0.8 [9,10]. The Bragg angle intensities and widths remain constant, and no additional phases are detected for the different TiAlN thin films deposited at the different deposition pressures. This indicates that neither the cathode manufacturing method nor the deposition pressure significantly influence the crystallographic structure or phase composition of the deposited thin films. Residual stresses were evaluated using the (111) TiAlN plane and the $\sin^2\Psi$ method, revealing a compressive stress state in all arc-evaporated TiAlN thin films. The residual stresses exceed 3 GPa, with standard deviations ranging from 0.1 to 0.2 GPa. The cathode material had no notable impact on the residual stress state. For films deposited using the SM cathodes, a slight increase in absolute residual stress values was observed with higher deposition pressure reaching around 3.8 ± 0.2 GPa. In contrast, thin films produced with the PM cathodes showed consistent stress values around 3.6 ± 0.2 GPa at deposition pressures of 5000 mPa or higher. These variations, however, remain within the standard deviation of the XRD measurements and are therefore not considered significant.

The results of the crystallographic structure analyzed by high resolution XRD are correlating with the mechanical properties of the thin films, revealing no significant differences in hardness or elastic modulus across cathode materials or chamber pressures. However, process-related variations in surface quality of TiAlN were observed due to differences in droplet formation. In conclusion, high

resolution XRD analyses provides a comprehensive understanding on the structural properties of TiAlN thin film and allows to determine correlations with the mechanical properties.

Acknowledgments: The authors gratefully acknowledge the financial support by the Deutsche Forschungsgemeinschaft (DFG, German Research Foundation) in the framework of the priority program SPP2402 “*Greybox models for the qualification of coated tools for high-performance cutting*” in the subproject 521382051. In addition, the authors thank the DELTA for providing synchrotron radiation and for the technical support at beamline BL9 during the X-ray diffraction.

Presentation to a scientific audience: The study entitled “*Influence of TiAl cathode material manufacturing route on the structural and tribo-mechanical properties of arc-evaporated TiAlN thin films*” included the previously shown results and was presented as a poster at the 50th International Conference on Metallurgical Coatings & Thin Films, which took place on May 19-24, 2024 in San Diego.

References

- [1] V.F.C. Sousa, F.J.G. Da Silva, G.F. Pinto, A. Baptista, R. Alexandre, Characteristics and Wear Mechanisms of TiAlN-Based Coatings for Machining Applications: A Comprehensive Review, *Metals* 11 (2021) 260. <https://doi.org/10.3390/met11020260>.
- [2] P. Jindal, A. Santhanam, U. Schleinkofer, A. Shuster, Performance of PVD TiN, TiCN, and TiAlN coated cemented carbide tools in turning, *International Journal of Refractory Metals and Hard Materials* 17 (1999) 163–170. [https://doi.org/10.1016/S0263-4368\(99\)00008-6](https://doi.org/10.1016/S0263-4368(99)00008-6).
- [3] A. Kimura, T. Murakami, K. Yamada, T. Suzuki, Hot-pressed Ti-Al targets for synthesizing Ti_{1-x}Al_xN films by the arc ion plating method, *Thin Solid Films* 382 (2001) 101–105. [https://doi.org/10.1016/S0040-6090\(00\)01692-8](https://doi.org/10.1016/S0040-6090(00)01692-8).
- [4] S. PalDey, S. Deevi, Single layer and multilayer wear resistant coatings of (Ti,Al)N: a review, *Materials Science and Engineering: A* 342 (2003) 58–79. [https://doi.org/10.1016/S0921-5093\(02\)00259-9](https://doi.org/10.1016/S0921-5093(02)00259-9).
- [5] L. Chen, Y. Yang, M.J. Wu, Y.X. Xu, Y. Du, S. Kolozsvári, Correlation between arc evaporation of Ti–Al–N coatings and corresponding Ti_{0.50}Al_{0.50} target types, *Surface and Coatings Technology* 275 (2015) 309–315. <https://doi.org/10.1016/j.surfcoat.2015.04.048>.
- [6] I. Zhirkov, A. Petruhins, P. Polcik, S. Kolozsvári, J. Rosen, Effect of Ti-Al cathode grain size on plasma generation and thin film synthesis from a direct current vacuum arc plasma source, *AIP Advances* 9 (2019). <https://doi.org/10.1063/1.5092864>.
- [7] S.G. Harris, E.D. Doyle, Y.-C. Wong, P.R. Munroe, J.M. Cairney, J.M. Long, Reducing the macroparticle content of cathodic arc evaporated TiN coatings, *Surface and Coatings Technology* 183 (2004) 283–294. <https://doi.org/10.1016/j.surfcoat.2003.08.086>.
- [8] B. Warcholinski, A. Gilewicz, P. Myslinski, E. Dobruchowska, D. Murzynski, Structure and Properties of AlCrN Coatings Deposited Using Cathodic Arc Evaporation, *Coatings* 10 (2020) 793. <https://doi.org/10.3390/coatings10080793>.
- [9] M. Zhou, Y. Makino, M. Nose, K. Nogi, Phase transition and properties of Ti–Al–N thin films prepared by r.f.-plasma assisted magnetron sputtering, *Thin Solid Films* 339 (1999) 203–208. [https://doi.org/10.1016/S0040-6090\(98\)01364-9](https://doi.org/10.1016/S0040-6090(98)01364-9).
- [10] I. Endler, M. Höhn, M. Herrmann, R. Pitonak, S. Ruppi, M. Schneider, H. van den Berg, H. Westphal, Novel aluminum-rich Ti_{1-x}Al_xN coatings by LPCVD, *Surface and Coatings Technology* 203 (2008) 530–533. <https://doi.org/10.1016/j.surfcoat.2008.04.098>.

An X-ray diffraction study of copper powder for laser-based powder bed fusion

E. Schneider¹, R. Ortmann³, J. Savelkoul¹, L. Friedrich¹, J. Frank², F. Hellwig²,
M. Blüm², M. Paulus¹, A. Röttger², J.T. Sehr³, C. Sternemann¹

¹Fakultät Physik/DELTA, Technische Universität Dortmund, 44221 Dortmund, Germany

²Lehrstuhl Neue Fertigungstechnologien und Werkstoffe (FUW), Bergische Universität Wuppertal, 42651 Solingen, Germany

³Lehrstuhl Hybrid Additive Manufacturing (HAM), Ruhr-Universität Bochum, 44801 Bochum, Germany

Additive manufacturing (AM) of components using laser-based powder bed fusion of metals (PBF-LB/M) enables the production of e.g. aerospace components using Inconel 718 [1], medical devices from Ti6Al4V [2], and improved antennas, or heat exchangers made of copper [3]. This layer-by-layer process offers significant advantages over casting, shaping, and subtractive methods, particularly for machining complex parts with internal cavities. One promising application of PBF-LB/M is the creation of topology-optimized lightweight structures. Ongoing research seeks to extend the range of metals and alloys applicable to this technology.

The use of copper powders in PBF-LB/M poses distinct challenges due to copper's high thermal conductivity and reflectivity, especially to the commonly used 1070 nm and 1064 nm wavelength infrared lasers. These properties limit the efficient absorption of laser energy, affecting the process stability and reliability. Directed oxidation and reduction of copper particle surfaces present a potential solution for pre-conditioning, enhancing both the processability and reusability of copper powders.

In this study, we investigate the oxidation of pre-treated copper powders in air and their controlled reduction under an Ar/2%H₂ atmosphere at varying temperatures up to 350 °C. The experiments were conducted using X-ray diffraction at beamline BL9 of the DELTA synchrotron radiation source to gather insights into induction times and changes in the phase composition of Cu, Cu₂O, and CuO. This approach aims to constrain the reaction conditions for industrial processing by characterizing the composition of the crystalline oxide layers of the powder particles ex-situ and in operando, providing valuable data on the atomic structural level and thus potentially contributing to the broader applicability of copper in AM.

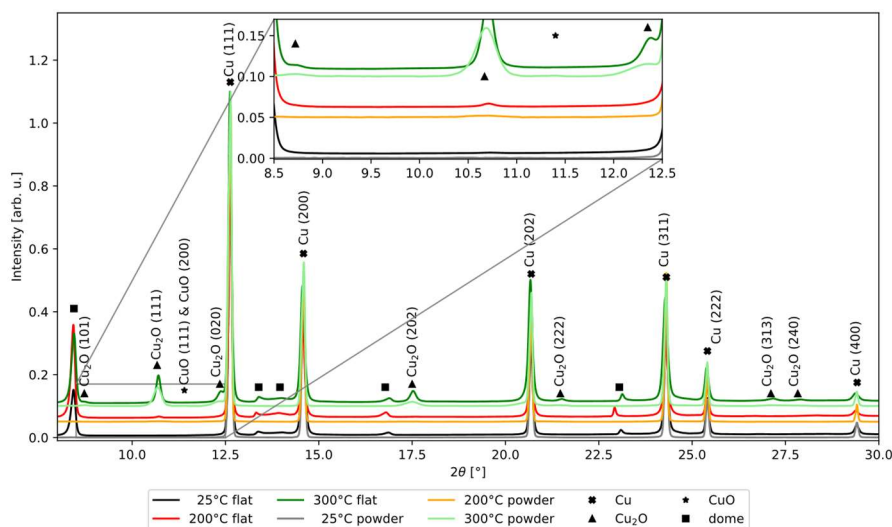


Figure 1: Diffractograms of the copper powders compared with the printed flat samples heated up to 300 °C.

Pure Cu-powder has been produced by atomizing from pure Cu wire (grade CW008A, Haecker Metall, Germany) using an atomizer ATOlabs (3Dlabs, Poland). Afterwards the powder particles were sieved to obtain a particle size

distribution between 20 μm – 63 μm . To enhance comprehension of the pre-oxidation process, samples of the powder were annealed in an muffle furnace in air to study the effect of temperature and time on the samples' oxide content and type of oxide formed, i.e. Cu_2O and CuO . Powder samples were enclosed in capillaries and mounted on the sample rotation unit for powder diffraction at beamline BL9. The X-rays had an energy of 27 keV and the beam size was 1 x 1 mm^2 . The scattered intensity was detected with a MAR345 image plate detector.

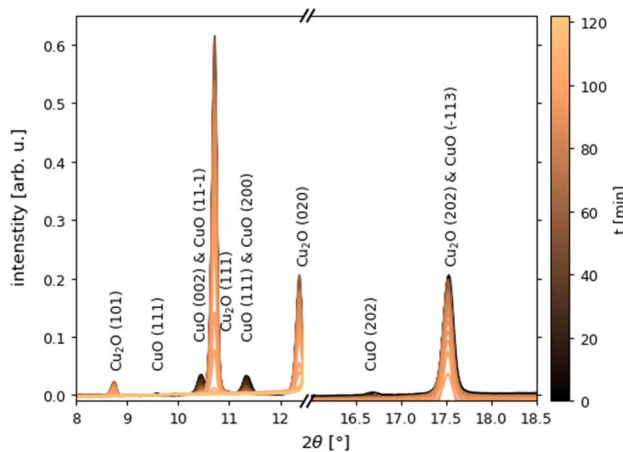


Figure 2: Diffraction patterns of a reduction series of pre-oxidised copper powder in an Ar/2% H_2 atmosphere.

Figure 1 compares the diffraction patterns of the native Cu powder and the annealed powders at 200 $^{\circ}\text{C}$ and 300 $^{\circ}\text{C}$. It also shows the Copper oxide phases of the printed samples using the PBF-LB/M process. It is noticeable that the printed samples do not form CuO . The additional peak above 8 degrees results from scattering from the graphite dome of the Anton Paar cell which was used to adjust the reaction atmosphere during heating.

In order to gain a better understanding of the oxidation and reduction behavior of the copper powders, the partially pre-oxidized powders

were both reduced and oxidized (in operando) at beamline BL9 while taking diffraction patterns. For these measurements, the powders were filled into borosilicate capillaries with a diameter of 1.5 mm. The capillaries were filled with glass wool before and after the powder to allow the gas to flow through and to keep the sample at place, during taking pre-vacuum and streaming with the gas. At the beginning of the series of measurements, the lower end of the capillary was cut off so that the gas can still reach the sample from both sides.

After evacuating and filling the sample cell with the reducing gas Ar/2% H_2 , the sample was heated up to 350 $^{\circ}\text{C}$ and exposed in 138-second intervals (30 s detection + 108 s detector readout) until the sample was completely reduced. We studied various reduction temperatures and gas flows to reveal the phase composition of the oxides Cu_2O and CuO and its change with time. The data is currently analyzed and the measurements will be complemented by further experiments using better defined gas flow rates.

References

- [1] X. Wang, et al: Review on powder-bed laser additive manufacturing of Inconel 718 parts, Proceedings of the Institution of Mechanical Engineers, Part B: J. of Eng. Manuf., 231 (2016) 11, S. 1890-1903
- [2] E. Mahmoud, et al: Optimization of SLM process parameters for Ti6Al4V medical implants, Rapid Prototyping Journal, 25 (2019) 3, pp. 433-447
- [3] T. Romano, M. Vedani: Additive Manufacturing of Pure Copper: Technologies and Applications, in: Copper - From the Mineral to the Final Application, IntechOpen, 2022, DOI: 10.5772/intechopen.107233

Acknowledgments

We thank the DELTA team for providing synchrotron radiation. This work was supported by the DFG via projects STE 1079/9-1, RO 4523/9-1, SE 2935/6-1

Hard X-ray spectroscopy

An X-ray absorption near edge spectroscopy study on AlCrVY(O)N thin films

Eric Schneider¹, Finn Rügenapf², Jaqueline Savelkouls¹, Christian Sternemann¹, Michael Paulus¹, Nelson Filipe Lopes Dias², Dirk Lützenkirchen-Hecht³, Wolfgang Tillmann²

¹Fakultät Physik/DELTA, Technische Universität Dortmund, 44221 Dortmund, Germany

²Fakultät Maschinenbau, Institute of Materials Engineering, TU Dortmund University, 44221 Dortmund, Germany

³Fakultät für Mathematik und Naturwissenschaften, Fachgruppe Physik, University of Wuppertal, 42119 Wuppertal, Germany

Great efforts are being made to optimize tool coatings for use at elevated process temperatures. This aims to enable machining with minimal lubrication. During operation, temperatures between 300 °C and 1000 °C can occur. To enable the machining of high-strength materials, the coatings must be optimized for their temperature resistance, which is significantly affected by their oxidation properties. AlCrVY(O)N thin films are potential candidates for such coatings, as the addition of V to AlCrN promotes the formation of Magnéli phases at high temperatures, which promote a reduction in friction due to their crystallographic structure. The oxidation behavior of V in the thin films is characterized using X-ray absorption near edge spectroscopy (XANES) at beamline BL10 [1] as well as X-ray diffraction (XRD) measurements at beamline BL9 of DELTA.

The AlCrVY(O)N thin films were deposited on WC-Co substrates. The coating process was performed using an industrial magnetron sputtering system with Al₅₂Cr₃₀V_{16.5}Y_{1.5} targets (values in at.%). Oxygen and nitrogen gas flow rates were individually controlled, with oxygen varied between 0 and 20 sccm, while nitrogen was maintained at 130 sccm. Argon served as the ionization gas during deposition. For AlCrVYON thin films with varying vanadium contents, the cathode power of the cathode equipped with a vanadium target was varied between 0.5 kW and 4.5 kW. A detailed description of the deposition process is given in [2].

In order to investigate the oxidation behavior of the thin films at machining-related temperatures, the AlCrVY(O)N thin films were heated stepwise up to 1000 °C using an SR 100-750/11 tube furnace (Carbolite Gero GmbH & Co. KG, Germany). The XANES measurements of the vanadium K-edge (5465 eV) were performed in fluorescence detection mode using a grazing angle of 3°, to identify the different oxidation states of vanadium in the thin film. In this setup we used a beam size of 0.2 x 8.0 mm² (v x h). For XRD experiments we used a photon energy of 27 keV and a beam size of 0.1 x 0.8 mm² (v x h) the grazing angle was 4°. The scattered intensity was detected by a MAR345 image plate detector.

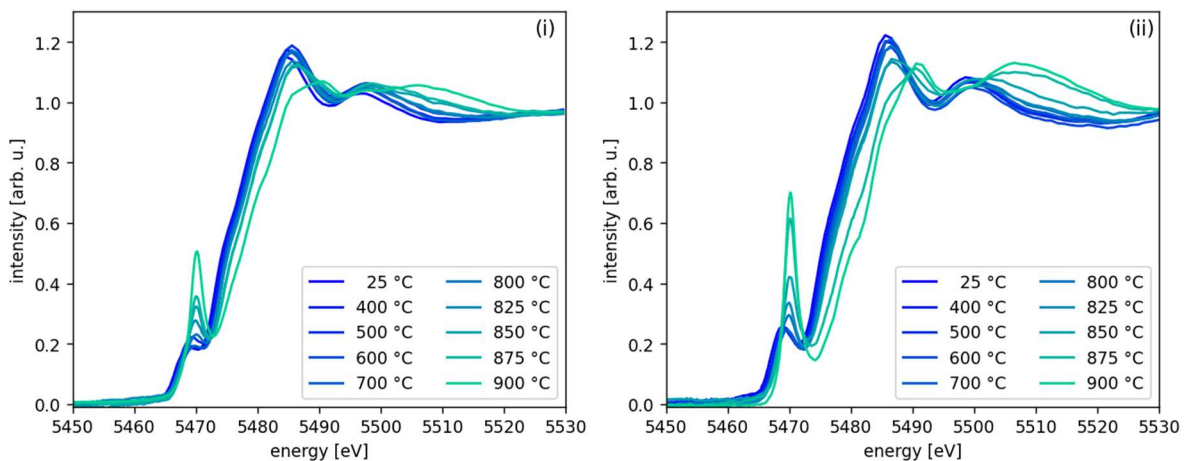


Figure 1: i) XANES spectra of AlCrVYON thin film annealed in ambient atmosphere for the sample pre-oxidized at O₂ flow of 5 sccm for 10 min and the indicated temperatures. ii) XANES spectra of AlCrVYON thin film annealed in ambient atmosphere for the sample pre-oxidized at O₂ flow of 20 sccm for 10 min and the indicated temperatures.

Due to the penetration depth of over 50 μm , the XRD data sets are dominated by WC, which is part of the substrate (data not shown). The next largest contribution comes from cubic AlCrVYN, which determines the structure of the 2.4 - 2.7 μm thick thin film [3]. The measured diffractograms show below 700 $^{\circ}\text{C}$ no Bragg reflexes that can be clearly assigned to vanadium oxides, while at higher temperatures a large number of reflections occur, suggesting increasing oxidation of the sample. However, due to the high number of possible phases formed, a clear assignment of the oxide phases is problematic. However, the occurrence of surface oxidation can be validated with the XANES measurements as shown in Figure 1. Via the analysis of the pre-edge peaks of the XANES vanadium K-edge spectra, the formation of vanadium oxides in thin films is investigated. Similar to iron oxides, the pre-edge area and main-edge position provide information about the average oxidation state of vanadium [3, 4]. Figure 1 shows the vanadium K-edge of samples produced with an O_2 flow rate up to 20 sccm. The oxidation state can be tracked by analyzing the area and center of gravity position of the pre-edge feature. The pre-edge of the as-deposited thin films becomes more pronounced with higher O_2 flow rates during synthesis. The main-edge position shifts to higher energies suggesting that the AlCrVYON thin films are pre-oxidized for the O_2 flow rates above 10 sccm with stronger variation in the local environment of V at 20 sccm as indicated by the changes in the post edge region.

To determine the average oxidation state of the thin films, the relationship between the area and energy position of the integrated pre-edge features need to be analyzed. All AlCrVY(O)N thin films, whether pre-oxidized or not, exhibit high oxidation resistance up to temperatures of 700–800 $^{\circ}\text{C}$. Above approximately 800 $^{\circ}\text{C}$, the vanadium in films with higher levels of pre-oxidation oxidizes more rapidly, leading to a higher average oxidation state at the maximum annealing temperature. These results indicate that the increased oxygen incorporation in AlCrVYON thin films accelerates the vanadium oxidation, particularly the formation of Magnéli phases.

References

- [1] D. Lützenkirchen-Hecht, R. Wagner, S. Szillat, A.K. Hüsecken, K. Istomin, U. Pietsch, R. Frahm, The multi-purpose hard X-ray beamline BL10 at the DELTA storage ring, *Journal of Synchrotron Radiation*, Volume 21, 2004, Pages 819-26.
- [2] W. Tillmann, F. Rümenapf, D. Aubry, E. Schneider, M. Paulus, C. Sternemann, N. F. Lopes Dias, Structural and tribo-mechanical properties of AlCrVYON thin films with varying O contents sputtered from either AlCrVY or AlCrY and V targets, *Surface and Coatings Technology*, Volume 497, 2025.
- [3] E. Schneider, F. Ontrup, G. Scholz, J. Savelkouls, N. F. Lopes Dias, C. Sternemann, D. Lützenkirchen-Hecht, W. Tillmann, M. Paulus, "Oxidation Behavior of Vanadium in Annealed AlCrVY(O)N Thin Films Characterized by X-ray Absorption Spectroscopy," *Physica Status Solidi (A)*, 2024.
- [4] M. Wilke, G. M. Partzsch, R. Bernhardt, D. Lattard, Determination of the iron oxidation state in basaltic glasses using XANES at the K-edge, *Chemical Geology*, Volume 213, Issues 1–3, 2004, Pages 71-87.

Acknowledgments

We thank the DELTA team for providing synchrotron radiation. This work was supported by the DFG via TO 169/21-1 and TI 343/190-1.

Hydrogen Economy vs. Hydrogen Embrittlement: Indirect Electrochemical Determination of Hydrogen Diffusion in Steel

Andreas Drichel^a, Madlin Spiewak^a, Arne Röttger^b, Dirk Lützenkirchen-Hecht^c,
Bruno V. Manzoli Rodrigues^{a,*} and Adam Slabon^{a,*}

^a Faculty of Mathematics and Natural Sciences: Inorganic Chemistry, University of Wuppertal, Gaußstraße 20, 42119 Wuppertal, Germany

^b Chair for New Manufacturing Technologies and Materials, University of Wuppertal, Bahnhofstraße 15, 42651 Solingen, Germany

^c Faculty of Mathematics and Natural Sciences: Condensed Matter and Experimental Solid-State Physics, University of Wuppertal, Gaußstraße 20, 42119 Wuppertal, Germany

Hydrogen is in great demand as an alternative energy source for a sustainable economy. However, the problem arises during long-term storage and transportation, as hydrogen diffuses through the containers and the material becomes brittle. For this reason, it is important to be able to investigate the diffusion processes of hydrogen in metals (here: stainless steel types) and the resulting embrittlement of the material. Structural investigations are thus of utmost importance to understand the processes. In particular, EXAFS measurements appear useful due to their inherent sensitivity towards small changes of the local atomic environment of the involved metals.

The results can be used to indirectly deduce hydrogen damage to the metal lattice, as the positions of the metal atoms may change significantly due to a hydrogen treatment. Here we have demonstrated the hydrogen-induced embrittlement in stainless steel by performing EXAFS/XANES fluorescence measurements.

Extended X-ray absorption fine structure (EXAFS) experiments were carried out at the materials science beamline 10 [1] at the DELTA storage ring (TU Dortmund / Germany) operating with 1.5 GeV electrons and a stored current of 100–140 mA¹ (Range: 4–14 keV). A Si (111) channel-cut monochromator was employed, and the intensity of the incident beam on the sample was measured using a nitrogen-gas filled ionization chamber, while the X-ray fluorescence from the sample was collected using a large-area PIPS[®] photodiode (Passivated Implanted Planar Silicon). The energy range measured covered the X-ray absorption edges of Cr (5989 eV), Mn (6539 eV), Fe (7112 eV), Ni (8333 eV) and Cu (8980 eV). Fluorescence mode EXAFS data were collected on the fly in the quick-scanning EXAFS mode. Background subtracted, normalized EXAFS data of the duplex steel sample 1.4501 obtained at the Fe and Cr K-edges after hydrogen permeation tests are depicted in Figure 1

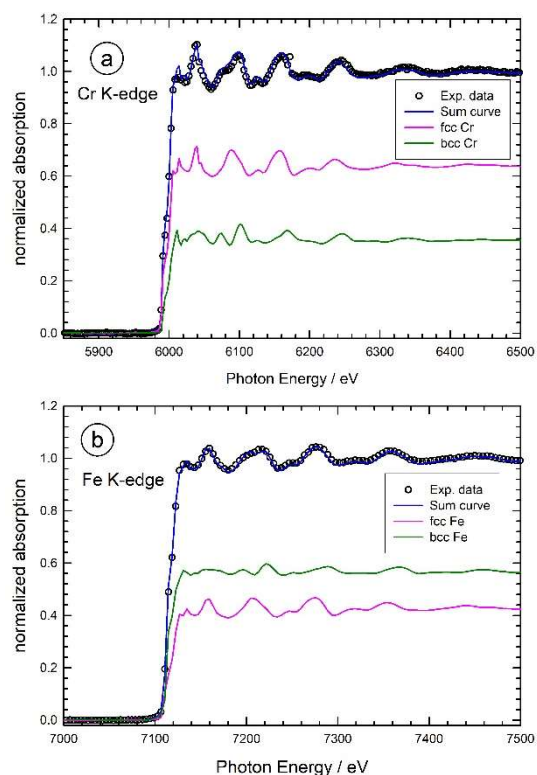


Figure 1. Linear-combination fits of the normalized X-ray absorption spectra measured at the Cr K-edge (a) and the Fe K-edge (b) of the 1.4501 duplex steel. EXAFS measurement were performed on samples after hydrogen permeation tests.

as examples. From the edge height in the raw data, the concentration of the respective elements has been calculated. For the further data evaluation, the data at the Cr and Fe K-edge were fitted with linear combinations of standard spectra for the austenite (face-centered cubic, fcc) and ferrite (body-centered cubic, bcc) phases, obtained from purely bcc Cr and Fe metal foils, and a purely fcc steel containing Cr, Fe, and Ni. As depicted in Figure 1, the spectra measured at the Cr and Fe K-edges can be well-fitted with linear combinations of these reference materials, indicating that the duplex steel indeed is comprised of both phases in nearly equal proportions of about 50%.

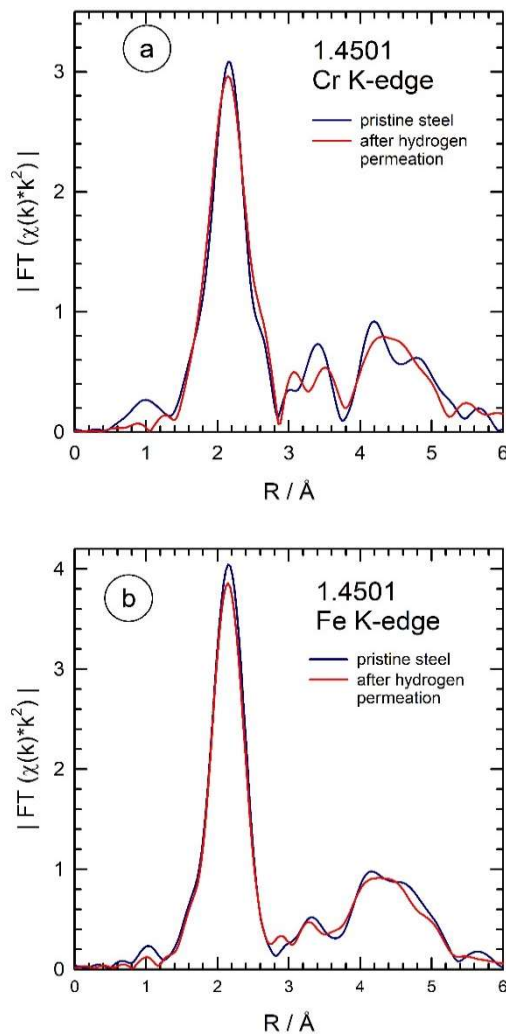


Figure 2. Comparison of the magnitude of the Fourier-transform of the k^2 -weighted EXAFS fine structures obtained at the Cr (a) and Fe (b) K-edges of 1.4501 duplex steel prior and after the hydrogen permeation test. Obviously, the amplitudes of all coordination decrease in intensity, while the positions remain unchanged.

It is important to note that the contributions of bcc and fcc phases remain unchanged before and after the hydrogen permeation tests, suggesting that no new phases are formed during the hydrogen treatment. However, a careful inspection of the Fourier-transforms (FT) of the $\chi(k) \cdot k^2$ data before and after hydrogen permeation reveals that the amplitudes of all the coordinations visible in the FT decrease after the permeation testing, as depicted in Figure 2, indicating an increase of disorder on an atomic level.

These results are of particular interest for the transformation toward a hydrogen economy, which will rely heavily both on i) predictable long-term stability of storage materials and ii) minimization of hydrogen loss, *i.e.* leakage, through the storage vessel.

Acknowledgements

We would like to thank the University of Dortmund for the measuring time at the DELTA-Synchrotron.

References

- (1) Lützenkirchen-Hecht, D.; Wagner, R.; Szillat, S.; Hüsecken, A. K.; Istomin, K.; Pietsch, U.; Frahm, R. The multi-purpose hard X-ray beamline BL10 at the DELTA storage ring. *J. Synchrotron Rad.* 2014, *21*, 819–826.

Revealing the metal coordination environment of solvent-free synthesised MOF glasses by X-ray absorption fine structure analysis

Wen-Long Xue, Sebastian Henke*

Anorganische Materialchemie – TU Dortmund, Otto-Hahn-Str. 6, 44227 Dortmund

Scientific context

Metal-organic framework (MOF) glasses, represented by zeolitic imidazolate framework (ZIF) glasses^[1], are a class of materials that possess random porous network structures and intriguing physicochemical properties. They offer a unique combination of functional porosity found in framework materials like conventional crystalline MOFs or zeolites, as well as properties from polymers, such as mouldability and processability.^[2] This combination of properties makes MOF glasses promising candidates for various applications, including gas separation, optoelectronics, and solid electrolytes. However, the established processes for preparing MOF glasses involve several costly and time-consuming steps that make it impractical for real-world industrial production. MOF glass preparation typically starts with the solution synthesis of MOF (micro)crystals under solvothermal conditions. Besides the high temperatures and reaction times, large amounts of hazardous organic solvents are also required. Afterwards, the derived MOF (micro)crystals are heated to their melting point and melt-quenched to obtain the MOF glasses. Recently, a mechanochemical method for the direct synthesis of MOF microcrystals and glass powders has been reported.^[3] However, this method still depends on the subsequent energy-intensive process of heating and (re)melting the powders in order to get homogeneous bulk glasses at a large scale. Thus, the commercialisation and practical use of MOF glasses require simpler and more environmentally friendly synthetic routes, as is the case with the commercialisation needs of other inorganic glass materials.

We developed a new solvent-free strategy for the **direct synthesis** of MOF glasses by mixing metal oxides and imidazole ligands followed by heating them directly to slightly above the ligand melting point. The amorphous nature of the **directly synthesized MOF glasses** (DSG-1) was verified by powder X-ray diffraction (PXRD). Moreover, differential scanning calorimetry (DSC) proves the glassy nature of the materials by the presence of a glass transition signal at $T_g \sim 170$ °C, which is the lowest glass transition temperature of any ZIF glass reported so far

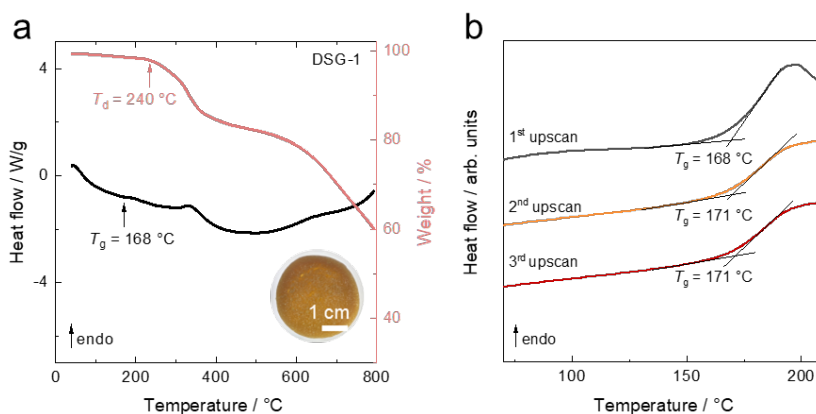


Fig. 1. **a** Simultaneous TGA and DSC data of DSG-1. The inset shows a photograph of a monolith of the DSG-1. **b** DSC data of DSG-1 with three upscans features a stable T_g of ~ 170 °C.

(Fig. 1). The new solvent-free direct synthesis strategy is pivotal for advancing the field of MOF glasses, providing a foundation for large-scale production, diversification, and the creation of composite materials, leading to innovative glass materials surpassing the current state of the art.

To unravel the Zn coordination environments in the DSG, we performed X-ray absorption spectroscopy (XAS) at BL10 of DELTA to resolve their extended X-ray absorption fine structure (EXAFS) for the directly synthesised Zn-based ZIF glass materials.

Experimental procedure

Powdered samples were carefully loaded into borosilicate capillaries with a 1.0 mm diameter. The samples were measured at room temperature at the Zn K-edge using X-ray absorption spectroscopy (XAS). Data collection was performed over a total scan time of 30 minutes per sample to ensure a high signal-to-noise ratio. Normalisation and background subtraction of the raw XAS spectra were conducted using the *Athena* software from the *Demeter* package. For validation and interpretation of the structural features, zinc foil and ZnO were used as reference compounds.

Results

The X-ray absorption near edge structure (XANES) of DSG-1 at the Zn K-edge closely resembles that of ZnO, particularly at the edge energy (**Fig. 2a**). This similarity indicates that the zinc ions in DSG-1 exhibit the oxidation state +II, as expected for Zn^{2+} ions. Further analysis through Fourier transformation reveals significant differences in the local coordination environment (**Fig. 2b-c**). In the Fourier-transformed EXAFS (the real-space radial distribution function), DSG-1 exhibits only one distinct Zn–N correlation signal at 1.53 Å (phase shift not corrected), with no evidence of residual ZnO in the glass sample. This observation strongly indicates that Zn^{2+} in DSG-1 is primarily coordinated with nitrogen atoms from the imidazolate linkers.

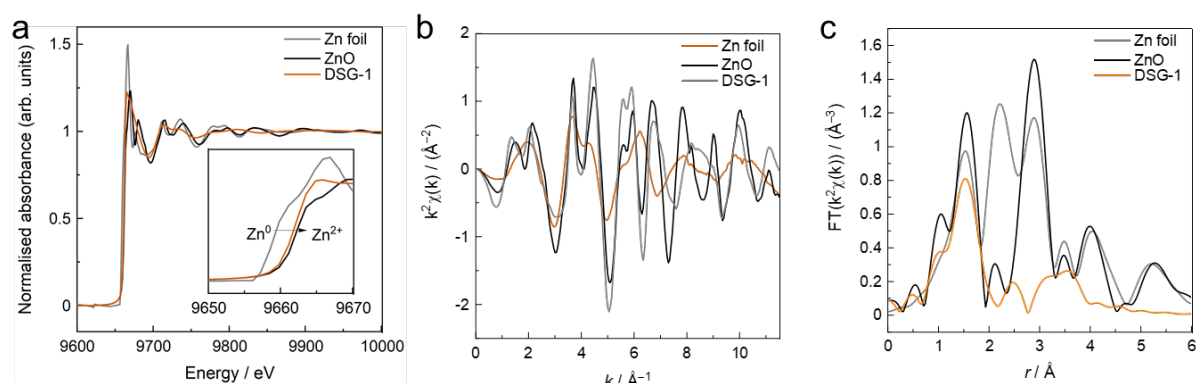


Fig. 2. (a) Normalised XAS spectra at the Zn K-edge for DSG-1, ZnO, and Zn foil. (b) k^2 -weighted EXAFS oscillations extracted from the XAS spectra. (c) Fourier-transformed EXAFS giving the radial distribution function (phase shift not corrected).

These findings demonstrate that DSG-1 shares similar structural characteristics with conventional ZIF glasses derived by melting of solvothermally synthesised microcrystals. The direct solvent-free synthesis results in a well-defined Zn–N

coordination environment that is part of a disordered random glass network. This newly developed direct synthesis method retains the key structural motifs typical of this class of ZIF glass materials while eliminating the need for intermediate crystallisation and melting processes.

In summary, BL10 enabled us to probe the local coordination environment of the novel directly synthesised glasses. Detailed analyses of the local coordination structure, including bond lengths and coordination numbers, are ongoing to deepen our understanding of these materials. Further investigations into their mechanical properties, such as hardness and elastic moduli, are planned to complement the structural insights and establish a comprehensive structure-property relationship.

The XAFS data collected during the beamtime will contribute to a manuscript currently under preparation for submission. We gratefully acknowledge the support of the DELTA team for providing beamtime and the invaluable assistance of the BL10 beamline scientists during the experiments.

References

- [1] a) T. D. Bennett et al., *J. Am. Chem. Soc.* **2016**, *138*, 3484; b) S. Horike, et al. *Angew. Chem. Int. Ed.* **2020**, *59*, 2.
- [2] a) L. Frenzel-Beyme et al., *J. Am. Chem. Soc.* **2019**, *141*, 12362–12371; b) L. Frenzel-Beyme et al., *Nat. Commun.* **2022**, *13*, 7750.
- [3] M. F. Thorne et al., *Chem. Commun.* **2021**, *57*, 9272-9275.

The structure of medium-entropy alloy nanoparticles as determined by EXAFS

T. Trompeter, D. Lützenkirchen-Hecht

Faculty of Mathematics and Natural Sciences-Physics Department, University of Wuppertal,
Gauss-Str. 20, D-42119 Wuppertal, Germany

By definition, a high-entropy alloy (HEA) consists of five or more elemental compounds, with an atomic concentration between 5 and 35 at.% for each of the constituting elements [1, 2]. A characteristic property of a high-entropy alloy is the mixed configuration entropy S_{mc} , given by

$$S_{mc} = -R \sum x_i \ln(x_i), \quad \text{eq. (1)}$$

with R the molar gas constant, and the x_i the molar fractions of each element (i) in the alloy. Accordingly, due to the large number of constituting elements and their large concentrations, S_{mc} of a HEA is substantially larger compared to that of a simple alloy, where several elements are present in very low concentration, or an intermetallic compound, with only two or three elemental species [3, 4]. Assuming the presence of five elements in equimolar concentrations, equation (1) reduces to $S_{mc} = R \ln(5) \approx 1.5 R$; i.e. an alloy can be considered as a high-entropy alloy if $S_{mc} \geq 1.5R$, and alloys with a smaller value of S_{mc} between 1 and 1.5 are considered as medium entropy alloys [1, 2]. From a thermodynamical perspective, an increase of the mixed configuration entropy favors the formation of disordered single-phase solid solutions, and suppresses the presence of more fragile multielemental intermetallic compounds. Employing several different metallic elements with accordingly different atomic radii and a random site occupation causes local lattice distortions [5].

In this context, EXAFS, with its unique opportunity to investigate the local atomic short range order around each of the contributing (metallic) elements, allows to investigate HEAs and MEAs to a large details, since all of the K-edges of the transition metal elements (i.e., Ti to Zn) can be investigated in a straightforward manner. Here we have investigated a medium entropy alloy with contributions of Co, Ni and Cu with K-edge EXAFS measurements at the DELTA wiggler beamline 10 using a Si(111) monochromator and ionization chambers as detectors for the incident and transmitted X-ray intensities [6]. According to the raw data, the edge jumps at the three investigated edges are 1.8 for Co, 1.1 for Ni, and 1.1 for Cu, leading to slightly different concentrations of 45 % for Co, and 28 % for Ni and Cu, respectively, giving a mixed configuration entropy $S_{mc} \approx (1.07 \pm 0.01) R$ [7].

In Fig. 1, the magnitude of the Fourier-Transform of the k^3 -weighted EXAFS fine structures measured at the different edges are compared to the FT of a face-centered cubic Ni reference foil. As can be seen, the peaks related to the first few neighbors clearly resemble the fcc structure of the reference material, suggesting indeed the presence of face-centered cubic structures in the MEA.

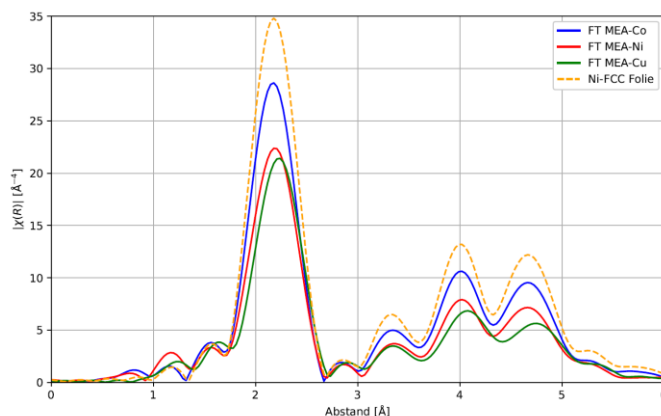


Fig. 1: Magnitude of the Fourier-Transform of the k^3 -weighted EXAFS fine structure oscillations $|\text{FT}(\chi(k) \cdot k^3)|$ from the high-entropy alloy at the Co, Ni and Cu K-edge. For comparison, the FT of a Ni metal reference foil is also shown.

We have therefore assumed a fcc-structure for the modelling of the EXAFS data of all edges, however with a random site occupation of Co, Ni and Cu. This way, disorder was taken into account, i.e., there is a certain probability for Co-Ni, Co-Cu and Co-Co nearest neighbor coordinations. From the k-range available from the experiment, and the radial distance range used for the fitting, the maximum number of fit variables N_{idp} can be estimated, resulting in values of about $N_{\text{idp}} \approx 20$. We have used a variation of the bond length in the first four shells (R_i), the (static and thermal) disorder (σ_i^2), individual amplitude reduction factors for each element (S_{oi}^2) and a global value for the inner potential shift ΔE_0 , so that in total only 12 fit parameters were used.

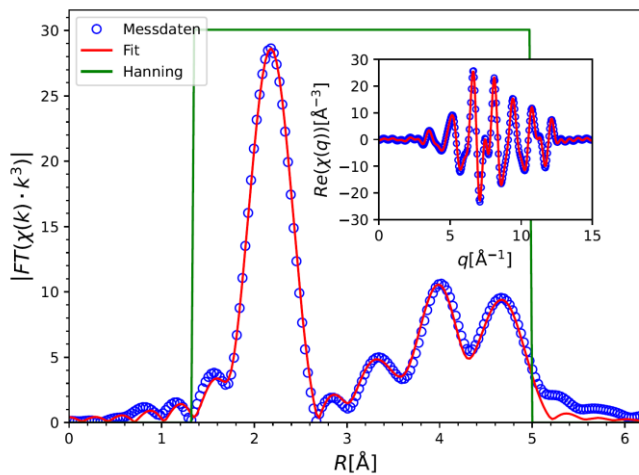


Fig. 2: Magnitude of the Fourier-Transform of the k^3 -weighted EXAFS fine structure oscillations $|FT(\chi(k) \cdot k^3)|$ at the Co K-edge, together with a fit assuming the presence of a fcc-structure, and Co, Ni and Cu randomly distributed on the regular lattice sites. A total number of 12 fit parameters was used, while $N_{\text{idp}} \approx 20$.

The results show, that the disorder parameters are substantially larger compared to the pure fcc metals Cu and Ni, with values around $(0.010 \pm 0.002) \text{ \AA}^2$ for the MEA compared to values well below 0.007 \AA^2 for the pure elements. Also the amplitude reduction factor reflects the larger disorder, with values of $S_o^2(\text{Co}) = 0.73 \pm 0.01$, $S_o^2(\text{Ni}) = 0.57 \pm 0.01$ and $S_o^2(\text{Cu}) = 0.56 \pm 0.02$, again reflecting the larger disorder around Ni and Cu, with smaller elemental concentration compared to Co. A more detailed publication of the EXAFS data analysis and the obtained fit results from the MEA and the HEA is currently in preparation.

Acknowledgements

We gratefully acknowledge the DELTA machine group for providing synchrotron radiation reliably.

References

- [1] D.B. Miracle, O.N.A. Senkov, *Acta Mater.* 122 (2017) 448.
- [2] W. Zhang, P.K. Liaw, Y. Zhang, *Sci. China Mater.* 61 (2018) 2.
- [3] J.W. Yeh, S.K. Chen, S.J. Lin, et al., *Adv. Eng. Mater.* 6 (2004) 299.
- [4] E.P. George, D. Raabe, R.O. Ritchie, *Nat. Rev. Mater.* 4 (2019) 515.
- [5] J.W. Yeh, *Ann. Chim. Sci. Mater.* 31 (2006) 633.
- [6] D. Lützenkirchen-Hecht, R. Wagner, S. Szillat, et al., *J. Synchrotron Rad.* 21 (2014) 819.
- [7] T. Trompeter, Bachelor's Thesis, University of Wuppertal, 2024.

XAS Investigations of a Dual Atom Iron Catalyst on Coffee Waste Biochar for Electrochemical Kraft Lignin Depolymerization

L. M. Lindenbeck,^a D. Lützenkirchen-Hecht,^b A. Drichel,^a B. B. Beele,^a B. V. M. Rodrigues,^a
A. Slabon^a

^a Chair of Inorganic Chemistry, Faculty of Mathematics and Natural Sciences, University of Wuppertal, Gaußstraße 20, 42119 Wuppertal, Germany

^b Department of Physics, Faculty of Mathematics and Natural Sciences, University of Wuppertal, Gaußstraße 20, 42119 Wuppertal, Germany

The electrochemical depolymerization of lignin represents a promising approach for the sustainable production of platform chemicals.¹⁻⁴ While advancements in single-atom catalysts (SACs) have demonstrated enhanced activity and selectivity for other applications (e.g., CO₂ reduction),⁵⁻⁷ dual atom catalysts (DACs) are emerging as superior alternatives due to their ability to synergistically activate multiple reaction intermediates.⁸ In this study, we investigated a Fe-based DAC supported on coffee waste biochar for lignin depolymerization. The objective was to examine the structural and electronic changes of the catalyst using *in-operando* and *ex-situ* X-ray absorption spectroscopy (XAS).

The extended X-ray absorption fine structure (EXAFS) spectra of the DAC catalyst before and after the reaction are displayed in **Figure 1A and 1B**, respectively. The Fourier-transformed spectra exhibit two dominant peaks at approximately 1.5 Å and 2.1 Å, corresponding to Fe-N (1.98 ± 0.03 Å) and Fe-Fe (2.58 ± 0.03 Å) bonds. Additionally, a weaker signal at 2.66 ± 0.05 Å is attributed to Fe-C interactions from the carbon matrix.

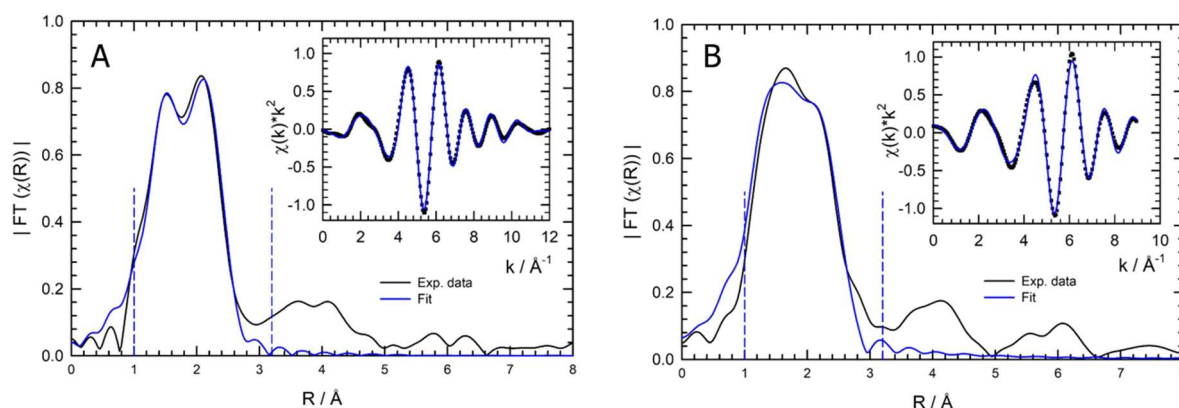


Figure 1. Coordination structure of DAC. **A** Fourier transform (FT) of the Fe K-edge EXAFS spectrum of DAC pre-reaction and corresponding fitting curve (k -range for the FT $1.3 \text{ \AA}^{-1} < k < 11.6 \text{ \AA}^{-1}$). The inset depicts the back-transformed data from $1.0 \text{ \AA} < R < 3.2 \text{ \AA}$ according to the dashed vertical lines. **B** Fourier transformation of the Fe K-edge EXAFS spectrum of DAC post-reaction and corresponding fitting curve, again the range from $1.0 \text{ \AA} < R < 3.2 \text{ \AA}$ was back-transformed into k -space and is depicted in the inset.

An analysis of the first-shell coordination numbers indicates a notable reduction in Fe-Fe interactions compared to metallic Fe, with an average coordination number of 1.6. This value is markedly lower than the expected eight neighbors in bulk Fe, indicating the absence of Fe clusters and supporting the dual atom Fe configuration. It is also noteworthy that no second-shell Fe-Fe interactions are observed, which serves to further confirm the di-atomic dispersion of the Fe centers.

Based on the EXAFS fitting results, a structural model of the catalyst was proposed. The N₂-Fe-Fe-N₂ motif, featuring dual atom Fe centers bridged by nitrogen from the doped biochar matrix, is consistent with the observed coordination numbers and bond distances.

After 20 hours of electrochemical lignin depolymerization, the EXAFS spectrum (**Figure 1B**) indicates the persistence of the N₂-Fe-Fe-N₂ motif, with negligible changes in bond distances or coordination numbers. These results demonstrate the structural stability of the catalyst under reaction conditions.

In-operando XAS measurements were performed to monitor the catalyst's stability during electrochemical lignin depolymerization at various potentials. The normalized Fe K-edge XAS spectra (**Figure 2A**) exhibit no detectable shifts in the edge position or changes in post-edge features across the applied potential range (−1.2 to −2.0 V vs. Ag/AgCl (satd. KCl)).

The first derivative of the XAS spectra (**Figure 2B**) and corresponding Gaussian fits (**Figure 2C**) reveal no significant edge energy shifts, confirming that the Fe oxidation state remains unchanged throughout the reaction. This stability is a key feature of the dual atom Fe catalyst, ensuring consistent catalytic performance under varying electrochemical conditions.

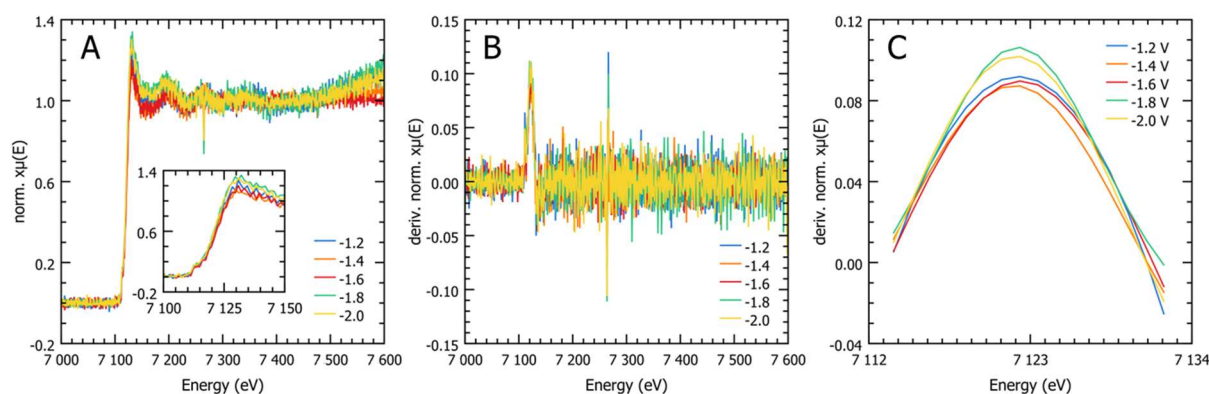


Figure 2. Stability of DAC. **A** Normalized Fe K-edge XAS spectra measured *in-operando* for different potentials as indicated. **B** First derivative of the normalized Fe K-edge XAS spectra. **C** Gaussian fit for the first derivative in the edge region (7112 eV < E < 7143 eV) of the normalized Fe K-edge XAS spectra. No systematic shift of the edge positive is observed.

A more detailed analysis of the characterization of the catalyst is currently under way and will be published in a forthcoming publication.

Acknowledgements

We gratefully acknowledge the DELTA machine group for providing synchrotron radiation reliably.

References

- (1) Da Cruz, M. G. A.; Gueret, R.; Chen, J.; Piątek, J.; Beele, B.; Sipponen, M. H.; Frauscher, M.; Budnyk, S.; Rodrigues, B. V. M.; Slabon, A. Electrochemical Depolymerization of Lignin in a Biomass-based Solvent. *ChemSusChem* **2022**, *15* (15), e202201246. <https://doi.org/10.1002/cssc.202201246>.
- (2) Lindenbeck, L. M.; Barra, V. C.; Dahlhaus, S.; Brand, S.; Wende, L.; Beele, B. B.; Schebb, Nils. H.; Rodrigues, B. V. M.; Slabon, A. Organic Chemicals from Wood: Selective Depolymerization and Dearomatization of Lignin via Aqueous Electrocatalysis. *ChemSusChem* **2024**, e202301617. <https://doi.org/10.1002/cssc.202301617>.
- (3) Lindenbeck, L. M.; Dahlhaus, S.; Wende, L. M.; Beele, B. B.; Frauscher, M.; Schebb, N. H.; Lehmann, C. W.; Bornhorst, J.; Slabon, A.; Rodrigues, B. V. M. Breaking down Lignin in Gamma-Valerolactone: Advances into a Bioelectrorefinery. *Green Chem. Lett. Rev.* **2024**, *17* (1), 2390867. <https://doi.org/10.1080/17518253.2024.2390867>.
- (4) Lindenbeck, L.; Brand, S.; Stallmann, F.; Barra, V.; Frauscher, M.; Beele, B. B.; Slabon, A.; Rodrigues, B. V. M. Silver-Catalyzed Aqueous Electrochemical Valorization of Soda Lignin into Aliphatics and Phenolics. *Polymers* **2024**, *16* (23). <https://doi.org/10.3390/polym16233325>.
- (5) Wang, W.; Li, S.; Qiang, Q.; Wu, K.; Pan, X.; Su, W.; Cai, J.; Shen, Z.; Yang, Y.; Li, C.; Zhang, T. Catalytic Refining Lignin-Derived Monomers: Seesaw Effect between Nanoparticle and Single-Atom Pt. *Angew. Chem. Int. Ed.* **2024**, e202404683. <https://doi.org/10.1002/anie.202404683>.
- (6) Lindenbeck, L. M.; Beele, B. B.; Lützenkirchen-Hecht, D. F.; Rodrigues, B. V. M.; Slabon, A. Electrochemical Biomass Depolymerization: Will Complex Catalysts Trigger High Product Selectivity? *Chem. Mater.* **2024**, *36* (19), 9173–9188. <https://doi.org/10.1021/acs.chemmater.4c02078>.
- (7) Chen, J.-Y.; Xiao, Y.; Guo, F.-S.; Li, K.-M.; Huang, Y.-B.; Lu, Q. Single-Atom Metal Catalysts for Catalytic Chemical Conversion of Biomass to Chemicals and Fuels. *ACS Catal.* **2024**, *14* (7), 5198–5226. <https://doi.org/10.1021/acscatal.4c00208>.
- (8) Zhao, S.; Liu, M.; Qu, Z.; Yan, Y.; Zhang, Z.; Yang, J.; He, S.; Xu, Z.; Zhu, Y.; Luo, L.; Hui, K. N.; Liu, M.; Zeng, J. Cascade Synthesis of Fe-N₂-Fe Dual-Atom Catalysts for Superior Oxygen Catalysis. *Angew. Chem. Int. Ed.* **2024**, e202408914. <https://doi.org/10.1002/anie.202408914>.

Laser-polishing of niobium in N₂-atmospheres: An EXAFS study

F. Brockner, D. Lützenkirchen-Hecht

Faculty of Mathematics and Natural Sciences-Physics Department, University of Wuppertal, Gauss-Str. 20, D-42119 Wuppertal, Germany

Superconducting niobium cavities, cooled to temperatures around 2 K, are widely used in modern particle accelerators and free-electron lasers. Due to the high acceleration gradients in the order of 30 MV/m, smooth and clean surfaces are required in the interior of the cavities, e.g., to avoid breakdown by parasitic electron field emission or other loss mechanisms [1,2]. Current treatments include buffered chemical etching in hydrofluoric acid and nitric acid [3], centrifugal barrier polishing and electrochemical polishing, again employing HF to achieve smooth surfaces of the initially technically rough starting materials [4]. In order to remove residues from the polishing agents, high-pressure water rinsing [3, 4] and dry ice cleaning [5] are applied. In addition, different heat treatments at up to 800 °C under vacuum [6] or at lower temperatures between 100 °C and 200 °C [1] are needed, and furthermore, heat treatments in N₂ atmospheres have revealed a positive influence on the superconducting RF properties [1, 6-8].

In order to avoid the consumption of hazardous liquids such as HF and to allow a more energy-efficient and environmental friendly preparation of the cavity materials, we have investigated the feasibility of dry laser-polishing treatments of polycrystalline niobium [9]. Furthermore, by conducting the laser-polishing treatments under well-defined N₂ atmospheres, we investigated the feasibility of a successful N-doping simultaneously to the polishing [10], thus adding further synergies to the manufacturing of the cavities, and saving time and energy as well, as the laser only heats the near-surface region of the treated metal, instead of the entire cavity as for conventional treatments in an oven.

Here we report on Nb K-edge (18987 eV) EXAFS-experiments on laser-treated niobium thin foils at DELTA beamline 8 [11]. The samples, 30 mm thick polycrystalline foils, were laser-treated in a setup with a frequency tripled Nd-YAG laser (355 nm), with 9 ns pulse duration and 10 Hz repetition rate [9]. The samples are located in a small ultrahigh vacuum chamber with a base pressure below 10⁻⁷ mbar, and high-purity N₂-gas is introduced via a leak valve to the desired level. More details about the laser-processing are given elsewhere [9]. The X-ray experiments were carried out on laser-treated areas of 4x5 mm², so that the beam from the Si(311) monochromator of beamline 8 with a size of 0.3 mm (v) x 3 mm (h) can be well accommodated on the treated areas. For the transmission mode EXAFS experiments, the incident intensity is measured using an Ar-filled ionization chamber, while the transmitted intensity as well as the intensity behind a Nb reference foil were measured using ionization chambers with a Xe-Ar-mixture. High-quality EXAFS scans covering at least 1500 eV above the edge corresponding to about 20 Å⁻¹ were measured. Data reduction and analysis was performed using the Demeter package [12], and some exemplary X-ray absorption fine structure data $\chi(k)*k^3$ extracted from Nb foils laser polished at three different N₂-pressures are presented in Figure 1(a).

Since EXAFS in general originates from the scattering and the interference of photoelectron waves from neighboring atoms, even small changes of the short range order around the X-ray absorbing atom are sensitively reflected in the fine structure oscillations $\chi(k)*k^3$. As can be seen in Figure 1(a), clear and almost noise-free EXAFS oscillations are visible up to a photoelectron wave vector of 16 Å⁻¹, but no clear differences between the spectra are detectable. However, the structural modifications induced by the laser-processing in N₂-atmospheres are more clearly visible in the Fourier-transformed data in Figure 1(b). With increasing N₂-pressure, the decrease of the peaks at 2.56 Å and 3.02 Å belonging to the first and second Nb-Nb-coordination are clearly detectable. In Figure 1(c), the decrease in the amplitude of the first coordination shell is depicted as a function of the N₂-pressure

for several samples. An abrupt decrease in amplitude is visible for nitrogen pressures above ca. 10^{-3} mbar, and the decrease in amplitude is about 5 % for $p(\text{N}_2)=5 \times 10^{-2}$ mbar.

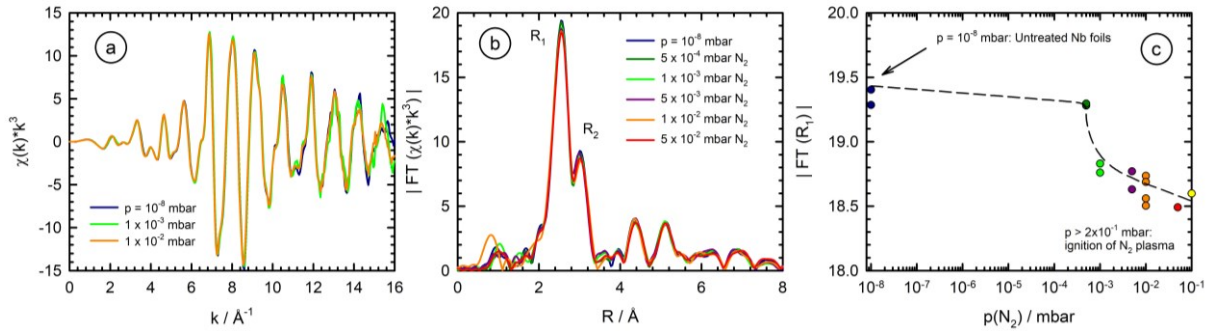


Fig. 1: (a) Comparison of the k^3 -weighted X-ray absorption fine structure data $\chi(k) \cdot k^3$ at the Nb K-edge obtained from Nb foils after a laser polishing at different N_2 pressures during the treatment as indicated. A slight decrease in the amplitude of the oscillations is detectable for larger k -values. (b) Magnitude of the Fourier-transform of the EXAFS oscillations $|\text{FT}(\chi(k) \cdot k^3)|$ for Nb foils after laser polishing at different pressures as indicated (k -range for the FT: $1.3 \text{\AA}^{-1} < k < 15.2 \text{\AA}^{-1}$, data are not corrected for phase-shifts). (c) Magnitude of the FT for the first Nb-Nb coordination R_1 as a function of the N_2 -pressure during the laser treatment. Each data point corresponds to an individual sample. The dashed line is meant to guide the eye.

The detailed analysis of the EXAFS data, i.e., a quantitative fitting of the detected first and second nearest Nb-Nb neighbor coordination shows a slight increase of the Nb-Nb bond distances with nitrogen pressure, and also a slight increase in the disorder parameter [10]. Both observations are well aligned with the incorporation of nitrogen in the bcc lattice of the niobium, see e.g., [13]. Thus, in conclusion, it appears promising to further optimize the laser polishing treatments under nitrogen atmospheres, to further improve the properties of the Nb cavities in a more sustainable way.

Acknowledgements

We gratefully acknowledge the DELTA machine group for providing synchrotron radiation reliably. This project was financially supported by the German Federal Ministry of Education and Research (BMBF, grants No. 05H21PXR1 and 05H24PXA).

References

- [1] D. Bafia, A. Grassellino, Z. Sung, A. Romanenko, O. S. Melnychuk, Gradients of 50 MV/m in TESLA-shaped cavities via modified low temperature bake. Proc. SRF 2019, Dresden. DOI: 10.18429/JACoW-SRF2019-TUP061
- [2] J. Sekutowicz, New Geometries: Elliptical Cavities. In: Proc. Workshop on Pushing the Limits of RF Superconductivity. K.-J. Kim, C. Eyberger (Eds), Argonne, ANL-05/10, p. 3 (2005).
- [3] L. Lilje, C. Antoine, C. Benvenuti, D. Bloess, et al., Nucl. Instrum. Methods Phys. Res A 516, 213 (2004).
- [4] A. Navitski, A. Prudnikava, Y. Tamashevich, R&D on SRF cavities at DESY towards the ILC performance goal. Proc. 5th Int. Particle Acc. Conf. IPAC2014, Dresden WEPRI011 (2014). DOI: 10.18429/JACoW-IPAC2014-WEPRI011
- [5] A. Dangwal, G. Müller, D. Reschke, K. Floettmann, X. Singer. J. Appl. Phys. 102, 044903 (2007).
- [6] A. Grassellino, A. Romanenko, D. Sergatskov, O. Melnychuk, et al., Supercond. Sci. Technol. 26, 102001 (2013).
- [7] A. Grassellino, A. Romanenko, Y. Trenikhina, M. Checchin, et al., Supercond. Sci. Technol. 30, 094004 (2017).
- [8] P. Dhakal, G. Ciovati, G. R. Myneni, K. E. Gray, et al., Phys. Rev. ST Accel. Beams 16, 042001 (2013).
- [9] F. Brockner, D. Lützenkirchen-Hecht, Rev. Sci. Instrum. 95, 043003 (2024).
- [10] F. Brockner, D. Lützenkirchen-Hecht, Appl. Phys. Lett. 125, 201902 (2024).
- [11] D. Lützenkirchen-Hecht, R. Wagner, U. Haake, A. Watenphul, et al., J. Synchrotron Rad. 16, 264 (2009).
- [12] B. Ravel, M. Newville, J. Synchrotron Rad. 12, 537 (2005).
- [13] J. Klaes, P. Rothweiler, B. Bornmann, R. Wagner, et al., J. Synchrotron Rad. 28, 266 (2021).

XAS Investigations of Copper Nanoparticles on Biomass for Biomass Valorization

F. Stallmann,^a L. M. Lindenbeck,^a D. Lützenkirchen-Hecht,^b A. Drichel,^a B. B. Beele,^a
B. V. M. Rodrigues,^a A. Slabon^a

^a Chair of Inorganic Chemistry, Faculty of Mathematics and Natural Sciences, University of Wuppertal, Gaußstraße 20, 42119 Wuppertal, Germany

^b Department of Physics, Faculty of Mathematics and Natural Sciences, University of Wuppertal, Gaußstraße 20, 42119 Wuppertal, Germany

Waste materials should be reconceptualized as underutilized by-products, capable of reintegration into the material cycle through targeted recycling processes.¹ The depolymerization of lignin represents a sustainable pathway for the production of value-added chemicals.²⁻⁵ Copper, used as a bulk catalyst, has demonstrated catalytic activity in facilitating the depolymerization of lignin.² Furthermore, copper nanoparticles have exhibited catalytic efficacy in electrochemical experiments, particularly in promoting the formation of C-C bonds.⁶ In this study we investigated copper nanoparticles (CuNP) on a coffee-biochar matrix, for the lignin depolymerization.

The structural form of the CuNP was observed throughout the entire synthesis process. The synthesis of CuNP, followed by the formation of an electrode with CuNP. The electrode was employed in the process of lignin depolymerization.

Table 1 Intermediate products of the different steps of CuNP

Sample	description
CuNP@C	CuNP on Coffee
CuNP@CB	CuNP on Coffe biochar
CuNP@CB@CP	CuNP on Coffe biochar on Carbonpaper
CuNP@CB@CP 1x	Single use of CuNP@CB@CP

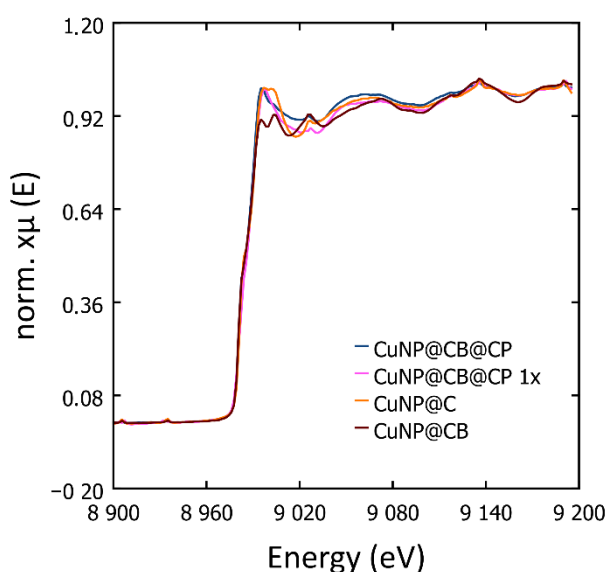


Figure 1. XANES-spectra of the Cu K-edge observing the intermediate products, different oscillations after the edge and a shift of 1 eV of the absorption edge.

In the XAS spectra different oscillations can be observed. This indicates a change in the formation of the nanoparticles during the synthesis. There are also some differences in the oxidation state. The absorption edge has a positive shift of 1 eV which speaks for oxidation of the Cu. The oxidation state changes from Cu(0) after carbonization while preparation for the electrode to Cu(I) and after using the electrode Cu(II) is also existing. This is an indication for oxidation of the CuNP while depolymerization.

Additionally, CuNP was observed *in-operando* in dependence on the potential.

No change in oscillations are observed in XANES, which suggests that the structure of the CuNP remains stable throughout different potentials (see Fig. 2A). A comparison of the Gaussian fit of

the initial normalized derivation reveals no alteration in the absorption edge, indicating that the oxidation state is independent of the potential as can be deduced from Fig. 2(B).

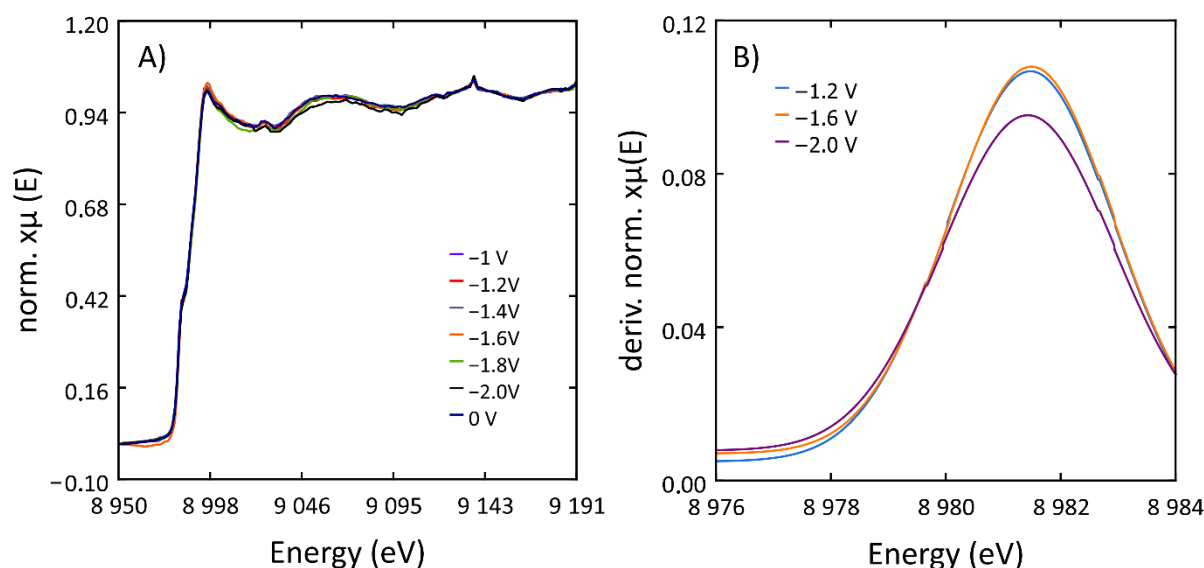


Figure 2. Stability of CuNP. **A** normalized Cu K-edge XANES spectra measured in-operando for different potentials same oscillations **B** Gaussian-fit for the first derivation in the edge region ($8976 \text{ eV} < E < 8984 \text{ eV}$) of the normalized Cu K-edge XANES-spectra. No absorption edge shift observed.

A more detailed analysis of the characterization of the catalyst is currently under way and will be published in a forthcoming publication.

Acknowledgements

We gratefully acknowledge the DELTA machine group for providing synchrotron radiation reliably.

References

- (1) Osman, A. I.; Abdelkader, A.; Farrell, C.; Rooney, D.; Morgan, K. Reusing, Recycling and up-Cycling of Biomass: A Review of Practical and Kinetic Modelling Approaches. *Fuel Process. Technol.* **2019**, *192*, 179–202. <https://doi.org/10.1016/j.fuproc.2019.04.026>.
- (2) Da Cruz, M. G. A.; Gueret, R.; Chen, J.; Piątek, J.; Beele, B.; Sipponen, M. H.; Ferauscher, M.; Budnyk, S.; Rodrigues, B. V. M.; Slabon, A. Electrochemical Depolymerization of Lignin in a Biomass-based Solvent**. *ChemSusChem* **2022**, *15* (15), e202200718. <https://doi.org/10.1002/cssc.202200718>.
- (3) Lindenbeck, L. M.; Barra, V. C.; Dahlhaus, S.; Brand, S.; Wende, L. M.; Beele, B. B.; Schebb, Nils. H.; Rodrigues, B. V. M.; Slabon, A. Organic Chemicals from Wood: Selective Depolymerization and Dearomatization of Lignin via Aqueous Electrocatalysis. *ChemSusChem* **2024**, *17* (9), e202301617. <https://doi.org/10.1002/cssc.202301617>.
- (4) Lindenbeck, L. M.; Dahlhaus, S.; Wende, L. M.; Beele, B. B.; Ferauscher, M.; Schebb, N. H.; Lehmann, C. W.; Bornhorst, J.; Slabon, A.; Rodrigues, B. V. M. Breaking down Lignin in Gamma-Valerolactone: Advances into a Bioelectrorefinery. *Green Chem. Lett. Rev.* **2024**, *17* (1), 2390867. <https://doi.org/10.1080/17518253.2024.2390867>.
- (5) Lindenbeck, L.; Brand, S.; Stallmann, F.; Barra, V.; Ferauscher, M.; Beele, B. B.; Slabon, A.; Rodrigues, B. V. M. Silver-Catalyzed Aqueous Electrochemical Valorization of Soda Lignin into Aliphatics and Phenolics. *Polymers* **2024**, *16* (23), 3325. <https://doi.org/10.3390/polym16233325>.
- (6) Kim, D.; Kley, C. S.; Li, Y.; Yang, P. Copper Nanoparticle Ensembles for Selective Electroreduction of CO_2 to C_2 – C_3 Products. *Proc. Natl. Acad. Sci.* **2017**, *114* (40), 10560–10565. <https://doi.org/10.1073/pnas.1711493114>.

EXAFS investigations of Fe-Co single atoms catalysts on N-doped carbon supports

K. Yuan^a, Y. Pei^a, Y. Wu^a, Y. Chen^a, B. Wu^a, D. Lützenkirchen-Hecht^b

^a College of Chemistry and Chemical Engineering/Institute of Polymers and Energy Chemistry (IPEC), Nanchang University, Nanchang, 330031, China

^b Faculty of Mathematics and Natural Sciences-Physics Department, University of Wuppertal, Gauss-Str. 20, D-42119 Wuppertal, Germany

The transition towards sustainable energy conversion and storage technologies is of utmost global importance, primarily because of a needed reduction of CO₂ emissions and finite availability of fossil fuels. Here, metal-air batteries and fuel cells employing the oxygen reduction reaction (ORR) come into play [1-3]. Accordingly, high-performance electrocatalysts are needed. Although platinum catalysts have outstanding ORR activities in proton exchange membrane fuel cells (PEMFCs) [4, 5], the huge costs of the noble metal hindered their practical application on a large scale. Thus, diverse activities are ongoing worldwide to develop efficient, Pt-free electrocatalysts. In particular, nanostructured M-N-C catalysts employing earth-abundant metals (M=Fe, Co, Ni, Mn, Cu, etc.) have been recognized as a very promising alternative to noble metal based ORR materials, and a structural engineering of these materials is expected to substantially boost their catalytic performance [6-10].

In a continuation of our recent activities on structural investigations of Pt-free electrocatalysts with X-ray absorption spectroscopy at DELTA (see e.g., [11-19]), we investigated a Fe-Co catalysts on a nitrogen-doped carbon host here. Due to their inherent sensitivity towards the atomic short range order around the X-ray absorbing atom, EXAFS and XANES are invaluable techniques for detailed structural investigations of these materials [19]. For the present experiments, the opportunity to investigate Fe and Co separately is of particular importance. The samples were prepared on ZIF-derived N-doped carbon, that was used to adsorb the Fe- and Co-metal ions from solution. The final samples were obtained after annealing under N₂ atmosphere. X-ray absorption experiments at the Fe and Co K-edges (7112 eV and 7709 eV, respectively) were conducted at DELTA beamline 10, employing a Si(111) channel-cut monochromator and gas-filled ionization chambers [20]. Powder samples were filled into PVC sample holders in order to obtain a homogeneous sample with sufficient absorption. In Fig. 1, raw absorption data obtained from a representative sample are presented. With an edge jump of only about 0.1 at the Fe K-edge and even less (0.05) at the Co K-edge, the difficulty of the experiments is obvious, i.e., a data quality sufficient for a detailed analysis needs to be obtained by averaging over several consecutive scans.

In the two insets, the magnitude of the Fourier-transforms of the k²-weighted EXAFS fine structures |FT(k²*χ(k))| are presented. For both metals, a fourfold planar coordination with N was assumed, and the fits are also included in the graphs. As can be seen, the experimental data are well-described by a nearest neighbor environment consisting of 4 nitrogen atoms, and a distance of R₁(Fe-N) = 2.02 ± 0.01 Å and a mean square disorder of σ₁(Fe-N)² = 5.42 × 10⁻³ ± 1.19 × 10⁻³ Å² in the case of Fe, and R₁(Co-N) = 1.88 ± 0.03 Å and σ₁(Co-N)² = 6.76 × 10⁻³ ± 4.27 × 10⁻³ Å² in the case of Co, respectively. The shorter Co-N bond length is well in agreement with previous experiments, as well as the values obtained for the disorder parameters. It is important to note, that no Fe-Co contributions are detectable in the Fourier-transforms of both metals, indicating that isolated single atom catalysts have been prepared.

The catalytic performance of the prepared catalysts is currently under evaluation and will be published elsewhere.

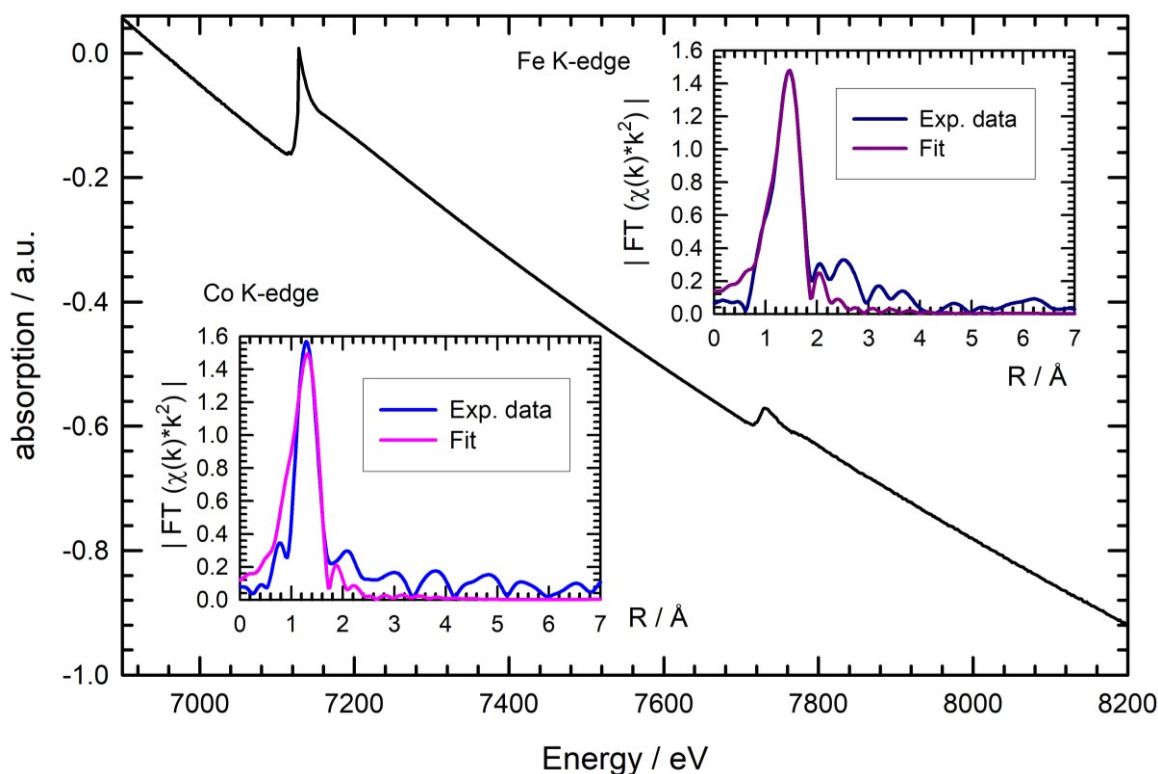


Fig. 1: Raw X-ray absorption data measured for a Fe-Co electrocatalysts on nitrogen-doped carbon. The magnitude of the Fourier-transforms of the k^2 -weighted EXAFS fine structure oscillations $|FT(k^2 \cdot \chi(k))|$ is depicted in the inserts for both Co and Fe. In addition, fits assuming a fourfold coordination of the respective metal with nitrogen have been performed and are included in the graphs as well.

Acknowledgements

We gratefully acknowledge the DELTA machine group for providing synchrotron radiation reliably.

References

- [1] J. Li, M. Chen, D.A. Cullen, S. Hwang, M. Wang, et al., *Nature Catal.* 1 (2018) 935.
- [2] A.A. Gewirth, J.A. Varnell, A.M. DiAscro, *Chem. Rev.* 118 (2018) 2313.
- [3] L. Liu, G. Zeng, J. Chen, L. Bi, L. Dai, Z. Wen, *Nano Energy* 49 (2018) 393.
- [4] B. Wong, *J. Power Sources* 152 (2005) 1.
- [5] J. Wu, H. Yang. *Acc. Chem. Res.* 46 (2013) 1848.
- [6] C. Zhu, H. Li, S. Fu, D. Du, Y. Lin, *Chem. Soc. Rev.* 45 (2016) 517.
- [7] Y. He, Q. Tan, L. Lu, J. Sokolowski, G. Wu. *Electrochem. Energy Rev.* 2 (2019) 231.
- [8] Z. Shi, W. Yang, Y. Gu, T. Liao, Z. Sun, *Adv. Sci.* 7 (2020) 2001069.
- [9] J.S. Bates, M.R. Johnson, F. Khamespanah, T.W. Root, S.S. Stahl, *Chem. Rev.* 123 (2023) 6233.
- [10] X. Li, D. Wang, S. Zha, Y. Chu, L. Pan, M. Wu, C. Liu, W. Wang, N. Mitsuzaki, Z. Chen. *Int. J. Hydrogen Ener.* 51 (2024) 51
- [11] K. Yuan, S. Sfaelou, M. Qiu, D. Lützenkirchen-Hecht, et al., *ACS Energy Lett.* 3 (2018) 252.
- [12] K. Yuan, M. Qiu, D. Lützenkirchen-Hecht, X. Zhuang, Y. Chen, X. Feng, U. Scherf, *J. Amer. Chem. Soc.* 142 (2020) 2404.
- [13] Y. Wu, X. Tang, F. Zhang, L. Li, W. Zhai, B. Huang, et al., *Mater. Chem. Frontiers* 6 (2022) 1209.
- [14] B. Huang, S. Huang, C. Lu, L. Li, J. Chen, T. Hu, et al., *CCS Chem.* 5 (2023) 1876.
- [15] L. Li, X. Tang, S. Huang, C. Lu, D. Lützenkirchen-Hecht, K. Yuan, et al., *Angew. Chemie Int. Ed.* 62 (2023) 202301642.
- [16] B. Wu, J. Xiao, L. Li, T. Hu, M. Qiu, D. Lützenkirchen-Hecht, K. Yuan, Y. Chen, *CCS Chem.* 5 (2023) 2545.
- [17] B. Huang, Q. Gu, X. Tang, D. Lützenkirchen-Hecht, K. Yuan, Y. Chen, *Nature Commun.* 15 (2024) 6077.
- [18] X. Tang, Y. Zhang, S. Tang, D. Lützenkirchen-Hecht, K. Yuan, Y. Chen, *ACS Catal.* 14 (2024) 13065 - 13080
- [19] D. Lützenkirchen-Hecht, K. Yuan, F. Eckelt, F. Braun, et al., *Phys. Stat. Sol. A* (2024), 2400606.
- [20] D. Lützenkirchen-Hecht, R. Wagner, S. Szillat, A.K. Hüsecken, et al., *J. Synchrotron Rad.* 21 (2014) 819.

Feasibility study for in-situ investigations of Vanadium in battery materials by XANES

M. Spiewak,^a A. Drichel,^a V. Barra,^a N. Petersen,^a A. Slabon,^a D. Lützenkirchen-Hecht,^b

^a Chair of Inorganic Chemistry, Faculty of Mathematics and Natural Sciences, University of Wuppertal, Gaußstraße 20, 42119 Wuppertal, Germany

^b Department of Physics, Faculty of Mathematics and Natural Sciences, University of Wuppertal, Gaußstraße 20, 42119 Wuppertal, Germany

X-ray absorption near edge spectroscopy (XANES) is a valuable tool for the investigation of battery materials, due to its inherent sensitivity to the local atomic structure around the X-ray absorbing atom. This is of particular interest for multi-elemental samples such as batteries, as each of the constituting elements can be separately selected by using photon energies in the vicinity of the respective absorption edge [1]. Furthermore, similar to photoelectron spectroscopy, the exact energy of the absorption edge in the XANES spectrum is a sensitive function of the chemical valence of the excited atom. Accordingly, a shift of the absorption edge toward higher photon energies is observed as the chemical valency of the absorber atom is increased, i.e., with increasing oxidation state. Thus, the charge and discharge of batteries can be followed by inspecting the position of the absorption edge in-situ and ex-situ (see, e.g., [2-4]). Furthermore, there are also features in the XANES below the edge. These so-called pre-edge peaks can be attributed to transitions from the excited photoelectron into unoccupied electronic levels of the sample, that is, an X-ray absorption spectrum probes the density of unoccupied states of the absorbing element [1]. Each compound is thus characterized by a characteristic shape in the edge region, i.e., from ca. 20 eV below the edge to ca. 50 eV above the edge, that is characteristic not only for the oxidation state, but also for the coordination geometry of the investigated compound [1, 5]. As a consequence, XANES spectra can be sensitively used for a qualitative and quantitative analysis of mixtures, where the X-ray absorbing element is present in more than one chemical state, for example by linear combination fitting with spectra of model compounds [6].

Here we want to investigate the feasibility of in-situ Vanadium K-edge XANES for battery materials. For this purpose, a coin cell was equipped with two conductive Kapton windows (5 mm in diameter), a carbon cathode, and a nanoscale V₂O₅-containing anode electrode, both coated on Al foil (see Fig. 1). Cellulose was used as a separator and Potassium acetate was used as the electrolyte. Typically, a thickness of about 1 µm was used. The XANES experiments were conducted at DELTA beamline 10 [7], employing a Si(111) monochromator, N₂-filled ionization chambers for the incident and the transmitted beam, and a large-area photodiode for the detection of the emitted fluorescence radiation.



Figure 1. Photo of the un-assembled coin cell with front and back windows, spacer membrane, and the V-loading used for the XANES experiments at DELTA beamline 10.

In general, the transmitted signals are very weak, due to the strong parasitic absorption of the windows, the counter electrode and the electrolyte, so that no meaningful XANES data could be detected in transmission. However, employing the fluorescence signals, we were able to measure XANES spectra of the Vanadium in the battery, as shown in Fig. 2. There we compare the V K-edge XANES of a V₂O₅

reference sample measured in fluorescence to that of the battery. As can be seen, the amplitude and the edge jump of the XANES of the battery are smaller by a factor of about 1000, which reflects the strong parasitic absorption by the electrolyte and the windows of the electrochemical cell. However, the pre-peak at about 5470 eV typical for tetrahedrally coordinated V_2O_5 [8, 9] is clearly visible also in the spectrum of the battery, suggesting that V^{5+} in a tetrahedral environment is dominating this material. In order to obtain more quantitative information from the data and for systematic in-situ / operando studies, further improvements (e.g. the use of an energy-dispersive X-ray detector for the fluorescence) have to be considered.

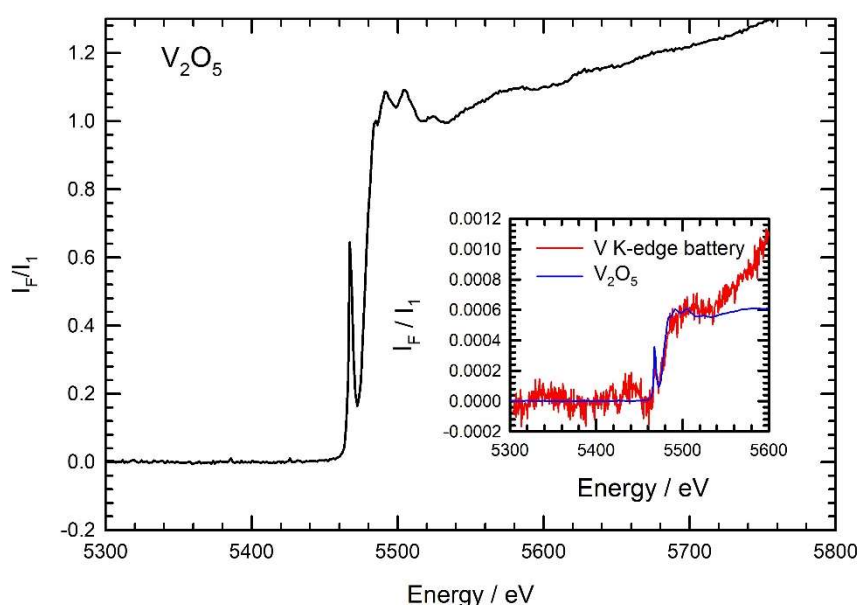


Figure 2. V K-edge XANES spectrum from a V_2O_5 reference sample measured in fluorescence mode. The pre-peak characteristic for tetrahedral V^{5+} is clearly resolved. In the insert, the spectrum of the battery material is compared to the reference spectrum, that is scaled in amplitude to match the battery spectrum. Pre- and post-edge features of the battery spectrum fit qualitatively well to that of the V_2O_5 reference.

A more detailed analysis of the characterization of the catalyst is currently under way and will be published in a forthcoming publication.

Acknowledgements

We gratefully acknowledge the DELTA machine group for providing synchrotron radiation reliably.

References

- (1) Koningsberger, D.; Prins, R. X-ray Absorption: Principles, Applications, Techniques of EXAFS, SEXAFS and XANES; Wiley: New York, 1988
- (2) Cheng, W.; Zhao, M.; Lai, Y.; Wang, X.; Liu, H.; Xiao, P.; Mo, G.; Liu, B.; Liu, Y. Exploration 4 (2024) 20230056. DOI: 10.1002/EXP.20230056 (3)
- (3) Ghigna, P.; Quartarone, E. J. Phys. Energy 3 (2021) 032006. DOI: 10.1088/2515-7655/abf2db
- (4) Wang, ; Chen-Wiegart, Y.-C. K.; Wang, J. Nature Commun. 5 (2014) 4570. DOI: 10.1038/ncomms5570
- (5) Pantelouris, A.; Modrow, H.; Pantelouris, M.; Hormes, J.; Reinen, D. Chem. Phys. 300 (2004) 13. DOI: 10.1016/j.chemphys.2003.12.017.
- (6) Wasserman, S. J. Phys. IV 7 (1997) C2 203. DOI: 10.1051/jp4/1997163
- (7) Lützenkirchen-Hecht, D.; Wagner, R.; Szillat, S.; Hüsecken, A. K.; Istomin, K.; Pietsch, U.; Frahm, R. J. Synchrotron Rad. 21 (2014) 819. DOI: 10.1107/S1600577514006705.
- (8) Palanisamy, K.; Um, J.H.; Jeong, M.; Yoon, W.-S. Sci. Rep. 6 (2016) 31275. DOI: 10.1038/srep31275.
- (9) Horrocks, G.A.; Braham, E.J.; Liang, Y.; De Jesus, L.R.; Jude, J.; Velázquez, J.; Prendergast, D.; Banerjee, S. J. Phys. Chem. C 120 (2016) 23922. DOI: 10.1021/acs.jpcc.6b06499

Notes

Notes